Multi-Redox Active Polyanionic Cathodes for Alkali-ion Batteries

by

Ian Lawrence Matts

Submitted to the Department of Materials Science and Engineering
in partial fulfillment of the requirements for the degree of

Doctor of Philosophy in Materials Science and Engineering

at the

MASSACHUSETTS INSTITUTE OF TECHNOLOGY

June 2016

Author .....
Department of Materials Science and Engineering
May 9, 2016

Certified by .....
Gerbrand Ceder
Professor
Thesis Supervisor

Accepted by .....
Donald Sadoway
Chairman, Department Committee on Graduate Theses

Multi-Redox Active Polyanionic Cathodes for Alkali-ion Batteries

by

Ian Lawrence Matts

Submitted to the Department of Materials Science and Engineering
on May 9, 2016, in partial fulfillment of the
requirements for the degree of
Doctor of Philosophy in Materials Science and Engineering

Abstract

In order for alkali-ion batteries to gain widespread adoption as the energy storage technology of choice for transportation and grid applications, their energy must be improved. One key step towards this necessary improvement is the development of new battery cathode materials. In this thesis, two classes of polyanionic materials are examined as candidate cathodes for alkali-ion batteries: Li-containing carbonophosphates for Li-ion batteries and Na-containing fluorophosphates for Na-ion batteries.

High-throughput ab initio calculations have previously identified carbonophosphates as a new class of polyanionic cathode materials. $Li_3MnCO_3PO_4$ is the most promising candidate due to its high theoretical capacity, predicted multi-redox activity, and ideal voltage range. However, a major limitation of this material is its poor cyclability and experimental capacity. In this work $Li_3Fe_{0.2}Mn_{0.8}CO_3PO_4$ is synthesized to combine the high theoretical capacity of $Li_3MnCO_3PO_4$ with the high cyclability of $Li_3FeCO_3PO_4$. $Li_3Fe_{0.2}Mn_{0.8}CO_3PO_4$ outperforms both $Li_3MnCO_3PO_4$ and $Li_3FeCO_3PO_4$, showing a reversible capacity of 105 mAh/g with little capacity fade over 25 cycles. However, poor thermodynamic stability of these compounds, particularly at partially delithiated compositions, prevents carbonophosphates from being seriously considered as a viable Li-ion cathode.

Fluorophosphate cathodes are currently one of the most promising polyanionic sodium-ion battery cathodes due to their high energy density and cyclability. To further improve fluorophosphate cathodes, their capacity must be increased by using Na sites that had not been accessed prior to this work. In this thesis, reversible electrochemical Na^+ insertion into $Na_3V_2(PO_4)_2F_3$ is demonstrated. To further im-

prove fluorophosphate cathodes by using its newly discovered insertion capacity, novel $Na_3[M]_2(PO_4)_2F_3$ cathodes, with {M = Fe, Ti, V}, are synthesized and evaluated. Seeing no improvement, the question of what specific mechanism limits fluorophosphate cathode capacity is addressed. For this, the synthesis, electrochemical characterization, and computational examination of a specifically designed test system, $Na_3GaV(PO_4)_2F_3$, is reported. This leads to the conclusion that large diffusion barriers at high sodiations impose a kinetic limit on Na^+ insertion in fluorophosphate cathodes, as opposed to limits in transition metal redox activity.

Thesis Supervisor: Gerbrand Ceder
Title: Professor

Acknowledgments

I would like to thank my advisor, Professor Gerbrand Ceder, for his guidance over the course of my graduate studies. I am grateful that he challenged me to meet his high scientific and communication standards, for his flexibility in allowing me to pursue what I found interesting, and for trusting me to solve problems with an independent approach.

I would also like to thank my committee, Professor Yang Shao-Horn and Professor Donald Sadoway, for their fruitful discussion and guidance with my project. Their thoughtful questions helped me contextualize my work and made sure I avoided becoming too narrow-minded.

I am grateful for funding provided by Robert Bosch Company and Umicore for my work on Li-ion batteries and Samsung Advanced Institute of Technology for my work on Na-ion batteries.

I owe much of my success to Professor Hailong Chen of Georgia Tech University, who in 2011 was a postdoc in the Ceder Group. He mentored me in the lab when I entered the group and taught me a great deal about batteries, how to make them, and the value of an alternative approach.

I feel privileged to have spent these years with my colleagues in the Ceder Group. Specifically I would like to thank Nancy for her constant willingness to help with presentations, experiments, and the general maintenance of my sanity, Steve for accompanying me down the fluorophosphate rabbit-hole, Rahul for always providing a laugh and being my "Soup of the Day" co-host on WMBR, Jinhyuk for always making sure I'm "working hard," and Kathy for always being helpful and supportive. Everyone in the group taught me something, and I am glad to have shared offices, meetings, and labs with all of them.

Friends made my time in graduate school enjoyable as well as productive, and I wouldn't have wanted to be at MIT without them. Thanks to my friends in the department, out of the department, and out of the Institute including, but certainly not limited to, Dina, Michelle, Alex, Heather, Sara, Abdulla, Marlena, Phil, Ryan, Andrew, Jen, John, Jenn, Sarah, Brian, and my girlfriend Ibby. I would like to thank Ibby, Sarah, Ryan, and Alex in particular for their support during the past year, which included my relocation to Berkeley.

Finally, I am extremely grateful for the love and support of my mom, dad, and sister, without whom I couldn't have gotten to where I am today.

Contents

List of Figures

List of Tables

Chapter 1

Introduction

1.1 Motivation

Due to widespread concerns about the long-term effects of fossil fuel emissions, renewable energy sources are viewed as a long-term solution for meeting growing world energy demands [8, 9]. However, many renewable energy sources, including wind and solar, offer intermittent power supplies that do not always match demand. Therefore, for the generated energy to be widely utilized in grid and transportation applications, it must be stored in times of excess supply so that it can be distributed later when the supply is deficient. Without sufficient grid storage capabilities, renewable sources of energy will not be able to lessen the energy-grid's reliance on fossil fuels to provide base-load power [10, 11, 12, 13, 14]. In addition to grid-level needs, energy storage demands for portable electronics are ever-increasing as devices gain functionality while decreasing in size [15]. Combined, these facts highlight society's need for better batteries. The current leading battery technology in terms of both gravimetric and volumetric energy density is the lithium-ion (Li-ion) battery, as illustrated in Figure

1-1 [1, 16, 17, 18, 19]. Secondary (or rechargeable) Li-ion batteries were invented over 40 years ago, and their ability to store more energy per mass and volume, retain charge over repeated cycles, and operate effectively at faster rates has improved dramatically over this time [20, 21, 22, 23, 24]. However, with expanding storage needs has come demand for even better secondary energy storage, so research efforts to improve Li-ion batteries are ongoing. In addition, other energy storage technologies are being explored to meet these demands [25, 26, 27, 28, 29, 30]. Sodium-ion (Na-ion) batteries are one such alternative technology and are viewed as a possible energy storage alternative for the near future, particularly for grid-level storage applications. However, they have not yet reached the requisite level of performance to supplant Li-ion batteries [31, 32, 33, 34, 35, 36, 37]. This thesis will focus on the synthesis and characterization of Li- and Na-ion battery cathode materials with novel chemistries that are computationally predicted to be able to cycle multiple alkali ions per electrochemically active transition metal ion, and to investigate and explain any performance limitations observed.

1.2 Alkali-ion rechargeable battery overview

Figure 1-2 depicts a schematic of a Li-ion battery and shows its three main components: the anode, cathode, and electrolyte. As noted above, this thesis focuses on both Li- and Na-ion battery cathodes. In a Na-ion battery, Na ions perform the same function as Li ions in a Li-ion battery, while the overall battery format remains the same. As such, the term "working ion," which refers to the mobile ionic species in the battery, will be used in the continued discussion of alkali-ion batteries when identifying the specific ion is not required. The negative electrode, the anode, and the positive electrode, the cathode, are electronic and ionic conductors while

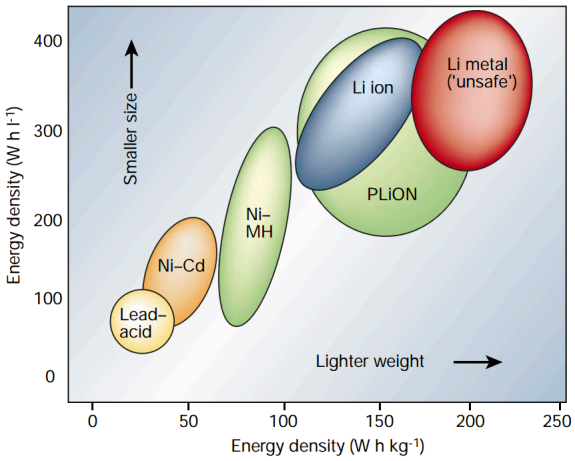

Figure 1-1: A graphical comparison of different battery technologies on a scale of volumetric energy density versus gravimetric energy density. Lead-acid, nickel-cadmium (Ni-Cd), nickel metal-hydride (Ni-MH), lithium-ion (Li-ion), and plastic Li-ion (PLiON) batteries are commercially available, while Li metal batteries are not [1].

the electrolyte is an ionic conductor and an electronic insulator. When the battery is connected to an external circuit, which is an electronic conductor and an ionic insulator, electric energy may be converted to chemical energy, stored as chemical energy, and then converted back to electrical energy in the following manner:

When the battery is charged, a positive voltage is applied between the cathode and anode, driving cathode oxidation, and causing working ions to move across the electrolyte from the cathode to the anode. The free energy of the working ion in the anode is higher than the free energy of the working ion in the cathode, so positive electrical work must be done to complete this process. The different types of functional electrochemical reactions in alkali-ion battery electrodes is discussed in Section 1.4. Overall neutral charge must be conserved, so the positive working ions' arrival at the anode must be compensated by the arrival of electrons with equiv-

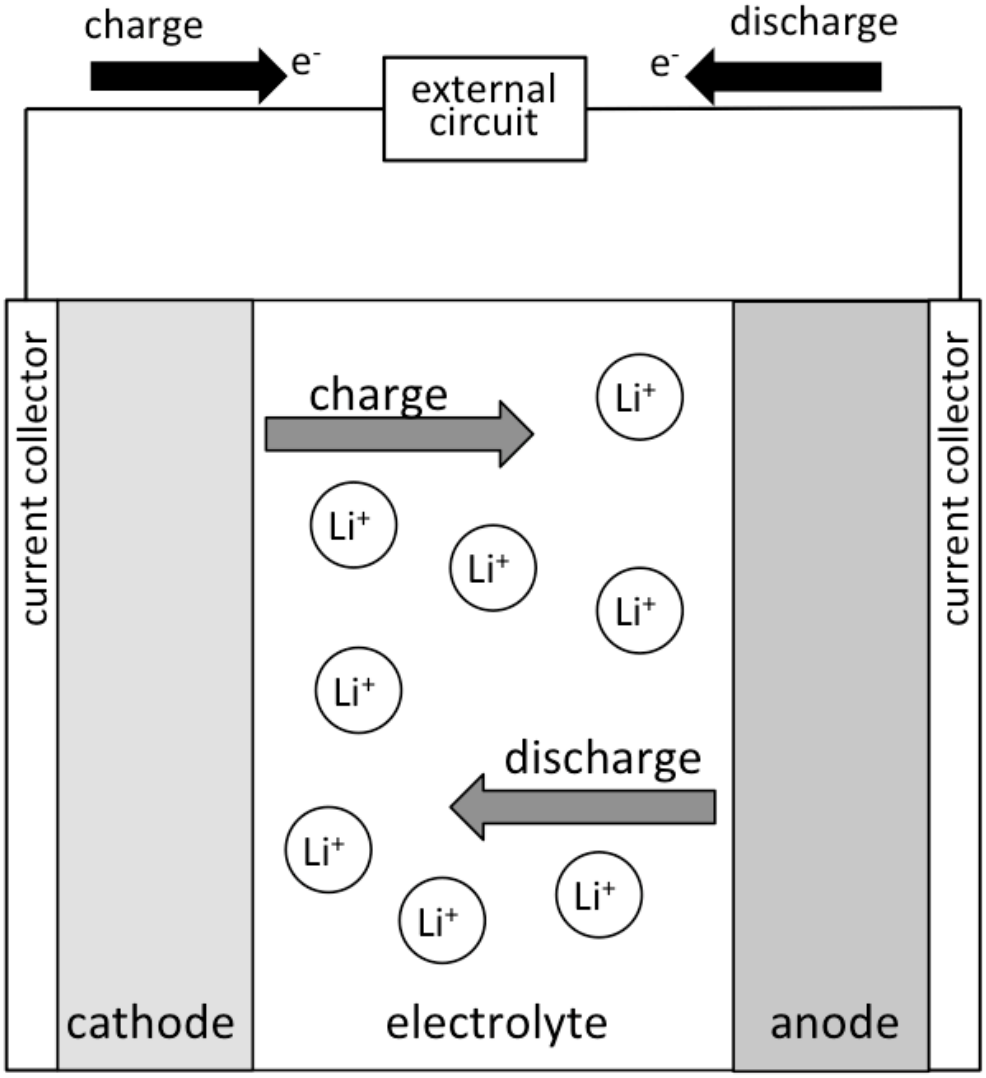

Figure 1-2: Schematic representation of a Li-ion battery, with the major components labelled. When the battery is charged, a voltage is applied across the external circuit, causing Li ions and electrons to move from the cathode to the anode via the electrolyte and external circuit, respectively. The process proceeds in the reverse when the battery is discharged. In the case of a Na-ion battery, Li ions would be replaced with Na ions, while the other components in the schematic remain unchanged.

alent total charge, resulting in the electrochemical reduction of the anode. When the circuit is broken, the working ions will remain in the anode, which is a higher energy state than working ions in the cathode. The working ions are prevented from spontaneously moving to the lower-energy state (in the cathode) because the battery electrolyte is an electronic insulator so the charge of mobile working ions can not be compensated, meaning the working ions must remain in the anode, storing chemical energy. When the circuit is completed with no applied voltage, the working ions will spontaneously move from the anode back to the cathode. Electrons must also move to compensate the mobile ionic charges. The only electronically conducting pathway for such movement is through the external circuit, resulting in the electrons returning electric work. The separation of moving charges between ions in the electrolyte and electrons in the external circuit is the principle by which electrical energy can be stored as chemical energy.

All cathodes in alkali-ion batteries do not contain only active material, but also include high-surface area carbon to increase electrode conductivity and a polymer binder such as polyvinylidene fluoride (PVDF) or polytetrafluoroethylene (PTFE) to hold the electrode component powders together. The most common electrochemically active cathode materials for both Li- and Na-ion batteries are layered oxide cathodes of the type AMO_2, where A = {Li, Na} and M is a transition metal in the third row of the periodic table. The layered structure has a hexagonal unit cell with the $R\bar{3}m$ space group, and is defined by a close-packed oxygen sublattice in which layers of alkali ions and layers of transition metal ions alternate in stacking between oxygen layers.

For Li-ion batteries, $LiCoO_2$ is the most prevalent cathode material [21]. While exhibiting high performance, $LiCoO_2$ is hindered by both the cost of cobalt and the ability to reversibly cycle only half of the lithium ions in the material [38]. To bypass

these issues a number of other layered oxide cathode chemistries that substitute out some or all of the cobalt in favor of other transition metals, such as nickel, manganese, and/or aluminum have been explored and subsequently commercialized [39, 40, 41]. Such substitutions can decrease cost and increase structural stability, allowing more Li to cycle reversibly in these compounds. Spinel and olivine crystal structures such as those in $LiMn_2O_4$ and $LiFePO_4$, respectively, have also been commercialized [16, 42]. These cathodes excel in high-rate applications and are more environmentally friendly than $LiCoO_2$, but ultimately they cannot match the energy density of layered oxide Li-ion cathodes.

For Na-ion layered oxide cathodes, no specific transition metal chemistry has established itself above a wide variety of variations, though Fe-, Ni-, and Mn-containing cathodes are viewed as the most promising due to their low cost and environmental-friendliness [43, 44, 45, 46]. NASICON-type polyanionic cathodes are also of interest, both in fluorinated ($Na_3V_2(PO_4)_2F_3$) and unfluorinated ($Na_3V_2(PO_4)_3$) structures [47, 48, 49, 50, 51]. These cathodes show high energy densities, particularly among non-oxide chemistries, high stability, and improved safety.

Lithium-ion battery anodes are most commonly composed of graphite, into which lithium readily intercalates to form LiC_6 [52]. Silicon-containing anodes for Li-ion batteries have also become prominent. Lithium reacts with silicon via an alloying reaction yielding high energy densities, but also causing large volume changes that have made these cathodes difficult to commercialize until recently [53, 54, 55].

In contrast, sodium cannot intercalate into graphite. Instead, hard carbon is most commonly used [56, 57]. Hard carbon is not as gravimetrically or volumetrically energy dense as graphite, so both intercalating and alloying alternatives, such as $Na_2Ti_3O_7$ and tin-based composites, are actively being sought [58, 59].

The difference in energy between the working ion in the cathode versus the work-

ing ion in the anode is the source of battery voltage. The difference in chemical potentials of the working ion in each electrode is related to the open circuit voltage of the battery by the Nernst equation, which is

$$Voltage = \frac{-(\mu^c - \mu^a)}{zF} \tag{1.1}$$

. μ^c is the chemical potential of the working ion in the cathode, μ^a is the chemical potential of the working ion in the anode, both in joules per mole, z is the working ion valence, and F is the Faraday constant (98,485 Coulombs per mole). The cell voltage is the energy that is stored or returned by one working ion moving across the electrolyte. Complimentary to this, capacity is the amount of working ions that are transported between electrodes across the electrolyte. The specific capacity of an electrode active material, in units of mAh/g, is

$$capacity = \frac{z \cdot N}{3600 \cdot M} \tag{1.2}$$

. z is the valence of the working ion moved from one electrode to the other, N is the number of working ions moved between electrodes, M is the molecular weight of the electrode material in grams per mole, and 3600 is a unit conversion factor. Gravimetric energy density is the product of the average cell voltage and specific capacity. Gravimetric energy density is related to volumetric energy density by the active material's density.

While energy density is maximized when voltage is large, the operating voltage of a battery is functionally limited by electrolyte stability, and the so-called "voltage window" of the electrolyte. The electrolyte window is determined by the difference between the electron energies of the electrolyte's highest occupied molecular orbital (HOMO) and lowest unoccupied molecular orbital (LUMO). For an electrolyte to

be stable, the electron energy of the cathode and anode, or, stated differently, the chemical potential of electrons in each electrode must also fall in between the HOMO and LUMO of the electrolyte solution during the entire charge/discharge cycle. A diagram of of the electron energies in a stable battery system are shown in Figure 1-3. If the electron energy of an electrode falls outside of the window the electrolyte will decompose either via oxidation or reduction reactions at the electrode/electrolyte interface to lower the interface energy [19].

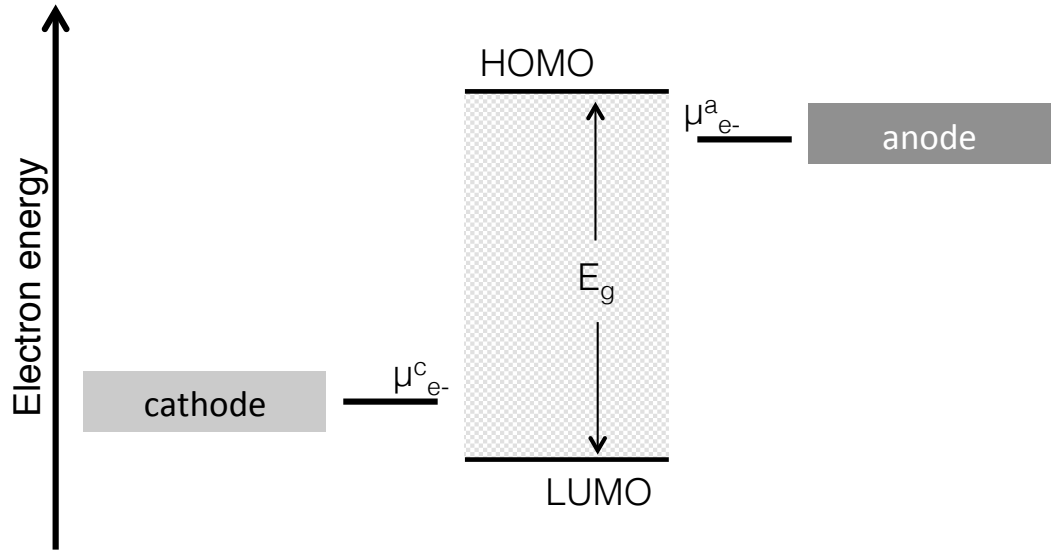

Figure 1-3: Schematic energy band diagram for a thermodynamically stable battery system in an open circuit configuration. The voltage window of the electrolyte is represented as E_g.

In addition to having a large voltage window suited to the electrodes used, alkali-ion battery electrolytes must also have high ionic conductivity, low electronic conductivity, high chemical stability with the electrodes and cell components, low melting

point, and high boiling point. These features are manifested as low viscosity, high polarity, and high relative permittivity [52]. They must also have acceptable costs and toxicity [60]. Based on these constraints, the most successful electrolytes widely-used today in alkali-ion batteries are solutions of Li- or Na-containing salts in organic solvents. Specifically, the most common salts used are $LiPF_6$, $LiBF_4$, and $LiClO_4$ for Li-ion battery electrolytes and $NaPF_6$ and $NaClO_4$ for Na-ion battery electrolytes [61, 62]. These salts benefit from good solubility and separation of charge in solution due to their bulky anion groups [63]. Alkyl carbonates, mostly ethylene carbonate (EC), dimethyl carbonate (DMC), ethyl methyl carbonate (EMC), and diethyl carbonate (DEC), have been adopted as the most common electrolyte solvents for both Li- and Na-ion batteries [64]. Electrolytes are frequently optimized by making binary combinations of these solvents. When using liquid electrolytes, the anode and cathode must also be physically separated in order to prevent a short-circuit while still maintaining an ionic conductive pathway. Commercially, this is achieved by using a microporous PTFE membrane. Glass fiber separator films are frequently used in research electrochemical testing applications as well. Alternatives to alkyl carbonate solutions are actively being sought, with significant research efforts being put toward the pursuit of high-performing solid-state or ionic liquid electrolytes, but as of this time none have supplanted alkali-salt in alkyl carbonate solutions as the preeminent electrolyte technology [65, 66, 67, 68].

1.2.1 Other important battery properties

While voltage and capacity are often the driving force behind materials discovery for alkali-ion battery electrode materials, they are not the only properties considered. In addition to energy density, the main properties considered when developing a new

battery material are cycle life, rate capability, safety, and cost.

Cycle life is the ability of a battery to retain its energy storage capability after repeated cycles. All batteries degrade over time, but it is important for commercial batteries to operate at as high of a percentage of their initial performance as possible during their lifetime; batteries in electric vehicles and in stationary grid storage applications that will require a service lifetime of at least ten years will need to retain their capacity for greater than 10,000 cycles [69]. The main mechanisms by which capacity in batteries is degraded are structural degradation, electrolyte decomposition, and parasitic side reactions, including some forms of solid-electrolyte interface (SEI) growth. These capacity-degrading electrochemically-induced reactions are frequently manifested as coulombic inefficiency, which is the percentage of capacity that is irreversible in a single charge-discharge cycle. Therefore, minimizing coulombic inefficiency, and in doing so maximizing cycle life, is essential for commercial batteries.

Rate capability is a measure of how quickly a battery can charge and discharge while still storing a significant amount of energy. This property is of particular importance to batteries used in high power applications such as motors for power tools and electric vehicles. For a battery to exhibit good rate capability, it is necessary for the cathode to exhibit both high electronic and high ionic conductivity. The most common way to improve electronic conductivity is to incorporate conductive carbon into battery electrodes and carbon-coat active materials in order to create a percolating conductive pathway from the active material to the current collector [70, 71]. Cation doping may also be used to improve the intrinsic electronic conductivity of the active material. The use of doping in $LiFePO_4$ is the most prominent example of utilizing the process to improve electronic conductivity. Chung et al. used supervalent doping to induce p-type conductivity, which in part led to the conductivity

in $LiFePO_4$ to be improved by eight orders of magnitude and allowing it to gain commercial success [72].

Ionic conductivity, and thus ion diffusivity, is the most common limit to rate capability. For an electrochemical reaction to occur throughout the bulk of a material, working ions are required to diffuse from the active material particle's interior to its surface and into the electrolyte. To minimize this diffusion distance, and in doing so shortening ion diffusion times, active material particle sizes are frequently minimized to improve battery rate performance [73]. Within the active material itself, diffusion barriers limit the movement of ions in the cathode crystal structure. Such diffusion barriers are generally determined by the geometry of the diffusion pathway and the electrostatic forces the mobile ion experiences from neighboring ions along this path. These diffusion paths have been shown to occur in either one, two, or three dimensions. Examples of crystal structures with one-, two-, and three-dimensional diffusion paths, such as those in olivine $LiFePO_4$, layered α-$LiCoO_2$, and spinel $LiMn_2O_4$, respectively, are shown in Figure 1-4 [2].

As with nearly every other commercial product, cost is also an important factor for batteries. Cost is one reason that Na-ion batteries may be preferred to Li-ion batteries, as Na-containing ores used for cathode material production are more abundant and cheaper than comparable Li-containing ores [74]. However, the alkali-ion cost is less significant than the cost of the transition metal used. Of all transition metals, Fe, Mn, and Ni are the most attractive due to their low cost, high abundance, and low toxicity. This is one reason why $LiMn_{1/2}Ni_{1/2}O_2$ has begun replacing $LiCoO_2$ in some commercial Li-ion battery cells [39].

Batteries must be adequately safe, even at the cost of performance. As an example, safety concerns prevent the use of metal as an anode despite the possibility of higher energy densities. Dendritic growth on alkali-metal anode surfaces during

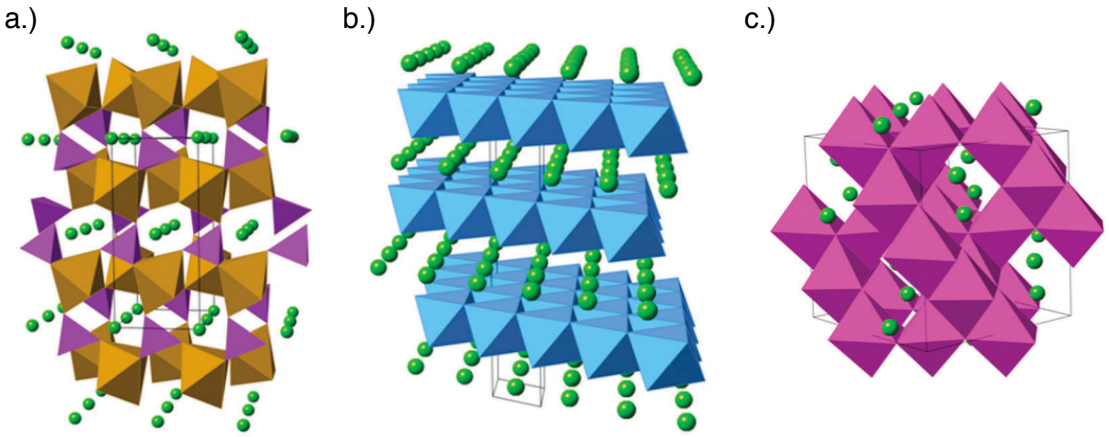

Figure 1-4: Representative crystal structures of cathode materials for alkali-ion batteries with ion diffusion pathways of increasing dimensionality: (a) 1D: Olivine $LiFePO_4$; (b) 2D: layered α-$LiCoO_2$; (c) 3D: spinel $LiMn_2O_4$ [2].

battery cycling can lead to a short-circuit, causing high temperatures and a risk of fire. To diminish these risks and make alkali metal anodes safer, protective thin films preventing dendrite growth are being explored [75, 76]. Until such research is able to be commercialized, carbon anodes are generally used in alkali ion batteries, leading to safer, but less energy dense cells. Cathode safety most commonly refers to a material's propensity to decompose at high voltages via reaction pathways including oxygen gas evolution. The alkyl carbonates commonly used as battery electrolytes react exothermically with oxygen gas, so cathode decomposition can cause thermal runaway and pose a fire hazard [77, 78, 79].

1.3 Categories of reversible electrochemical reactions for alkali-ion battery electrodes

1.3.1 Intercalation

This work focuses exclusively on the discovery of novel intercalation cathodes. Intercalation reactions are topotactic electrochemical reactions in which an ion is removed while leaving the underlying structure unchanged [20, 21]. The most well-characterized intercalation reaction, that in $LiCoO_2$, is shown in the following formula for charge and discharge half cycles:

$$LiCoO_2 \rightarrow xLi + xe^- + Li_{1-x}CoO_2 \textit{ (charge)}$$

$$xLi + xe^- + Li_{1-x}CoO_2 \rightarrow LiCoO_2 \textit{ (discharge)}$$

Most simply, the working ion is removed from the cathode, leaving behind a vacancy during charge that can then be filled on discharge. Intercalation reactions tend to be highly reversible as the underlying crystal structure framework does not change on cycling. During such reactions, the cathode volume change is relatively small and the structure is mostly undamaged by fracture, stacking faults, or phase changes. Combined, this leads to high capacity retention over repeated cycling and good rate capability in intercalation cathodes. However, with the exception of tavorite and NASICON cathodes in Li- and Na-ion batteries, respectively, only one electron per transition metal can be moved through the external circuit, yielding limited capacity [80, 81, 82]. As such, this work hopes to expand the capacity of intercalation cathodes while maintaining the benefits of cycling stability.

1.3.2 Conversion and alloying

The other main categories of active material reactions in battery electrodes are conversion and alloying reactions, which have similar benefits and limitations. In conversion reactions, lithium reacts with the electrode material, and the materials undergo an exchange reaction, as shown in the following formula for Li and FeF_3 [83, 84, 85, 86].

$$FeF_3 + 3Li^+ + 3e^- \rightarrow 3LiF + Fe_{(s)} \textit{ (charge)}$$

$$3LiF + Fe_{(s)} \rightarrow FeF_3 + 3Li^+ + 3e^- \textit{ (discharge)}$$

In alloying reactions, lithium reacts with the electrode to form an alloy on discharge, which is decomposed on charge.[87, 88, 89] The alloying reaction for lithium and silicon proceeds as follows [53, 89]:

$$xLi^+ + Si_{(s)} + xe^- \rightarrow Li_xSi \textit{ (discharge)}$$

$$Li_xSi \rightarrow xLi^+ + Si_{(s)}\ xe^- \textit{ (charge)}$$

In both conversion and alloying reactions, each redox active species, Fe or Si in the given examples, can access all available redox states, resulting in higher capacities than in intercalation reactions [84, 85, 86, 90, 53, 89]. However, unlike intercalation reactions, in which the overall crystal structure of the active material remains unchanged during cycling, materials undergoing conversion or alloying reactions undergo significant structural transformations, often manifested as phase

transformations with large volume changes [83, 73, 86, 90, 87, 88, 53, 89]. For example, as silicon is alloyed with lithium its volume can expand by approximately 400%. With such large changes in volume and structure, these types of reactions exhibit slower kinetics and suffer from poorer reversibility than intercalation reactions [83, 84, 85, 86, 90, 87, 53, 89]. As a consequence of these issues, cathodes of these types are difficult to implement in commercial batteries.

1.4 Na- versus Li-ion rechargeable batteries

As described in Section 1.2, Li- and Na-ion batteries function in fundamentally the same way. Thus, it is not surprising that both of these technologies were invented around same time [91, 92, 93, 94]. However, Li-ion batteries soon surpassed Na-ion batteries and became the more-widespread energy storage technology. One clear advantage that Li-ion batteries has over Na-ion batteries is the molecular weight of Li, which is 6.94 g/mol compared to Na's molecular weight of 22.99 g/mol. Thus, analogous chemistries with similar performance in terms of moles of alkali-ion cycled will always favor lithium-containing compounds on the basis of specific capacity, which is inversely proportional to active material molecular weight. Lithium is also a smaller ion than sodium, which have effective ionic radii of 76 and 102pm, respectively. Therefore, lithium frequently has a higher mobility than sodium in similar crystal structures. Further, Na-vacancy ordering is stronger than Li-vacancy ordering in alkali ion cathodes, meaning that Li-cathodes often have smoother voltage curves, making them more easily used in devices [95, 96, 42, 64, 21]. This difference is most evident in $LiCoO_2$ and $NaCoO_2$, which show qualitatively different voltage curves despite sharing a layered crystal structure, are shown in Figure 1-5 [3].

As a result of these, and other, factors, Li-ion batteries developed quickly while

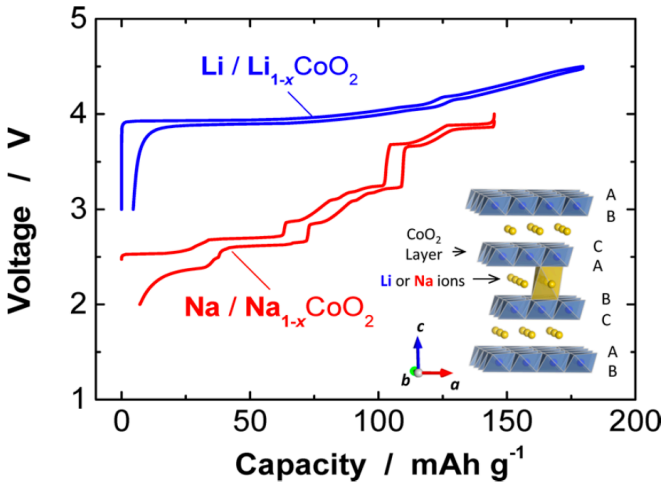

Figure 1-5: A comparison of charge and discharge curves of $Li/LiCoO_2$ and $Na/NaCoO_2$ cells of the same crystal structure. A schematic illustration of the Li(Na)CoO2 crystal structure is also shown. This figure was originally published by Yabuuchi et al.[3].

Na-ion battery research slowed. However, as energy storage needs continue to increase and Li-ion battery technology nears its ultimate maturity, Na-ion batteries are being revisited as a possible alternative. Lithium is relatively scarce, so the high abundance and low-cost of sodium is often given as a driving force in the recent development of Na-ion technologies [74]. However, work to discover new Na-ion battery materials in the Ceder Group, and in Chapter 3 of this thesis in particular, stems from the belief that such technologies with novel structures and chemistries may supplant Li-ion batteries on the basis of performance. As such, efforts to discover new Na-ion battery materials are ongoing.

Much of the current research on materials discovery for Na-ion batteries focuses on finding cathodes whose structures are analogous to known Li-ion battery cathodes. To date, the main focus has been on layered oxide structures. A greater

number of AMO_2 systems, where A is an alkali ion and M is a transition metal ion, have been shown to be electrochemically active for sodium systems than for lithium systems. For example $NaMO_2$ with M = {Ti, V, Cr, Mn, Fe, Co, Ni} have all been shown to be electrochemically active whereas only Co and Ni are electrochemically active in layered $LiMO_2$ cathodes [97, 98, 99, 100, 101, 95, 102]. However, layered Na-ion cathodes exhibit strong Na-vacancy ordering [103] and phase transitions during electrochemical cycling, which inhibit performance. To improve these cathodes, chemistries with combinations of transition metals have been examined as well [104, 33, 79, 96, 105]. Some of these systems have capacities comparable to that of commercial Li-ion cathodes, including $NaNi_{0.5}Mn_{0.5}O_2$ [99] and $NaMnO_2$ [100], both of which have shown reversible capacities around 185 mAh/g.

While capacities in Na-ion cathodes are similar to those found in analogous Li-ion cathodes, Na-ion reaction voltages are lower in all cases due to weaker alkali-anion bonding in Na-ion cathode ceramics [4]. For oxides, Na-ion systems exhibit redox voltages >0.5 V less, on average, than their Li-ion counterparts. A direct comparison of these calculated voltages in a variety of structures is shown in Figure 1-6, originally shown by Ong et al. [4]. A graph plotting the observed average redox voltage and compound volumetric capacity is presented in Figure 1-6 and confirms this trend experimentally; despite comparable capacities, Na-ion battery cathodes are in general less energy dense than their Li-ion counterparts [5]. In order to achieve energy densities comparable to or exceeding Li-ion cathodes, higher voltage Na-ion cathodes must be explored. Recently, Na-ion battery-oriented chemistries with average voltages of approximately 4 V, including fluorophosphates and different sulfate-based structures, have received an increased amount of attention as Na-ion battery intercalation cathodes [51, 49, 106, 107, 108].

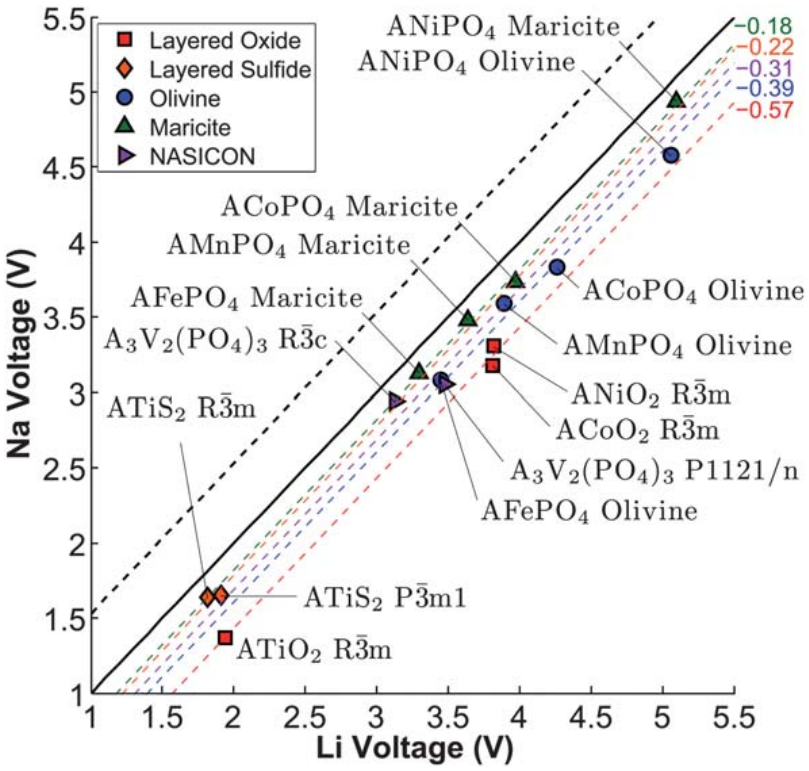

Figure 1-6: Calculated Na voltage vs. calculated Li voltage for different cathode crystal structures. The black dashed line indicates the +0.53 V difference between the cohesive energies of Na and Li, while the other dashed lines indicate the fitted average voltage difference, ΔV_{Na-Li}, for different crystal structures [4].

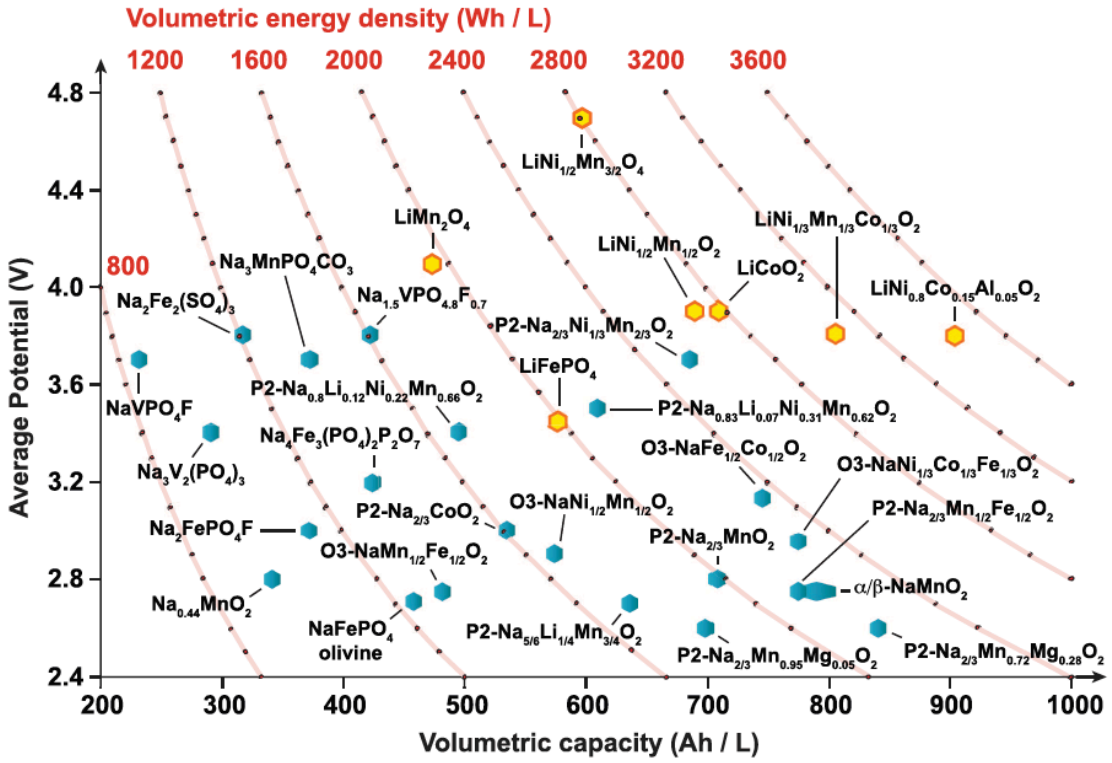

Figure 1-7: Average discharge potential (V vs. Na^+/Na or vs. Li^+/Li for the blue and yellow hexagons, respectively) and volumetric energy density (Wh/L) vs. volumetric capacity (Ah/L) for selected positive electrode materials for Na- and Li-ion batteries. The mass and volume of the active electrode material have been taken into account to calculate the capacity and energy density.This figure is reproduced from the publication by Clément et al. [5].

1.5 Polyanionic multi-redox cathodes for alkali-ion batteries

Polyanionic cathodes are cathodes that contain polyanion groups as part of their chemical formula. In addition, not all polyanionic cathodes have polyanion groups as their only anionic component, and such materials are called mixed-polyanion cathodes. A large variety of polyanionic chemistries have been demonstrated as functional Li- and Na-ion battery cathode materials, including, but not limited to, $(PO_4)^{3-}$ [109, 110], $(P_2O_7)^{4-}$ [111, 112], $(SO_4)^{2-}$ [113], $(CO_3)^{2-}$ [114, 115], and $(BO_3)^{3-}$ [116]. The polarity of the anion group and its bonds will influence the overall electronic band structure of the cathode and its transition metal components, in turn influencing the redox reaction voltage for each specific chemistry and structure. This influence of the anion polarity on the transition metal redox is called the inductive effect [42, 6]. Since each specific polyanion chemistry influences the specific voltage, the choice of transition metal with polyanion groups opens a wide chemical space in which redox reactions may occur at a large variety of voltages. Stated differently, the average redox reaction voltage of a cathode may be tuned by specific chemical choices during materials design.

Though higher average voltages improve cathode energy density, they also make batteries less safe. At high voltages when alkali ions are extracted, the cathode is oxidized, increasing its chemical potential of oxygen, and in certain cases causing the material to decompose, releasing oxygen gas, which, as discussed in Section 1.3, may lead to thermal runaway [19]. This makes polyanionic cathodes desirable because they are less likely, in general, to release oxygen at high voltages than oxide cathodes due to the strong bonding of oxygen in polyanion polyhedra [6]. As a result,

polyanionic cathodes can exhibit redox activity at higher average voltages than oxide systems while maintaining adequate safety [117, 118].

While polyanionic cathodes may be safer, they are usually less energy-dense than oxide materials. Since polyanion groups have a relatively high mass and volume compared to their charge, their theoretical capacity, and thus their energy density, is lower than that of the best oxide materials. Despite this, $LiFePO_4$ has gained some commercial success for its ability to perform well in high power systems, as discussed previously. $LiFePO_4$ is the only polyanionic alkali-ion cathode material that has been commercialized to date. However, the capacity disadvantage Na-ion polyanionic cathodes face versus oxide cathodes in the half-cell research format with a Na metal anode may be diminished when tested as a full cell with a carbon-based anode. The Tarascon group has recently shown that when tested in a full cell with a hard carbon anode, which is currently the leading Na-ion battery anode, optimized $Na_{3+x}V_2(PO_4)_2F_3$/hard C systems exhibited an energy density of 265 Wh/kg versus 235 Wh/kg in an optimized $Na_1(Fe_{1/2}Mn_{1/2})O_2$/hard C system [119]. This is one example of how chemical and stability considerations may benefit future polyanionic chemistries.

In order for capacities in polyanion-based alkali-ion cathodes to surpass those seen in oxide cathodes, more than one working ion must be cycled per transition metal ion. To date, the only Li-ion battery intercalation materials to achieve this reversibly have been $Li_{1+x}VPO_4F$, $Li_{1+x}FePO_4F$, and $Li_{1+x}TiPO_4F$, which are all polyanionic tavorite-structured Li-ion battery cathodes [80, 120]. For Na-ion batteries, only NASICON-structured $Na_3V_2(PO_4)_3$ has been demonstrated to reversibly cycle more than one sodium ion per transition metal [48]. While polyanionic multi-redox cathodes for alkali-ion batteries are rare, the vast chemical space that exists, both previously explored, postulated, and previously unknown, means that more

such cathodes likely exist. In addition, while looking in this chemical space for specific chemistries is a daunting task, leveraging the Ceder Group's aptitude for computationally guided materials aids in this search.

1.6 Computationally guided materials discovery for batteries

The Ceder Group, formerly of MIT and currently at UC Berkeley and Lawrence Berkeley National Laboratory, uses a joint computational-experimental approach to explain the fundamental mechanisms that govern alkali-ion battery performance. While Li-ion batteries have been heavily researched over the past 40 years, improvement on these technologies is still required and is continuously occurring. In contrast, Na-ion batteries are comparatively less explored due to their lower voltages and energy densities in existing materials; therefore, the Ceder Group conducts research on this topic due to potential opportunities for meaningful contributions that exist in this developing field. $LiCoO_2$ and $LiFePO_4$, which are leading Li-ion battery cathode materials, exhibit energy densities around 600 Wh/kg at reaction voltages of 4 V and 3.5 V, respectively. These values serve as targets for the performance of any new materials that are discovered in the Ceder Group.

One approach to aid in the search for novel alkali-ion cathodes is employing high-throughput screening algorithms to accelerate the materials discovery process. The properties of different metal-ligand combinations, including thermodynamic stability, voltage, capacity, and safety can be calculated in different crystal structures via fast, efficient computational methods [121, 6]. As such, high-throughput screening can be used to predict candidate battery materials that are either novel structures,

chemistries, or compounds that are known to exist but have not been explored as batteries. Although computational methods can screen for some vital properties of potential electrode materials, they can only provide direction to guide synthesis and processing. Ultimately, experiments are needed to find synthesis routes and examine rate kinetics, cyclability, and other important electrochemical properties. The work in this thesis focuses specifically on the discovery of new cathode materials, and high-throughput screening has been successfully used as a tool in cathode material discovery for both Li- and Na-ion batteries in the past [122, 123, 7, 114]. Thus, the first-principles calculation and high-throughput screening methods employed by the Ceder Group are well suited to guide the discovery of polyanionic alkali-ion battery cathode that can undergo multiple redox reactions during cycling [124, 19].

Another approach to aid materials discovery using computation is through a more focused examination of a specific class of materials. This computational approach usually begins as an experimental observation of a particular behavior in a material and then uses computation to explain the phenomena and inform intelligent design of new materials in this class. One such case of this "low throughput" approach was that of disordered-rocksalt Li-excess cathodes in the Ceder Group. Upon the observation of very high performance in cation-disordered $Li_{1.211}Mo_{0.467}Cr_{0.3}O_2$ cathodes, computational examination of this previously unexplained performance yielded the discovery of percolating fast-diffusion, or 0-TM, channels in Li-excess structures of this type [125, 126]. From this understanding, new cathodes could be designed with this new computational guidance in order to incorporate percolating 0-TM channels in novel chemistries, leading to the discovery of $Li_xNi_{2-4x/3}Sb_{x/3}O_2$ and $Li_{1.25}Nb_{0.25}Mn_{0.5}O_2$ [127, 128]. In this way, computational guidance stemming from a specific observation may also guide the discovery of new materials via a more narrow approach.

1.7 Capacity limits in alkali-ion battery cathodes

In this thesis, the predicted multi-redox cathode materials are synthesized and characterized electrochemically. Often, prospective cathode materials exhibit capacities below their theoretical maxima. Commonly, the observed shortfall in capacity below theoretical values occurs due to one or more of three primary reasons: structural/thermodynamic stability, working ion mobility, and limited transition metal redox activity.

1.7.1 Structural/thermodynamic stability limits

When a battery is charged, the working-ion concentration in the cathode decreases and the vacancy concentration increases. It is possible that the vacancy concentration within the transition metal-anion scaffold of the cathode crystal structure becomes high enough that the structure is no longer thermodynamically unstable. If this happens, there is a thermodynamic driving force for the structure to decompose to its new ground state. If this structural decomposition proceeds, the working ion will be unable to reinsert into the cathode during discharge. Such decomposition can occur gradually over many charges or quickly during a single charge. In the case of $LiCoO_2$, the capacity limitation caused by thermodynamic stability issues at high Li-vacancy concentration is well know [21, 129]. As a result, $LiCoO_2$ cathodes have their operational capacity limited to approximately 150 mAh/g, corresponding to Li concentrations between $LiCoO_2$ and $Li_{0.5}CoO_2$. If $LiCoO_2$ is cycled beyond this range of Li composition it will undergo an irreversible spinel-like structural transformation, dramatically decreasing the cathode capacity. Li-excess cathodes, or oxide cathodes in which the lithium concentration exceeds the overall transition metal concentration in the discharged state, also suffer from structural stability limits on their capacity.

This family of cathode materials has risen to prominence in the literature after capacities greater than 200 mAh/g were demonstrated, but is frequently hampered by structural instabilities at high voltages that give rise to phase transitions and degradation upon repeated cycling [130, 131, 132, 133].

1.7.2 Working ion diffusion limits

Working ion mobility is the ease with which the working ion can move out of and back into a cathode upon cycling. The energy required to move a working ion requires additional energy beyond that required to perform the necessary redox reaction and manifests itself as an overpotential during electrochemical cycling. The mobility of the working ions in cathodes may inhibit the amount of capacity that may be reversibly achieved under testing conditions depending on the energy barrier that must be overcome to move the working ion. Further, ion mobility is frequently concentration dependent and may change during cycling. Layered oxide cathodes for Li-ion batteries again act as an example of this behavior. For the layered oxide structure, the spacing between each layer changes with lithium content, and with it the Li-ion mobility also changes. A decrease in layer spacing of 4% can increase the energy requires to diffuse Li by as much as 200%, which can diminish the amount of extractable Li within a reasonable testing window [134].

In general, battery cathodes exhibit higher capacity at slow charge and discharge rates. At slow rates the kinetic effects, such as some observed overpotentials, are diminished [135]. Most frequently, Galvanostatic cycling tests are used at rates of between C/20 for "good" conducting cathodes, such as Na-ion layered oxides [105, 99], and C/200 for "very poor" conducting cathodes, such as Li-ion fluoride conversion cathodes [90]. However, it is possible that even at very slow rates, kinetic limitations

may still be present. To diminish such effects as much as possible, Galvanostatic or Potentiostatic Intermittent Titration Techniques (GITT and PITT, respectively) are used. Such techniques allow for near-equilibrium cycling data to be collected [135, 136], which allows for alkali extraction to be maximized. As such, using these methods may circumvent some ion mobility issues in examined materials when exploring the potential of a new material. Even so, diffusion barriers in a material may still prevent cycling of the theoretical maximum capacity.

1.7.3 Redox activity limits

The third major source of capacity limitations in alkali-ion battery cathodes stems from impediment of the oxidation or reduction reaction that accompanies Li or Na extraction/insertion. As discussed in Section 1.2, during battery charging, the cathode's active transition metal is oxidized as an alkali ion is removed and reduced on discharge when that ion is inserted into the cathode. Redox activity of the transition metal is required, and intercalation cannot proceed without it. Therefore, if the redox reactivity of the cathode is inhibited, so is the cathode capacity. Whether or not a transition metal is capable of reversible activity in a particular environment is determined by the specific electronic structure of each species in that particular environment. Again, using layered Li-ion oxide cathodes as an example, the stringent electronic structure requirements on transition metal ions in the layered structure limits the active chemistry of cathode oxides to just cobalt and nickel [137, 138]. For other $LiMO_2$ chemistries, reversible capacity is negligible as a result of this stringent redox limit. However, the redox activity in layered oxide cathodes is less limited for Na-ion batteries, occurring for Ti-, V-, Mn-, Fe-, Co-, Ni-, and Cr-containing chemistries, as mentioned in Section 1.5 [32, 62].

1.8 Synthesis and Characterization

After identification of a predicted new alkali-ion battery material, a compound must first be synthesized and then characterized to determine its ultimate potential. For this initial stage, the synthesis methods by which potential cathode materials are made do not need to be scalable, or otherwise commercially viable. If a material proves to be promising for eventual commercialization, new synthesis routes that are cheaper and more scalable may be explored.

1.8.1 Synthesis methods for predicted cathodes

The primary synthesis methods used for making alkali-ion cathode materials, both in this work and the literature, are solid-state and hydrothermal methods. Other less commonly used synthesis methods have been demonstrated in the literature, such as ionothermal [139], mechanochemical [140], and co-precipitation methods [141], but these will not be discussed for brevity.

Solid-state synthesis is the most common method used to make battery cathode materials. In this method, precursors are mixed and/or ground together to create a well-mixed powder, which is frequently pelletized in order to densify the mixture and bring precursors into more intimate contact, before being brought to an elevated temperature. When heated, the reactivity of the components increases, making the conditions favorable for ceramic synthesis reactions to occur. Frequently, volatile species from the precursors are released during the reaction. Depending on the precursors and the desired synthesis product, an inert, oxidizing, or reducing atmosphere may be used to alter the valence state of the transition metal species during synthesis.

Nearly all synthesizeable layered oxide alkali-ion cathode materials can be made using solid-state synthesis methods[6, 104, 33, 79, 96]. Synthesis of polyanionic cath-

odes using this method is also common, but the feasibility of solid-state synthesis depends on the specific anion chemistry and stability of the targeted product [49, 142, 50, 32, 143, 74]. In general, due to the strong binding in oxides, higher input of thermal energy is required to synthesize oxide-based cathodes, commonly 800^oC-900^oC, compared to polyanionic materials, which are frequently synthesized at 500^oC-750^oC. The chosen reaction environment, however, depends solely on the transition metal valence state in the precursor used and the transition metal valence state in the target compound. For vanadium, which is present in layered $LiVO_2$, NASICON, and tavorite structures, the most commonly used precursor is V_2O_5. To bring the valence to V^{3+}, which is present in the desired cathode structures, the compounds are synthesized in a reducing H_2 environment [79, 96, 144]. It is also possible to use solid-state reducing agents in synthesis. For example, Shakoor et al. use high surface area carbon black as a reducing agent to reduce V_2O_5 in the solid-state synthesis of $Na_3V_2(PO_4)_2F_3$ [49]. In the case of Fe, Co, Mn, Ni, and Ti, Ar gas environments are common during firing, as precursors with metal valences of 2+ or 3+, are readily available [6, 104, 33, 142, 50, 32, 143]. It is possible, though, to alter a metal's valence state from the precursor if certain intermediate precursors are more readily reacted. For example, Komaba et al. synthesized their high-performing $NaNi_{0.5}Mn_{0.5}O_2$ in air to oxidize transition metals in $Ni_{0.5}Mn_{0.5}(OH)_2$, which was made using co-precipitation methods for use as an intermediate precursor [105].

The next method commonly used to make alkali-ion battery cathode materials is hydrothermal synthesis. This method involves the formation of compounds at elevated temperatures and pressures in a closed aqueous environment. A variety of polyanionic cathodes have been made in this manner, along with compounds of interest including carbonophosphates [7], hydroxy- and oxyphosphates [140, 141], and phosphates [145]. In general, temperatures are much lower in hydrothermal

synthesis than in solid-state synthesis. High temperatures are generally not used for two reasons: 1) The mobility/activity of ions in solution far exceeds that in solids making high temperatures unnecessary and 2) aqueous reactions at temperatures exceeding the critical point of water ($\sim$374^{o}C) are difficult to perform and require built-for-purpose reaction vessels such as Tuttle-type reactors [146], which drastically limits the accessibility of such reactions methods.

The most widely used reaction vessel for hydrothermal synthesis is a PTFE-lined stainless steel autoclave. These devices are filled with the precursor solutions, sealed, and heated to a maximum of 250^{o}C, above which the PTFE lining would soften. The system variables include temperature, pressure, pH, solute concentration, reaction duration, and degree of filling of the autoclave. While all these variables, with the exception of pressure, can be directly controlled, their effects on the experimental result are difficult to separate since the hydrothermal synthesis vessel is a closed system, which presents significant challenges to experimental design. However, the major benefits of this method are the increased mobility of ions in liquids compared to solids, and a greater likelihood of forming metastable and slightly stable products. These facts make hydrothermal synthesis a desirable method when attempting to explore new chemistries, especially those predicted to have limited stability.

1.8.2 Characterization of synthesis products

Once a synthesis reaction is completed, the phase composition of crystalline synthesis products is conducted using x-ray diffraction (XRD). For an XRD measurement, coherent x-ray radiation is diffracted through the crystal structure(s) in the synthesis product through a range of angles, generating a characteristic spectrum that can be used to identify the crystalline phases in the sample. However, while XRD gives

insight into crystal structure, implying a likely sample chemistry, additional elemental analysis is usually needed. One method to analyze sample composition is Inductively Coupled Plasma atomic emission spectroscopy (ICP-AES), which is used in Chapter 2 of this thesis.

1.8.3 Electrochemical characterization of prospective cathode materials

To electrochemically characterize synthesized cathode materials, composite electrode films are used. They are generally made using a doctor-blade or dry-rolling method and tested in two- or three-electrode electrochemical cells. In general, cathode capacity is maximized at slow charge and discharge rates. This is because at low rates the effects of slow kinetics, such as polarization, are diminished [135]. Most frequently, Galvanostatic, or constant current, cycling tests are used. Galvanostatic or Potentiostatic Intermittent Titration Techniques (GITT and PITT, respectively) are sometimes used so that near-equilibrium cycling performance to be evaluated.

1.8.4 *In situ* studies of alkali-ion cathodes

In situ characterization methods have emerged as a powerful tool in the study of alkali-ion batteries. Foremost among them is *in situ* XRD. In this technique, a battery cell is cycled while diffraction patterns of electrode active materials are simultaneously collected at varying states of charge. Thus, real-time changes in lattice parameters and structure during electrochemical cycling may be observed *in situ*.

In situ studies of widely used Li-ion cathode materials have provided a great deal of insight into lithiation mechanisms and performance limitations in different systems. For example, *in situ* XRD of $LiMnO_2$ revealed a spinel-like structural

transformation that leads to significant irreversible capacity [147]. In addition, *in situ* XRD provided experimental evidence of a non-equilibrium solid-solution lithiation path in $LiFePO_4$ [148, 149]. *In situ* XRD has also been used as a way to characterize the many structural changes that occur during the cycling of layered oxide Na-ion cathode materials [95, 150]. While frequently used for gaining a better understanding of established cathode materials, *in situ* XRD can also be an invaluable tool in characterizing new materials and finding limits in their performance.

Battery cells designed for utilization of *in situ* XRD are generally built-for-purpose depending on the x-ray source employed in the measurement. A cathode, anode, separator, electrolyte, and current collectors are sealed in an aluminum [151] or polymer [152] frame. For *in situ* cells, a portion of the casing is removed and replaced with a beryllium window, since beryllium is transparent to x-rays, and, as such, will not diminish the observed intensity in the measured spectra. A schematic of the cell used in the Ceder Group is shown in Figure 1-8.

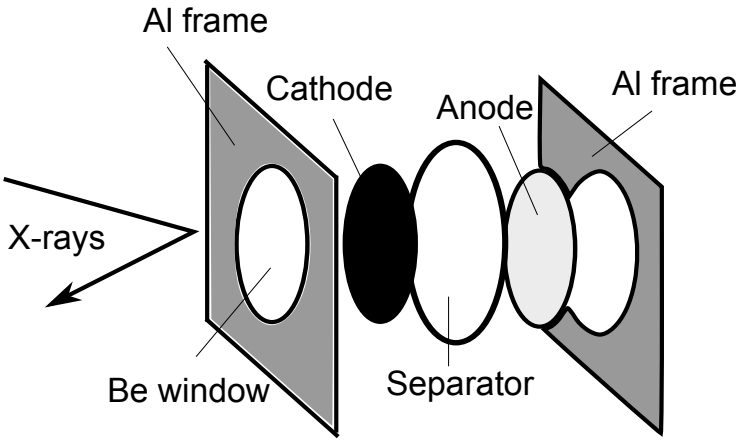

Figure 1-8: A schematic diagram of a battery cell used for *in situ* XRD measurements by the Ceder Group.

High flux x-ray sources, such as synchrotron radiation, are often used for *in situ* XRD measurements. Battery cathodes are generally composites containing small particles and, as a result, are weak scatterers. A high-flux source increases the observed signal, allowing a high-resolution spectrum to be taken in a shorter time than with a laboratory XRD so more spectra can be collected during each cycle. The high energy of synchrotron radiation allows for a greater x-ray penetration depth and also contributes to a larger signal from the cathode film, which is below the beryllium window and a current collector. Laboratory diffractometers may also be used to conduct *in situ* testing, as in Chapter 3 of this work, but such measurements are more challenging because they use a lower-power x-ray source [153].

1.9 Thesis overview

This thesis examines novel polyanionic chemistries as possible multi-redox cathodes for alkali-ion batteries using a computationally-informed approach. A number of synthesis approaches are used in this work, and once synthesized, the prospective cathodes are characterized electrochemically. Special attention is paid to identifying and explaining the underlying mechanisms by which cathode performance is limited when such issues are encountered. The first part of the thesis covers the synthesis, electrochemical characterization, and limitations of novel carbonophosphate cathode chemistries for Li-ion batteries. The second part of the thesis examines mixed-TM compositions of fluorophosphate for Na-ion batteries using a joint experimental-computational approach to explain observed cycling phenomena.

Chapter 2 establishes the two-step hydrothermal synthesis method used in the synthesis of computationally-predicted Li-containing carbonophosphate cathodes, specifically $Li_3Fe_{0.2}Mn_{0.8}CO_3PO_4$, and explores their electrochemical performance,

redox-active species, and the thermodynamic limits to electrochemical performance. **Chapter 3** demonstrates Na insertion in $Na_3V_2(PO_4)_2F_3$, discusses the synthesis and electrochemical performance of $Na_3[M]_2(PO_4)_2F_3$ with [M] = {V, Ti, Fe} as cathodes for Na-ion batteries, as well as the design and use of $Na_3GaV(PO_4)_2F_3$ as a test system for elucidating the limiting mechanisms in fluorophosphate Na-ion cathodes. **Chapter 4** concludes the thesis.

Chapter 2

Carbonophosphates as computationally-predicted Li-ion battery cathodes

2.1 Electrochemical Properties of $Li_3Fe_{0.2}Mn_{0.8}CO_3PO_4$ as a Li-ion battery cathode

2.1.1 Introduction

The need for lithium-ion batteries with higher energy density than existing materials has led to significant efforts to discover new cathode materials [154, 24, 7]. High-throughput *ab initio* computation is one effective approach employed to accelerate the process of materials discovery that has led to the identification of several novel lithium intercalation materials [6, 7, 122, 155]. One class of novel materials that has been predicted to function as intercalation cathodes for Li-ion batteries is lithium-

containing carbonophosphate compounds [6]. $Li_3FeCO_3PO_4$ and $Li_3MnCO_3PO_4$ are of particular interest. As shown in Table 2.1, which depicts data first reported by Chen et al. [7], both compounds are predicted to have accessible 2+ to 3+ redox couples, but the 3+ to 4+ couple in the manganese-containing compound is also expected to be active at 4.1 V, a voltage compatible with existing electrolytes. As a result, $Li_3MnCO_3PO_4$ is of the greatest interest because it has a two-electron theoretical capacity of 231 mAh/g and average voltage of 3.7 V. As polyanionic cathodes, lithium-containing carbonophosphates could also be preferred over oxide cathode materials since they are generally less likely to release oxygen at high voltages [6].

Table 2.1: A comparison of predicted voltages of redox couples and theoretical capacities of $Li_3[M]CO_3PO_4$ for [M] = {Fe, Mn} calculated in Chen et al. [7].

$Li_3[M]CO_3PO_4$

[M]	*Redox*	*Predicted Voltage*	*Theoretical Capacity between 2 V–5 V*
Fe	$2^+/3^+$	3.0 V	230 mAh/g
	$3^+/4^+$	4.6 V	
Mn	$2^+/3^+$	3.2 V	231 mAh/g
	$3^+/4^+$	4.1 V	

The synthesis and characterization of both $Li_3FeCO_3PO_4$ and $Li_3MnCO_3PO_4$ have been previously reported [7]. Lithium-containing carbonophosphates are not thermodynamic ground states, so the compounds are synthesized using ion-exchange techniques from the thermodynamically stable sodium carbonophosphates of the same crystal structure. As reported previously by Chen et al., $Li_3FeCO_3PO_4$ has a theoretical capacity of 115 mAh/g and can be easily synthesized using ion exchange methods. This compound cycles reversibly, close to its one-electron theoretical ca-

pacity at a rate of C/5. In contrast, $Li_3MnCO_3PO_4$ shows a discharge capacity of 135 mAh/g on its first discharge at a rate of C/100, which is only ∼58% of its theoretical two-electron capacity. In addition, the capacity of $Li_3MnCO_3PO_4$ degrades dramatically in subsequent cycles. The poor performance in $Li_3MnCO_3PO_4$ could be due to many factors. However, it is believed that one major cause is the residual sodium (∼17%) ions sitting on Li sites as a result of an incomplete ion exchange during synthesis. In contrast, the better-performing $Li_3FeCO_3PO_4$ shows no residual sodium after synthesis [7].

The approach employed is to substitute some manganese in $Li_3MnCO_3PO_4$ with iron to improve its performance by imparting the ion-exchangeability and cycling performance of the $Li_3FeCO_3PO_4$ on to $Li_3MnCO_3PO_4$. Similar mixing techniques have been used in previous attempts to improve the performance of α-$LiMnPO_4$ [156, 157, 158]. In this thesis $Li_3Fe_{0.2}Mn_{0.8}CO_3PO_4$ is focused on specifically. Since complete Li-Na exchange is much easier to perform in $Li_3FeCO_3PO_4$ than in $Li_3MnCO_3PO_4$, it is expected that this compound to ion-exchange more completely from its sodium-containing parent compound than $Li_3MnCO_3PO_4$.

2.1.2 Experimental methods

Hydrothermal synthesis and ion exchange

$Na_3Fe_{0.2}Mn_{0.8}CO_3PO_4$ was synthesized using a hydrothermal synthesis method [7]. Two clear solutions were made with $FeSO_4{\cdot}7H_2O$ (J. T. Baker) and $Mn(NO_3)_2{\cdot}4H_2O$ (Sigma Aldrich), and Na_2CO_3 (Alfa Aesar, 99.5%) and $(NH_4)_2HPO_4$ (Alfa Aesar, 98%), respectively. The combined molar ratio of transition metal cations was 1:7 to carbonate ions and 1:1 to phosphate ions. The solutions were mixed in a glass bottle, heated in an oil bath to 130^{o}C and magnetically stirred for 44 hours. The

solution mixing and subsequent heating was completed in an Ar-flushed glove box. Next, the reaction products were separated from the reaction solution and washed by centrifuging in the native solution followed by centrifuging in methanol, distilled water, and methanol again. The wet powder was dried overnight in a vacuum oven at 50^{o}C.

$Li_3Fe_{0.2}Mn_{0.8}CO_3PO_4$ was made from its sodium-containing precursor via a Li-Na ion-exchange method. As-synthesized sodium carbonophosphate was added to a 2 M solution of LiBr in 1-hexanol [159]. The suspension was stirred magnetically for 5 days in a 140^{o}C oil bath in an Ar atmosphere. The product was centrifuged to separate it from the ion-exchange solution, and was then washed in methanol, water, and methanol again. The wet powder was dried in a vacuum oven overnight at 50^{o}C.

The ion-exchange product was then ball-milled with carbon in a Retsch PM200 planetary ball mill to improve the material's electrochemical performance through decreased particle size and carbon coating [160, 161]. Zirconia-lined milling jars were loaded with $Li_3Fe_{0.2}Mn_{0.8}CO_3PO_4$ and carbon (Super P) in a weight percent ratio of 85:15 in an Ar-filled glove box. The sample was milled for 6 hours at 500 rpm, and the resultant powder was also unloaded in the Ar-filled glove box to limit air exposure.

Carbonophosphate sample characterization

Pristine powder samples of the sodium and lithium carbonophosphates were characterized by XRD using a Bruker D8 Advance diffractometer (Molybdenum Kα, λ=0.7017Å). Elemental composition of the lithium carbonophosphate material was verified by Inductively Coupled Plasma atomic emission spectroscopy (ICP) measurements using a Horiba Jobin Yvon, ICP-AES (ACTIVA-S) in MIT's Center for

Materials Science and Engineering (CMSE). For the ICP measurement, the sample powders were first dissolved in 2% nitric acid, which itself was prepared from concentrated nitric acid and ASTM grade I deionized water. The diluted nitric acid was also used as a control solution. Calibration curves were constructed using five calibration solutions of different concentrations for each measured element in 2% nitric acid. All measurements for each element were repeated three times and had a relative standard deviation of less than one percent.

To electrochemically characterize the $Li_3Fe_{0.2}Mn_{0.8}CO_3PO_4$ powder cathode films were made using the as-prepared sample mixed with PVDF and carbon (Super P) such that the overall ratio of components was 6:1:3 weight percent, respectively. The films were made using a doctor-blade method on aluminum current collectors, with each electrode containing $\sim$2 mg of active material. CR2016 coin cells were assembled in an Ar-filled glove box with a Li metal foil anode, Celgard 2025 separator (Celgard Inc., U.S.A.), and 1 M solution of $LiPF_6$ in ethylene carbonate/dimethyl carbonate (1:1) as electrolyte. Galvanostatic experiments were conducted at a rate of C/50 on an Arbin Instruments (College Station, TX) battery cycler.

2.1.3 Experimental results

The sodium-containing carbonophosphate sample is tan in color, while the lithium-containing carbonophosphate sample is light beige, which is consistent with previously reported results [7]. The XRD patterns of synthesized phase-pure $Na_3Fe_{0.2}Mn_{0.8}CO_3PO_4$ and $Li_3Fe_{0.2}Mn_{0.8}CO_3PO_4$ samples are shown in Figure 2-1. The pre- and post-ion exchange spectra exhibit substantial differences, but are consistent with differences between Li- and Na-containing carbonophosphate phases for other transition metals [7]. Substantial peak broadening is seen in the

$Li_3Fe_{0.2}Mn_{0.8}CO_3PO_4$ sample, which implies that either a substantial quantity of defects is present in the sample or that there are very small crystal domains in the ion-exchanged sample. Elemental analysis of the $Li_3Fe_{0.2}Mn_{0.8}CO_3PO_4$ sample was conducted using ICP analysis, the results of which are displayed in Table 2.2. It is evident that the Li-Na ion exchange proceeded almost entirely (>99%) to completion. The other elements are also present in very close to the desired ratio, with the exception of iron, which is in excess. The most likely explanation is that some amorphous Fe-containing phase formed during the ion exchange reaction in 1-hexanol, as has been previously hypothesized [7].

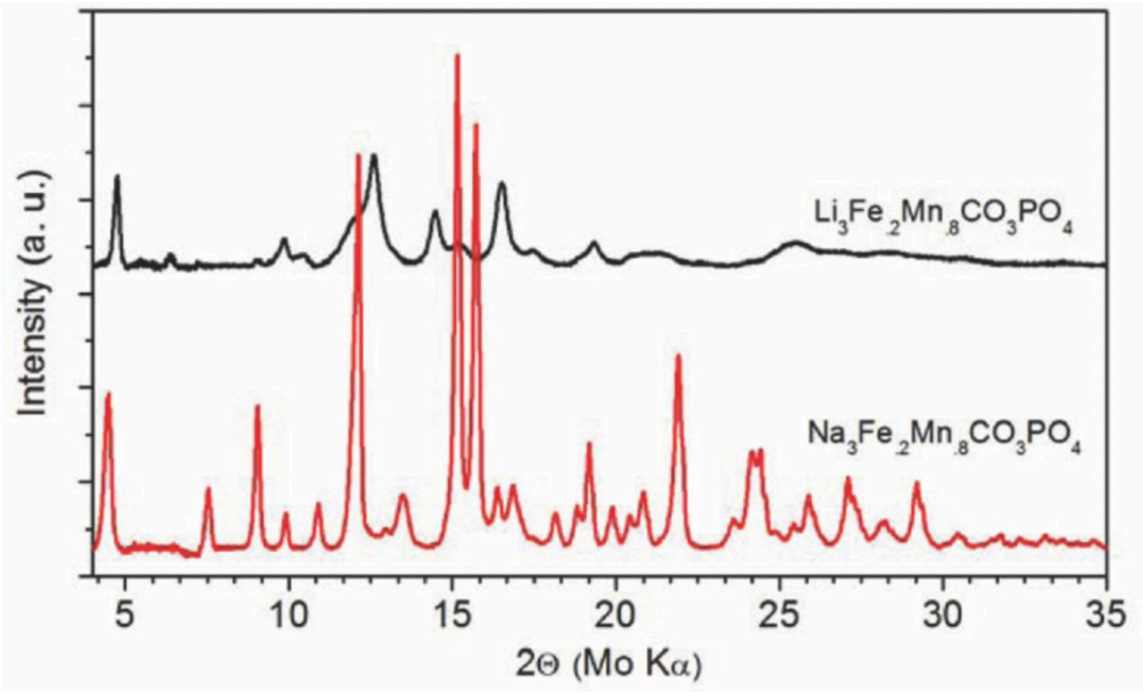

Figure 2-1: XRD spectra of as-prepared $Na_3Fe_{0.2}Mn_{0.8}CO_3PO_4$ and $Li_3Fe_{0.2}Mn_{0.8}CO_3PO_4$ samples.

Electrochemical testing of the $Li_3Fe_{0.2}Mn_{0.8}CO_3PO_4$ cathodes was conducted at

Table 2.2: Elemental composition of as-synthesized $Li_3Fe_{0.2}Mn_{0.8}CO_3PO_4$ obtained using ICP analysis.

Element	*mg/L*	*Normalized Molarity*
Li	34.49	2.97
Na	0.89	0.02
Fe	24.30	0.26
Mn	73.18	0.80
P	49.14	0.95

a rate of C/50 at room temperature in a 2.00–4.75 V window. The voltage versus capacity data for one of these tests is shown in Figure 2-2a. As seen in the figure, the first-cycle charge starts at greater than three volts, and exhibits a charge capacity of 284 mAh/g, which exceeds the material's theoretical capacity of 231 mAh/g. The high starting voltage and the differing behavior in subsequent cycles indicate that the Fe^{2+} in the prepared sample was oxidized during processing, likely as the result of some exposure. The high charge capacity on the 1^{st} cycle is believed to be caused by irreversible Li^+-extraction from an amorphous impurity phase left on the sample surface from synthesis, which is also indicated by the excess of iron seen in the ICP analysis of the ion-exchanged sample. The 1^{st} discharge shows a capacity of 147 mAh/g, but the capacity of the sample reduces over the course of the first 4 cycles to a reversible value of approximately 105 mAh/g, or 0.9 Li^+ per formula unit. This decrease is not believed to be the result of traditional cathodic capacity fade, but instead the result of irreversible cycling of amorphous iron-containing impurity phases between 2.5 V and 2.0 V. These impurities are likely iron-containing hydroxides or oxyhydroxides, which have been previously been shown to intercalate Li^+ at voltages in this region [162]. As shown in Figure 2-2a, the difference in discharge capacity between the 1^{st} and 18^{th} cycles stems primarily from decreased capacity in this low-

voltage region.

On charges following the first cycle, a distinct plateau is present near 3.0 V, which is the predicted voltage of the Fe^{2+}/Fe^{3+} and near that of the Mn^{2+}/Mn^{3+} couple [24]. The plateau approximately corresponds to the theoretical capacity of iron in $Li_3Fe_{0.2}Mn_{0.8}CO_3PO_4$, which is 23 mAh/g. Additional plateaus or other distinct features indicative of further redox activity are less apparent, and are discussed later.

The capacity retention of $Li_3Fe_{0.2}Mn_{0.8}CO_3PO_4$ is displayed in Figure 2-2b. Both the charge capacity and discharge capacity drop significantly over the first 4 cycles; from 284 mAh/g to 120 mAh/g and from 143 mAh/g to 108 mAh/g, respectively. After the 4^{th} cycle the charge and discharge capacity remain relatively constant, and drop only $\sim$5 mAh/g over the next 20 cycles. In addition, significant coulombic inefficiency is observed, with the charge capacity consistently being about 10 mAh/g higher than the discharge capacity after the 4^{th} cycle. This is likely the result of electrolyte decomposition at high voltage.

2.1.4 Discussion of $Li_3Fe_{0.2}Mn_{0.8}CO_3PO_4$ electrochemistry

The biggest attraction of $Li_3MnCO_3PO_4$ is the potential existence of two active redox couples in the voltage window of existing battery electrolytes. The proposed two-electron activity leads to a high theoretical capacity of 231 mAh/g. To improve the performance of the pure $Li_3MnCO_3PO_4$, $Li_3Fe_{0.2}Mn_{0.8}CO_3PO_4$ was synthesized, and its electrochemical performance is shown above. Of the 208 mAh/g theoretical capacity of the material, only about 105 mAh/g can be reversibly cycled for greater than 20 cycles. Despite performance well under theoretical values, this demonstrates a significant improvement over the previously reported performance of $Li_3MnCO_3PO_4$, which showed much poorer cyclability. In addition, $Li_3Fe_{0.2}Mn_{0.8}CO_3PO_4$ has a

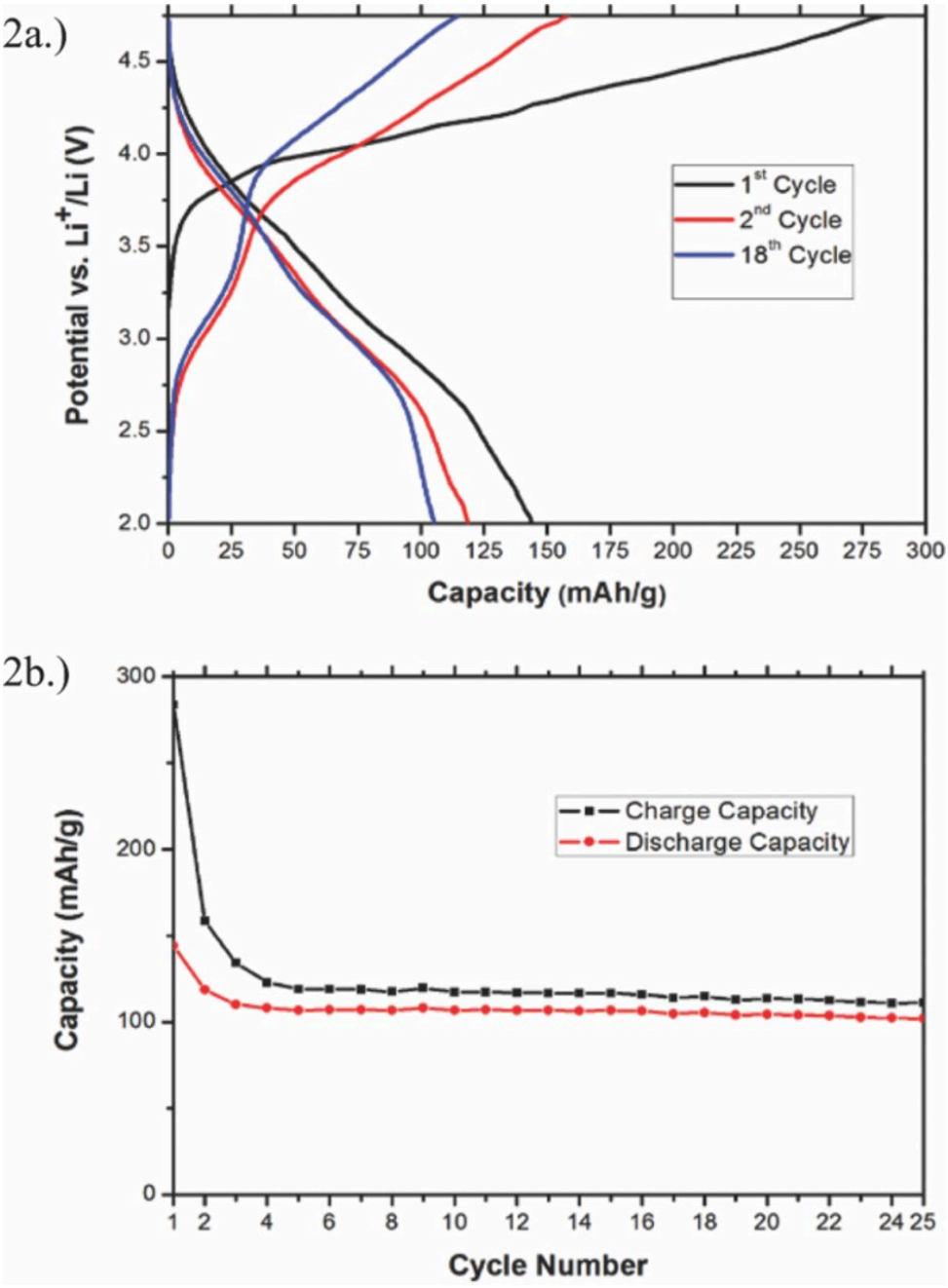

Figure 2-2: (a) Voltage profile and (b) capacity retention of $Li_3Fe_{0.2}Mn_{0.8}CO_3PO_4$ cycled between 2 V and 4.75 V. The galvanostatic tests were performed at room temperature at a rate of C/50.

larger energy density than $Li_3FeCO_3PO_4$. While the reversible discharge capacity for these materials is approximately the same, the average discharge voltage in $Li_3Fe_{0.2}Mn_{0.8}CO_3PO_4$ is 0.4 V higher, corresponding to an energy density 40 Wh/kg larger than in $Li_3FeCO_3PO_4$.

To examine the activity of Fe^{2+}/Fe^{3+}, Mn^{2+}/Mn^{3+}, and Mn^{3+}/Mn^{4+} redox couples more in depth, which are all predicted to be accessible in the tested voltage window, the differential charge (dQ/dV) capacity versus voltage is shown in Figure 2-3 for several cycles. Two charge peaks and two discharge peaks are clearly visible. The first set of peaks around 3.0 V most likely correspond to overlap of the Fe^{2+}/Fe^{3+} and Mn^{2+}/Mn^{3+} couples, computed to exist at 3.0 V and 3.2 V, respectively. It has been previously reported that Fe^{2+}/Fe^{3+} and Mn^{2+}/Mn^{3+} couples move closer together when mixed in single-phase Li(Fe, Mn)PO_4 [163], and similar behavior could be present in this system. The second set of peaks near 4.0 V corresponds to the predicted Mn^{3+}/Mn^{4+} activity in the active material. The slight shift seen in the second set of peaks over the first 12 cycles likely indicates that structural changes may be occurring in the material. In addition, the area of the peaks is noticeably different upon charge and discharge, which may be caused by slow ion mobility and thus Li concentration gradients in the material during cycling, even at these slow rates. Specifically, the area under the 3 V charging peak is smaller than the area of the 3 V discharge peak. Finally, the upturn at the high end of the charging curve on Figure 2-3 indicates that electrolyte oxidation may be occurring. This idea is reinforced since none of this observed charge capacity is returned on discharge, and explains the coulombic inefficiency seen in Figure 2-2b.

The observed voltage of the Mn^{2+}/Mn^{3+} redox couple shows one potential advantage carbonophosphate cathodes hold over oxide cathodes. The inductive effect of the carbonate and phosphate polyanions causes the Mn^{2+}/Mn^{3+} redox couple's

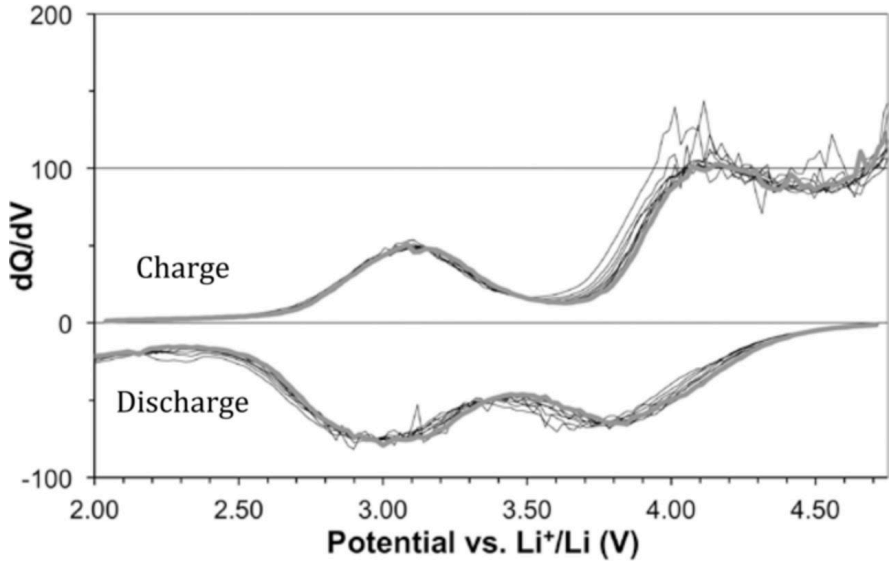

Figure 2-3: Curves showing the differential charge plotted for a $Li_3Fe_{0.2}Mn_{0.8}CO_3PO_4$ cell for its 3rd through 12th cycles. The reader should focus mainly on the envelope of the curves. The 1st and 2nd cycles are omitted for clarity.

voltage to be higher (3.2 V) than in oxide materials [164]. However, the inductive effect in this mixed-polyanion system is not as large as that in pure phosphates, making both Mn redox couples lie in a useable voltage window, in contrast to $LiMnPO_4$. In order to improve $Li_3Fe_{0.2}Mn_{0.8}CO_3PO_4$, the capacity fading of the material and its limited Li^+ extraction must be addressed. In addition, the material's ionic and electronic conductivity would also need to be improved.

While this work demonstrates preliminary results of carbonophosphates as Li-ion cathode materials, a number of aspects of this materials performance remain to be understood. One notable unexplained cycling feature is the apparent asymmetric capacity seen in the Mn^{2+}/Mn^{3+} redox couple on charging and discharging. In addition, the possibility that the increased discharge capacity in early cycles may result from an impurity phase in the material will need to be addressed in future works.

Finally, the reason why the inclusion of iron in $Li_3Fe_{0.2}Mn_{0.8}CO_3PO_4$ significantly improves the material is not yet known.

2.1.5 Conclusions from $Li_3Fe_{0.2}Mn_{0.8}CO_3PO_4$ electrochemical analysis

In this section of work an improvement over the performance of $Li_3MnCO_3PO_4$ by doping the compound with iron is reported. The synthesis of $Li_3Fe_{0.2}Mn_{0.8}CO_3PO_4$ is demonstrated via hydrothermal synthesis of a sodium-containing precursor followed by a Na–Li ion-exchange reaction. The Fe doping allows to ion exchange to proceed to near (>99%) completion. $Li_3Fe_{0.2}Mn_{0.8}CO_3PO_4$ cathodes show a reversible capacity around 105 mAh/g with excellent cyclability over 25 cycles. The observed initial drop in capacity comes from irreversible cycling of impurities formed during synthesis. Three redox couples, Mn^{2+}/Mn^{3+}, Mn^{3+}/Mn^{4+}, and Fe^{2+}/Fe^{3+} are active in this material. The results open new opportunities to improve the performance of the novel carbonophosphate cathode materials by doping and structural tuning. This is particularly meaningful because as recently reported, besides Fe and Mn, many alkaline earth and transition metals can also form Li-containing carbonophosphate in pure or doped form [165].

2.2 Examination of thermal stability in lithium-containing carbonophosphates

2.2.1 Introduction

Examination of $Li_3Fe_{0.2}Mn_{0.8}CO_3PO_4$ shows that all Fe and Mn redox couples are active in this material during electrochemical cycling, and that its first cycle capacity exceeds its theoretical single-electron capacity. From these results, $Li_3Fe_{0.2}Mn_{0.8}CO_3PO_4$ seems to be a promising candidate cathode that could be significantly improved through further optimization. In addition, the material has proven of interest to the Li-ion battery community [166, 167] and at least one additional university group has continued research efforts on the lithium-containing carbonophosphates [168].

However, continued testing revealed that older $Li_3Fe_{0.2}Mn_{0.8}CO_3PO_4$ samples performed significantly worse than newer ones when tested as cathodes, and attempts at elevated temperature (55^{o}C) cycling were unsuccessful due to a 100% failure rate of cells using a $Li_3Fe_{0.2}Mn_{0.8}CO_3PO_4$ cathode. Together, these problems led to concerns about the thermodynamic and, therefore, thermal stability of $Li_3Fe_{0.2}Mn_{0.8}CO_3PO_4$. When this composition was originally calculated by Hautier et al., the Li-containing carbonophosphates were all predicted to be metastable [6]. Figure 2-4 is an excerpt of a figure from the paper by Hautier et al. in which Li-containing carbonophosphates were first predicted. Figure 2-4 shows the calculated stability of the Na- and Li-containing carbonophosphates by plotting the energy above the hull, or the thermodynamic driving force of decomposition, for the calculated material to its ground state, for different transition metals in the carbonophosphate structure. Many of the Na-containing carbonophosphates are a thermodynamic ground state structure, but none of the Li-containing carbonophosphates represent the thermodynamic ground

state at its composition. From this figure, $Li_3Fe_{0.2}Mn_{0.8}CO_3PO_4$ is approximately 50 meV per atom off of the energy hull. The issues of decreasing performance with older samples and high failure rate of cells at elevated temperatures were hypothesized to be the result of $Li_3Fe_{0.2}Mn_{0.8}CO_3PO_4$ decomposition to its thermodynamic ground state. To determine if the calculated metastability of $Li_3Fe_{0.2}Mn_{0.8}CO_3PO_4$ was indeed causing material decomposition and the observed problems, thermal stability tests were conducted.

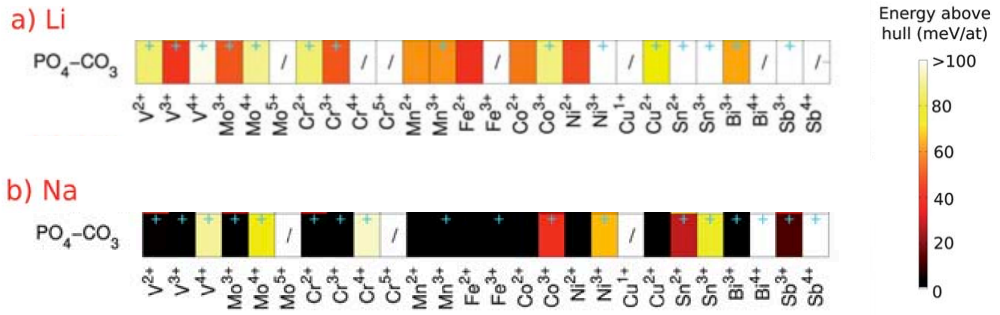

Figure 2-4: An excerpt from Figure 2 in the work by Hautier et al. published in 2011. The figure depicts the calculated energy of decomposition to thermodynamic ground states for $A_xM(CO_3)(PO_4)$ compositions in the sidorenkite structure (with M being a redox active metal) for (a) lithium-based (A = Li) compounds and (b) sodium-based (A = Na) compounds. The color indicates the decomposition energy. Light colors indicate thermodynamic instability while darker colors indicate greater thermodynamic stability. A black "/" indicates a missing entry in the Ceder Group database (i.e., chemistries that could not be charge balanced or computations that did not converge) [6].

2.2.2 Experimental methods

The sample of $Li_3Fe_{0.2}Mn_{0.8}CO_3PO_4$ used in this thermal decomposition study was synthesized using the same two-step hydrothermal synthesis and ion-exchange method described in Section 2.1.2. XRD spectra were measured both for the pristine $Li_3Fe_{0.2}Mn_{0.8}CO_3PO_4$ sample and the end result using a Rigaku Miniflex II diffractometer (chromium Kα, $\lambda = 2.2897$, Rigaku corporation, Tokyo) in flat-plate mode, scanning from 10^o to 120^o two-theta.

Short- and long-term thermal stability tests were conducted on $Li_3Fe_{0.2}Mn_{0.8}CO_3PO_4$ at 55^oC, the temperature at which elevated-temperature cycling tests with this material failed. The short-term Thermogravimetric Analysis (TGA) testing was conducted using a Simultaneous Differential Scanning Calorimeter and Thermogravimetric Analyzer (SDT) manufactured by TA Instruments (New Castle, Delaware). The sample was held at 55^oC for 10 hours under flow of Argon while its weight was continuously monitored. For the long term thermal stability test, approximately one gram of pristine $Li_3Fe_{0.2}Mn_{0.8}CO_3PO_4$ was placed in an empty CR2016 coin cell and sealed while in an Ar-filled glove box. The filled and sealed coin cell was then placed in a 55^oC thermoelectric temperature oven (TestEquity LLC, Moorpark, California) for 6 months, after which the contents was removed and analyzed using XRD.

2.2.3 Experimental results

The results of isothermal TGA analysis of $Li_3Fe_{0.2}Mn_{0.8}CO_3PO_4$ are shown in Figure 2-5, which shows a plot of sample weight percent as a function of time held at 55^oC. The sample weight drops more quickly for approximately the first two hours, and then decreases more slowly by the end of the test. The initial high rate of weight

loss is likely the result of evaporation of water on the surface of the sample pan and sample. In similar TGA tests, water evaporation commonly accounts for 1-2% sample weight loss, which is consistent with this test. After ten hours, the rate of weight loss over time appears close to a steady state value of -0.03% per hour. This test implies that the $Li_3Fe_{0.2}Mn_{0.8}CO_3PO_4$ sample decomposes slowly at 55°C, but the test duration is too short and the decomposition rate too slow for a conclusive result for or against carbonophosphate decomposition in this case.

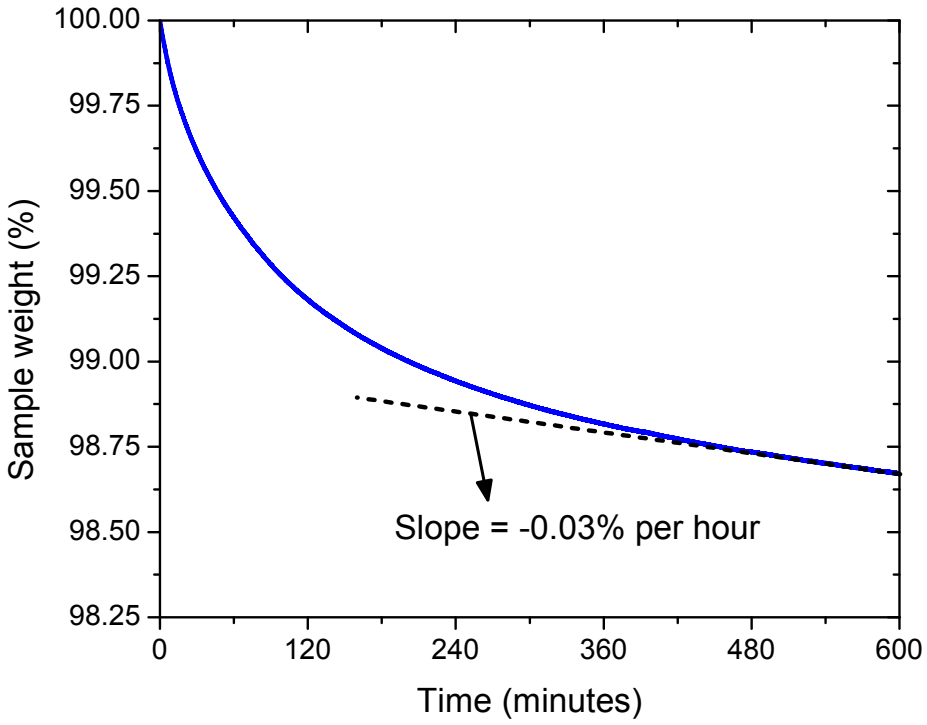

Figure 2-5: Sample weight percent graphed versus time for a sample of $Li_3Fe_{0.2}Mn_{0.8}CO_3PO_4$ held at 55°C. Additionally, the steady-state slope is estimated using the line shown.

XRD spectra for the $Li_3Fe_{0.2}Mn_{0.8}CO_3PO_4$ used in the long-term thermal stability test is shown in Figure 2-6. After six months in a 55^{o}C isothermal oven, the sample's XRD spectrum is significantly different than the original $Li_3Fe_{0.2}Mn_{0.8}CO_3PO_4$ sample, and none of the original sample crystal structure is present. The specific crystalline phase composition of the residual sample was not readily identifiable, and the broad elevated background signal indicates that a significant portion of the sample had become amorphous. Despite the difficulty in identifying exact composition, it is clear the $Li_3Fe_{0.2}Mn_{0.8}CO_3PO_4$ had fully decomposed.

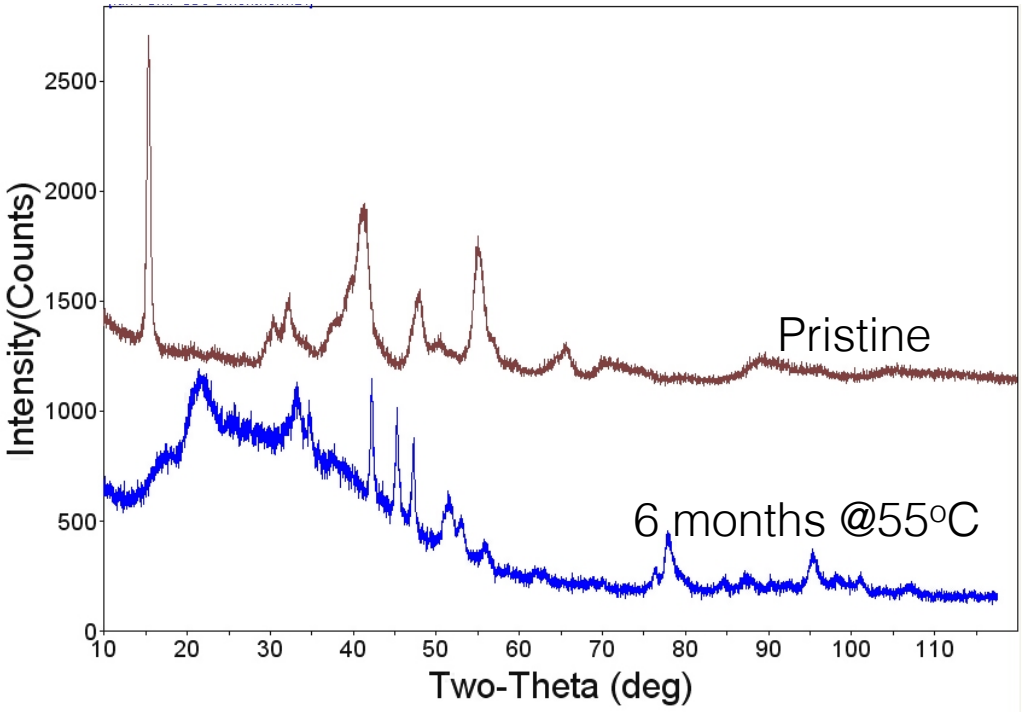

Figure 2-6: XRD spectra for an as-synthesized sample of $Li_3Fe_{0.2}Mn_{0.8}CO_3PO_4$ and an identical sample that had been placed in a 55^{o}C oven for 6 months.

2.2.4 Discussion and conclusions of carbonophosphate thermal stability

From the short- and long-term thermal stability tests performed on $Li_3Fe_{0.2}Mn_{0.8}CO_3PO_4$, it is clear that the material decomposes at 55^oC. Given that the material is close to 50 meV per atom above the energy hull, it is not surprising that $Li_3Fe_{0.2}Mn_{0.8}CO_3PO_4$ will decompose at elevated temperatures. Further, $Li_3Fe_{0.2}Mn_{0.8}CO_3PO_4$ becomes less stable as its lithium content decreases, which would exacerbate decomposition-related cycling issues, explaining the consistent cell failure for elevated temperature cycling tests of $Li_3Fe_{0.2}Mn_{0.8}CO_3PO_4$. As 55^oC is not a high temperature for a battery to be exposed to during standard operation, making use of $Li_3Fe_{0.2}Mn_{0.8}CO_3PO_4$, or any Mn-containing carbonophosphate, as a Li-ion battery cathode would not be possible. Therefore, despite promising cycling characteristics and the potential for multi-redox cycling performance, research on this class of materials was abandoned.

Chapter 3

Fluorophosphate cathodes for Na-ion batteries

3.1 Introduction

As discussed in earlier chapters, the need for increased energy storage coupled with concerns about the cost and availability of metals used in Li-ion battery cathodes has fueled a resurgence in the study of Na-ion batteries [169, 32, 62, 31]. To date, layered oxide Na-ion battery cathodes have demonstrated the best capacities and energy densities and, as a result, have received the majority of research attention. Despite this, oxide cathodes face significant problems including Na-ion ordering, dramatically stepped voltage plateaus, phase transformations during cycling, and poor cyclability [100, 45, 98, 44].

Polyanionic Na-ion cathodes are a promising alternative to oxide cathodes, as they constitute a wider design-space and offer more compositional flexibility when designing new materials with high redox potential. Among the polyanionic Na-ion

battery cathodes examined, fluorophosphates are currently the highest performing. Fluorophosphates have been shown experimentally to exhibit energy densities comparable to many oxide cathodes, but with higher cycle life [49, 50]. $Na_3V_2(PO_4)_2F_3$ is one of the most studied material of this class, and it has been demonstrated to reversibly cycle near its one-electron theoretical capacity of 128 mAh/g at an average voltage of ∼3.75V, while cycling between compositions of $Na_3V_2(PO_4)_2F_3$ and $NaV_2(PO_4)_2F_3$ [49]. While this is high performance for a polyanionic Na-ion cathode, an energy density of ∼470 Wh/kg would not be enough to supplant Li-ion battery cathodes, or even Na-ion battery oxide cathodes. Consequently, Kang [170, 49], Rojo [51], Goodenough [171], and others have tried to improve upon the performance of these cathodes through oxygen substitution, making cathodes with the chemical formula $Na_3V_2O_{2x}(PO_4)_2F_{3-2x}$. Substituting oxygen for fluorine increases the starting valence state of vanadium, which had the potential to increase the performance of oxyfluorophosphate cathodes over fluorophosphate cathodes by raising their average voltage. Together, in fluorophosphate and oxyfluorophosphate cathodes, both the V^{3+}/V^{4+} and V^{4+}/V^{5+} redox couples have been accessed reversibly and contributed significantly to capacity. However, no modified fluorophosphate cathodes have significantly exceeded the one-electron capacity (∼130mAh/g) so far [49, 170, 51, 171], and, as such, these materials do not improve on the performance of $Na_3V_2(PO_4)_2F_3$.

To make fluorophosphate cathodes competitive with Li-ion battery technology, their capacity must be substantially improved. If they can be made to cycle through an expanded composition range, the potential exists to achieve a capacity of 192 mAh/g if all sodium can be extracted, yielding a cathode composition of $V_2(PO_4)_2F_3$. If sodium can also be inserted to fill all available sites in the fluorophosphate crystal structure, making $Na_4V_2(PO_4)_2F_3$, a capacity as high as 256 mAh/g could be possible. This chapter investigates if it is possible to cycle fluorophosphate cathodes for

Na-ion batteries in an expanded Na concentration range by electrochemically inserting Na^+ in $Na_3V_2(PO_4)_2F_3$. In addition, cathodes of mixed transition metal compositions are examined, and performance-limiting mechanisms in fluorophosphate Na-ion battery cathodes are determined.

3.2 Electrochemical insertion of Na^+ in $Na_3V_2(PO_4)_2F_3$

3.2.1 Motivation for seeking Na^+ insertion

To determine if fluorophosphate cathodes could reversibly access greater than one electron per transition metal ion per electrochemical cycle and extend capacity beyond 128mAh/g, the possibility of electrochemical insertion of Na^+ in $Na_3V_2(PO_4)_2F_3$ is investigated. Two observations from literature indicate that electrochemical insertion of Na^+ could be possible. First, only three fourths of the possible Na^+ sites in $Na_3V_2(PO_4)_2F_3$ are occupied when the material is synthesized. Shakoor et al. define three Na^+ sites in the NASICON-like structure of $Na_3V_2(PO_4)_2F_3$, which they call Na1, Na2, and Na3 [49]. Na3 is a transition state unoccupied in the ground state crystal structure. Na1 is the lowest energy Na site and is fully occupied while the slightly higher energy site, Na2, is half-occupied in the as-synthesized material described in that work [49, 172]. If all Na1 and Na2 sites were occupied, the crystal composition would become $Na_4V_2(PO_4)_2F_3$. (Note: It would be impossible for Na3 sites to be occupied in addition to this due to high electrostatic forces between ions in sites adjacent to the Na3 site, meaning that $Na_4V_2(PO_4)_2F_3$ constitutes the highest Na concentration chemistry in this structure.) The second observation comes from Chihara et al.'s 2013 publication on fluorophosphate cathodes [50]. In Figure 4b of that work, $Na_3V_2(PO_4)_2F_3$ is discharged to 1.0 V, and the voltage versus capacity

plot shows a plateau near the low-voltage cutoff, which could indicate electrochemical Na^+ insertion. However, neither data showing charging from this low cutoff nor any other characterization of this plateau is presented in that work, so the reason for this plateau remained unknown. Based on these observations, $Na_3V_2(PO_4)_2F_3$ was synthesized and characterized in order to determine if Na^+ can be electrochemically inserted into this structure reversibly.

3.2.2 Experimental methods

Synthesis methods

$Na_3V_2(PO_4)_2F_3$ was synthesized via a two-step solid-state synthesis method similar to that used by Shakoor et al. [49]. First, stoichiometric amounts of V_2O_5 (Alfa Aesar, 99.2%) and $NH_4H_2PO_4$ (Sigma Aldrich, 99.999%) were mixed with 15% carbon black (Super P) by mass. The mixture was pelletized and heated to 750^{o}C for 4 hours under flow of argon. The resultant mixtures was then crushed, mixed with a stoichiometric amount of NaF (Alfa Aesar, 99.0%), repelletized, and calcined at 750^{o}C for 2 hours under flow of argon.

Sample characterization methods

Powder XRD was used to identify the phases present in the as-synthesized sample. XRD measurements for phase identification were taken using a Rigaku Miniflex II diffractometer (chromium Kα, $\lambda = 2.2897$ Å, Rigaku corporation, Tokyo) in flat-plate mode, scanning from 15^o to 65^o two-theta.

Electrochemical characterization methods

Prior to electrochemical characterization of the fluorophosphate samples, they were ball-milled with carbon in zirconia-lined milling jars in a Retsch PM200 planetary ball mill to improve the material's electrochemical performance through decreased particle size and carbon coating [161, 160]. The milled active material and carbon mixture consisted of an 80:20 mass ratio of fluorophosphate active material to carbon (Super P), and were milled for 4 hours at 400rpm. The resultant powder was removed from the milling jars in an Ar-filled glove box to limit air exposure.

For electrochemical characterization, composite electrode films were made using a dry-rolling method. PTFE binder was added to each ball-milled active material/carbon mixture such that the final ratio of components in the prepared electrodes was 76:19:5 by mass, respectively. The mixture was manually rolled on a steel plate to produce electrode films. Each electrode contained $\sim$2 mg of active material. Battery cells were assembled using Swagelok cells with 316 stainless steel current collectors, the dry-rolled cathode films described, glass fiber separator films, a solution of 1 M $NaPF_6$ in ethylene carbonate/diethyl carbonate (1:1) as electrolyte, and a Na metal anode. Galvanostatic experiments were conducted at a rate of C/20 on an Arbin Instruments (College Station, TX) battery cycler.

In situ x-ray diffraction methods

In situ XRD measurements were conducted on $Na_3V_2(PO_4)_2F_3$ cathodes such that crystal structure changes could be observed as sodium concentration changed during electrochemical cycling. These measurements were conducted on the Ceder Group's laboratory *in situ* XRD set-up using a Bruker D8 Advance diffractometer (molybdenum Kα, λ = 0.7093 Å), Bruker AXS, Germany). A specially-designed battery

cell, shown schematically in Figure 1-8, was assembled with a $Na_3V_2(PO_4)_2F_3$ composite cathode film prepared identically to that described in the previous paragraph, but containing ∼15 mg of active material and having a larger radius, a Celgard 2025 separator (Celgard Inc., U.S.A.), a Na metal anode, and aluminum foil current collectors in an Ar-filled glove box, and loaded onto the diffractometer's sample stage. The battery was then cycled galvanostatically at a rate of C/20 using a single-channel Solartron SI 1287 potentiostat (Solartron Analytical, Kingston-on-Thames, UK). Simultaneously, The Bruker D8 diffractometer collected spectra from 7^o to 40^o two-theta. XRD measurements were completed continuously on the cycling $Na_3V_2(PO_4)_2F_3$ cell. Each spectrum measurement spanned one hour and was mapped to the electrochemical test time and, thus, cell voltage and sodium content.

3.2.3 Experimental results

Synthesis results

The synthesis method in Section 3.2.2 resulted in a two-phase system consisting of the desired $Na_3V_2(PO_4)_2F_3$ phase with a $P4_2/mnm$ space group (Inorganic Crystal Structure Database powder diffraction file ID 03-012-2207) and an impurity phase of $Na_3V_2(PO_4)_3$ with the R-3c (NASICON) space group (Inorganic Crystal Structure Database powder diffraction file ID 00-062-0345). While the $Na_3V_2(PO_4)_2F_3$ sample is not a single phase, it is of sufficient purity for the purposes of this study. The XRD spectrum for $Na_3V_2(PO_4)_2F_3$ is shown in Figure 3-1.

Electrochemical results

The electrochemical cycling performance of $Na_3V_2(PO_4)_2F_3$ collected under galvanostatic conditions at a rate of C/20 is shown in Figure 3-2. The cathode had a charge

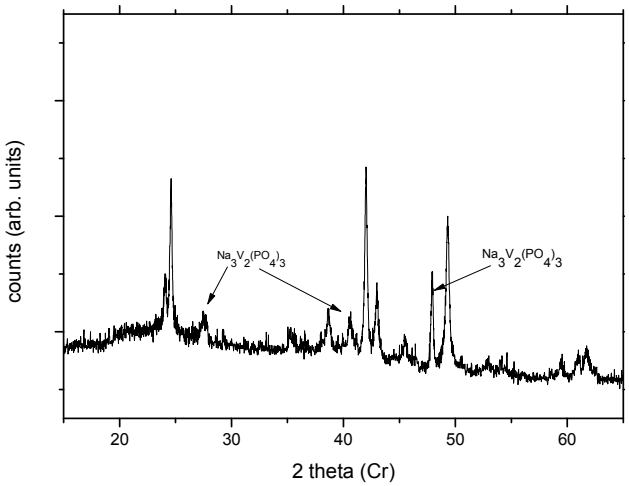

Figure 3-1: XRD spectrum for the synthesized sample of $Na_3V_2(PO_4)_2F_3$ used for electrochemical characterization. Impurity peaks are labelled on the figure.

capacity of 132 mAh/g and a discharge capacity of 129 mAh/g, including the two expected plateaus at 3.6 V and 4.2 V, corresponding to activity in the V^{3+}/V^{4+} redox couple, which is well documented in the literature [49, 50]. In addition, a third plateau is present at 1.5 V on charge and 1.2 V on discharge, indicating reversible activity of the V^{2+}/V^{3+} redox couple, which had not been previously presented in the literature prior to this study. Small plateaus at 3.3 V and 1.7 V are also observed. This can be attributed to electrochemical activity of $Na_3V_2(PO_4)_3$, an impurity present in the cathode sample, as previously noted. The observed performance is roughly 80% of that observed in the literature for the voltage window from 2.0 V to 4.5 V for an optimized $Na_3V_2(PO_4)_2F_3$ cathode [49, 50], but this performance is sufficient for the current investigation.

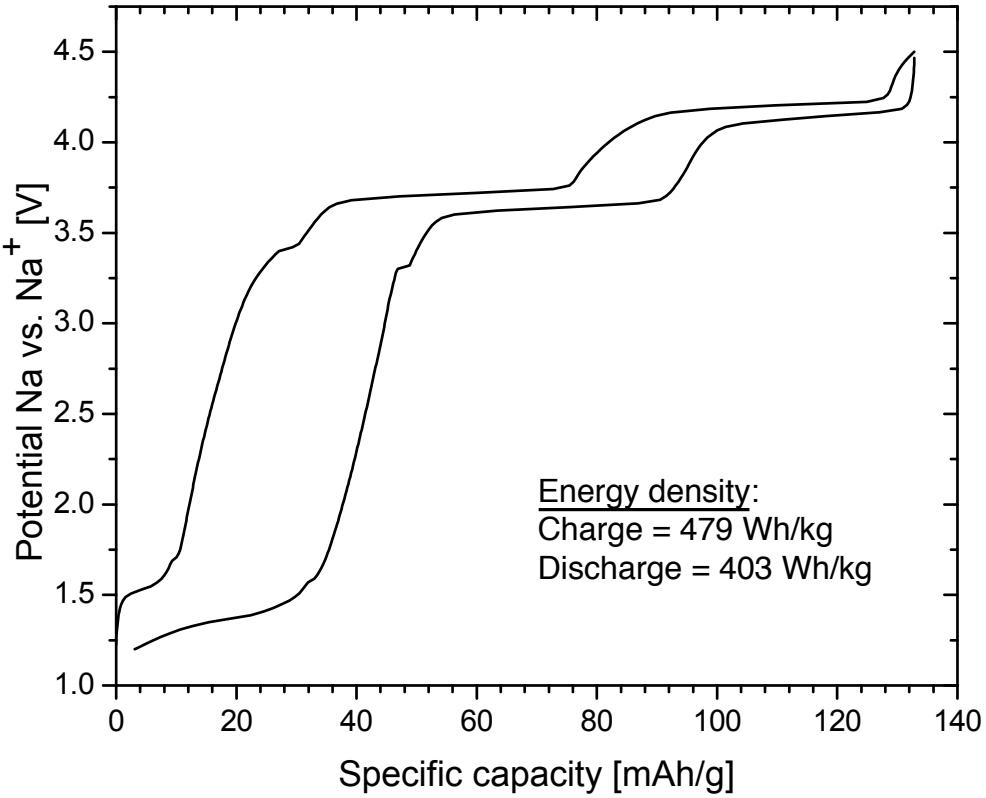

Figure 3-2: A voltage versus capacity plot for the electrochemical cycling of $Na_3V_2(PO_4)_2F_3$ during its third cycle of galvanostatic cycling at a rate of C/20. Notably, a low voltage plateau exists near 1.2 V on both charge and discharge, which could indicate reversible Na^+ insertion.

In situ x-ray diffraction results

In situ XRD experiements were performed on $Na_3V_2(PO_4)_2F_3$ as a means to determine the reaction mechanism responsible for the reversible low-voltage capacity in $Na_3V_2(PO_4)_2F_3$ during galvanostatic cycling. Specifically, these experiments were conducted to determine if the 1.2 V plateau is the result of a conversion or topotactic intercalation reaction. Sequentially-collected XRD spectra and corresponding electrochemical results of this experiment are presented in Figure 3-3, which is presented such that the start of each XRD spectrum can be horizontally tracked to the time and voltage (and thus sodium content) at which the spectrum was measured. The data focuses on spectra taken at voltages equal to or below the cell's open circuit voltage. As such, it can be concluded that the cathode is measured when it has a greater sodium content than its as-synthesized state. In the spectra presented, no significant peak shifts, new peaks, or changes in relative peak intensity are observable within the resolution of the measurement.

3.2.4 Discussion and conclusions

Given the reversible low-voltage activity in $Na_3V_2(PO_4)_2F_3$ cathodes and *in situ* XRD measurements, it can be concluded that it is possible to reversibly access the V^{2+}/V^{3+} redox couple in $Na_3V_2(PO_4)_2F_3$ and that this activity comes from Na^+ insertion rather than conversion. From Figure 3-3, it is clear that no substantial change occurs during low voltage cycling. In the case of electrochemical conversion, in which $Na_3V_2(PO_4)_2F_3$ would be converted into a metal and a phosphate salt, one would expect a binary metal-fluoride phase, likely NaF or another strong x-ray scatterer, to appear and the $Na_3V_2(PO_4)_2F_3$-related peaks to significantly diminish in intensity, particularly in the low-voltage potentiostatic regime, but neither of these

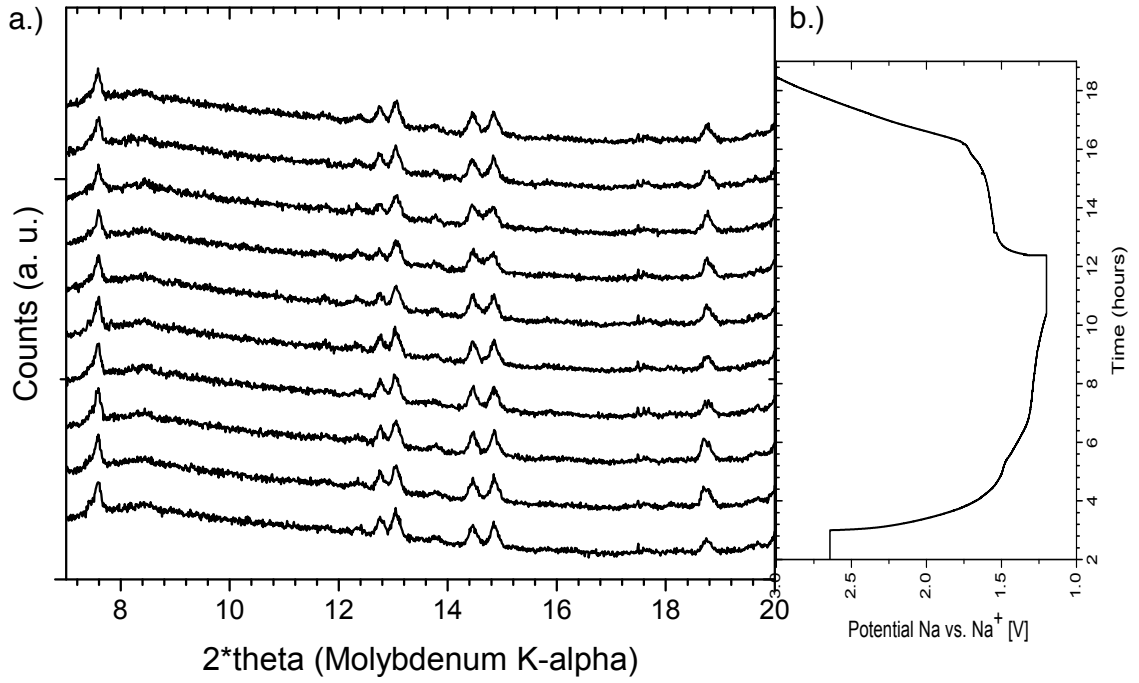

Figure 3-3: Combined *in situ* XRD and electrochemical data for a cycling $Na_3V_2(PO_4)_2F_3$ cathode. (a)Sequential XRD scans collected collected for $Na_3V_2(PO_4)_2F_3$ at differing cell voltages/sodiations and (b) a voltage versus time plot for the same cell. The two graphs are aligned such that following the first point of the XRD scan horizontally places the scan at its corresponding voltage and time.

changes occurs. The lack of peak shift resulting from lattice parameter changes is also consistent with electrochemical insertion of Na^+ into the $Na_3V_2(PO_4)_2F_3$ crystal structure. The NASICON-like crystal structure of fluorophosphate cathodes is known to exhibit low strain during cycling, and $Na_3V_2(PO_4)_2F_3$ exhibits less than 2% volumetric strain when two sodium ions per formula unit are extraced, so it is expected that Na^+ insertion would cause very little change in the crystal structure lattice parameter [49]. As such, any changes in lattice parameter, and the associated peak shifts in XRD spectra, could reasonably be expected to be small enough that they would be unobservable in a measurement with the resolution of the performed experiment.

Since electrochemical insertion of Na^+ occurs rather than cathode conversion at low voltages, it is possible that the observed low voltage capacity may be used in conjunction with previously-observed topotactic Na^+ extraction to increase capacity over the current capacity of fluorophosphate cathodes. However, the observed capacity is low enough that it would neither significantly contribute to cathode energy density nor be easily accessed in a commercial cell also using the capacity available above 3 V. In order for the 2+/3+ redox to be significantly improve the performance of fluorophosphate cathodes, the voltage at which the redox couple is accessed must increase. In an effort to accomplish this, different mixed-transition metal fluorophosphate chemistries were examined and are presented in Section 3.3.

3.3 $Na_3[M]_2(PO_4)_2F_3$ with {M = Fe, Ti, V} as a promising template for Na-ion battery cathodes

3.3.1 Fluorophosphates as a multi-redox Na-ion cathode template

In the electrochemical and *in situ* XRD study of $Na_3V_2(PO_4)_2F_3$ in Section 3.2, it was shown that V^{2+}, V^{3+}, and V^{4+} are accessible during a single charge or discharge. Even though the V^{2+}/V^{3+} activity occurs at too low of a voltage to significantly improve cathode energy density, fluorophosphate cathodes with the promising template chemistry $Na_3[M]_2(PO_4)_2F_3$ can be strategically designed as cathodes for Na-ion batteries. For single and mixed-TM cathodes of this type with carefully chosen chemistries, the average voltage of 2+/3+ redox might be made higher than that of V^{2+}/V^{3+} alone, meaning the insertion regime of electrochemical cycling could contribute more significantly to cathode performance. If Na^+ can be inserted to full Na-site occupancy, making a cathode chemistry of $Na_4[M]_2(PO_4)_2F_3$, and then extracted to $Na[M]_2(PO_4)_2F_3$ in a single half-cycle, one and a half electrons per transition metal ion would be accessed, resulting in a capacity of approximately 185mAh/g, depending on the specific cathode transition metal chemistry. Mixed-transition metal chemistries employing mixed activity of 2+/3+, 3+/4+, and 4+/5+ redox couples could also be employed to achieve this high capacity. This design strategy is schematically represented in Figure 3-4. If all redox couples may be accessed with an average voltage of 3.24 V, the energy density of the cathode would be 600 Wh/kg, placing such a cathode among the best-performing Na-ion oxide cathodes and $LiFePO_4$ cathodes for Li-ion batteries.

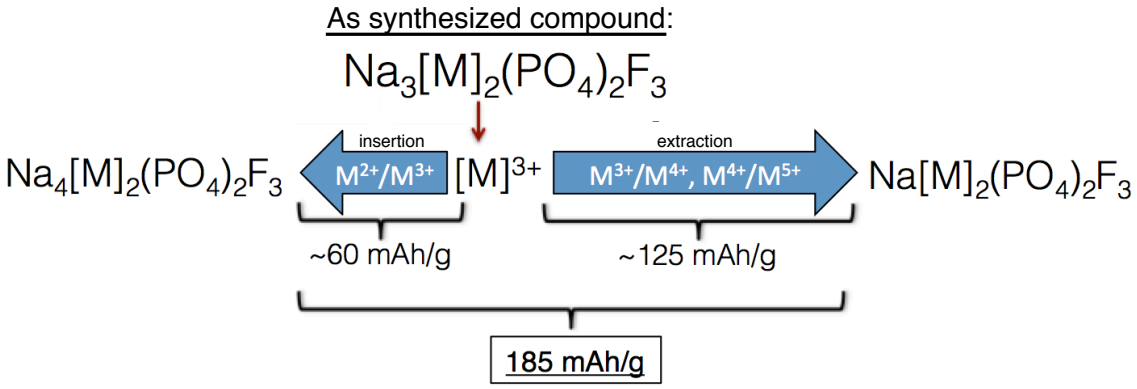

Figure 3-4: A schematic diagram explaining the specific redox activity expected, and the capacity each redox couple would contribute in the insertion and extraction regimes for cathodes of the type $Na_3[M]_2(PO_4)_2F_3$ with {M = Fe, Ti, V}.

For this study, $Na_3[M]_2(PO_4)_2F_3$, where {M = Fe, Ti, V}, is examined. Fe and Ti were chosen in addition to V since they are known to be stable in a 3+ valence state, have been shown to be redox active in Na-ion batteries, and have a similar ionic radius to V^{3+}, which combined imply that these fluorophosphate chemistries should be synthesizeable and redox active. In addition, $Na_3Ti_2(PO_4)_2F_3$ and $Na_3Fe_2(PO_4)_2F_3$ have both been previously synthesized and examined as Na-ion cathodes by Chihara et al., though not for insertion capacity [50]. In this case, the novel mixed-transition metal chemistries, $Na_3TiV(PO_4)_2F_3$ and $Na_3FeV(PO_4)_2F_3$, are of primary interest. Synthesis and electrochemical characterization for $Na_3Ti_2(PO_4)_2F_3$, $Na_3TiV(PO_4)_2F_3$, $Na_3Fe_2(PO_4)_2F_3$, and $Na_3FeV(PO_4)_2F_3$ are reported in this section.

3.3.2 Experimental Methods

Synthesis methods

All $Na_3[M]_2(PO_4)_2F_3$, where {M = Fe, Ti, V} compositions examined in this study, with the exception of $Na_3Fe_2(PO_4)_2F_3$, were made using a two-step solid-state synthesis method similar to those presented in the literature for fluorophosphate cathode compounds [49, 50]. The $Na_3V_2(PO_4)_2F_3$ sample used as a baseline for new compositions was prepared using the same synthesis method as in Section 3.1. Restated, $Na_3V_2(PO_4)_2F_3$ was made by first combining stoichiometric amounts of V_2O_5 (Alfa Aesar, 99.2%) and $NH_4H_2PO_4$ (Sigma Aldrich, 99.999%) with 15% carbon black (Super P) by mass and heating the mixture to 750^{o}C for 4 hours under flow of argon. The resulting pellets of VPO_4 and carbon was mixed with a stoichiometric amount of NaF (Alfa Aesar, 99.0%), pressed into a new pellet, and put in a 750^{o}C furnace for 2 hours under flow of argon.

Titanium-containing fluorophosphate compounds were made using Ti_2O_3 (Sigma Aldrich, 99.9%). For both $Na_3Ti_2(PO_4)_2F_3$ and $Na_3TiV(PO_4)_2F_3$, a stoichiometric amount of Ti_2O_3 was mixed with $NH_4H_2PO_4$ (Sigma Aldrich, 99.999%), and, in the case of $Na_3TiV(PO_4)_2F_3$, V_2O_5 (Alfa Aesar, 99.2%), and calcined at 700^{o}C for 15 hours under flow of 5% hydrogen in 95% argon. Then each sample was crushed, mixed with a stoichiometric amount of NaF (Alfa Aesar, 99.0%), repelletized, and and fired at 600^{o}C for 2 hours under flow of argon.

$Na_3FeV(PO_4)_2F_3$ synthesis required a first step of mixing V_2O_5 (Alfa Aesar, 99.2%) and $NH_4H_2PO_4$ (Sigma Aldrich, 99.999%) with 15% carbon black (Super P) by mass and firing the mixture at 750^{o}C for 4 hours under flow of argon. The synthesized VPO_4 was then mixed with stoichiometric amounts of $FePO_4 \cdot 2H_2O$ (Sigma Aldrich, Fe 29%) and NaF (Alfa Aesar, 99.0%) and calcined at 600^{o}C in

argon for 2 hours.

$Na_3Fe_2(PO_4)_2F_3$ was made using a single-step solid state synthesis method by mixing $FePO_4 \cdot 2H_2O$ (Sigma Aldrich, Fe 29%, 5% molar excess) with NaF (Alfa Aesar, 99.0%), pelletizing the mixture, and firing it at 600^oC in argon for 2 hours.

Characterization methods

Synthesis products were identified using powder XRD. XRD spectra were collected using a Rigaku Miniflex II diffractometer (chromium Kα, $\lambda = 2.2897$ Å, Rigaku corporation, Tokyo) in flat-plate mode. HighScore Plus software (PANalytical, Netherlands) was used for phase identification.

To decrease particle size and carbon coat the synthesized cathode materials, the synthesis products were ball-milled with carbon in zirconia-lined millling jars in a Retsch PM200 planetary ball mill for 4 hours at 400 rpm. The milled active material and carbon mixture consisted of an 80:20 mass ratio of active material to Carbon (Super P), and carbon was added to each sample as necessary to meet this ratio. The samples were loaded into the milling jars and unloaded in an argon-filled glove box.

For electrochemical characterization, the synthesized fluorophosphates were made into composite cathode films using a dry-rolling method. PTFE binder, at 5% by mass, was added to each ball-milled active material mixture, and the mixtures were rolled into cathode films on a steel plate. The final ratio of components (active material:carbon:binder) in the prepared electrodes was 76:19:5 by mass. Battery cells were made using Swagelok cells with 316 stainless steel current collectors, a $\sim$2mg dry-rolled cathode film prepared as described above, a glass fiber separator film, a solution of 1 M $NaPF_6$ in ethylene carbonate/diethyl carbonate (1:1) as electrolyte,

and a Na metal anode. An Arbin Instruments (College Station, TX) battery cycler was used to perform galvanostatic cycling tests at a rate of C/20 for each cathode composition presented.

3.3.3 Experimental Results

Synthesis Results

The XRD spectra for as-synthesized samples of $Na_3Ti_2(PO_4)_2F_3$ and $Na_3TiV(PO_4)_2F_3$ are presented in Figure 3-5. Each sample exhibited a tetragonal crystal structure with the $P4_2/mnm$ space group, which is characteristic of the $Na_3V_2(PO_4)_2F_3$ "template" structure. In Figure 3-5, the XRD spectrum of $Na_3V_2(PO_4)_2F_3$ is included as a reference, with vertical lines overlaid to indicate its major peak positions. The peak positions in Ti-containing samples exhibit a small peak shift towards smaller angles, which is expected given that the ionic radius of Ti^{3+} (81 pm) is larger than that of V^{3+} (78 pm). For $Na_3TiV(PO_4)_2F_3$, XRD peak shifts are approximately half as large as those of $Na_3Ti_2(PO_4)_2F_3$. Additionally, the $Na_3TiV(PO_4)_2F_3$ sample's XRD spectrum consists of well-defined, sharp peaks. Combined, these two facts indicate that the $Na_3TiV(PO_4)_2F_3$ sample is a single phase with Ti and V in a well-mixed solid solution in the crystal structure, rather than separate Ti- and V-containing phases and/or domains. If that were the case, one would expect to see doublet peaks at the major peak positions or broad peaks in the XRD pattern for the mixed-transition metal sample, neither of which is the case.

XRD spectra of $Na_3Fe_2(PO_4)_2F_3$ and $Na_3FeV(PO_4)_2F_3$ samples are shown in Figure 3-6. Unlike Ti-containing samples, the Fe-containing samples could not be synthesized as a single phase, nor could the impurity phase(s) be readily identified. Impurity peaks are labeled in Figure 3-6. The major phase in the samples, however,

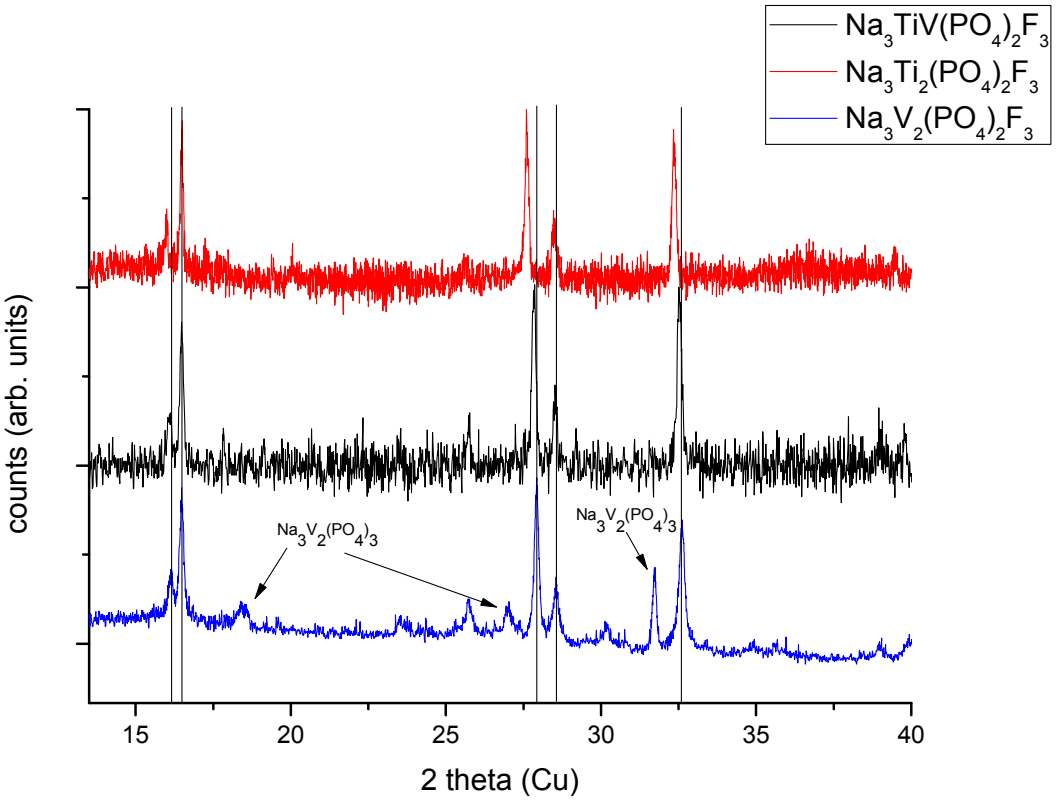

Figure 3-5: Collected XRD spectra for as-synthesized $Na_3V_2(PO_4)_2F_3$, $Na_3Ti_2(PO_4)_2F_3$, and $Na_3TiV(PO_4)_2F_3$. Impurity peaks are labelled in the spectra and vertical lines have been inserted to demonstrate the alignment of major peaks in $Na_3V_2(PO_4)_2F_3$ with those in the other synthesized samples.

was the fluorophosphate tetragonal structure in the $P4_2/mnm$ space group. Like the combined spectra presented for $Na_3Ti_2(PO_4)_2F_3$ and $Na_3TiV(PO_4)_2F_3$ in Figure 3-5, vertical lines are overlaid on the aligned spectra to indicate major peak positions of $Na_3V_2(PO_4)_2F_3$ so that they may be readily compared with the synthesized samples.

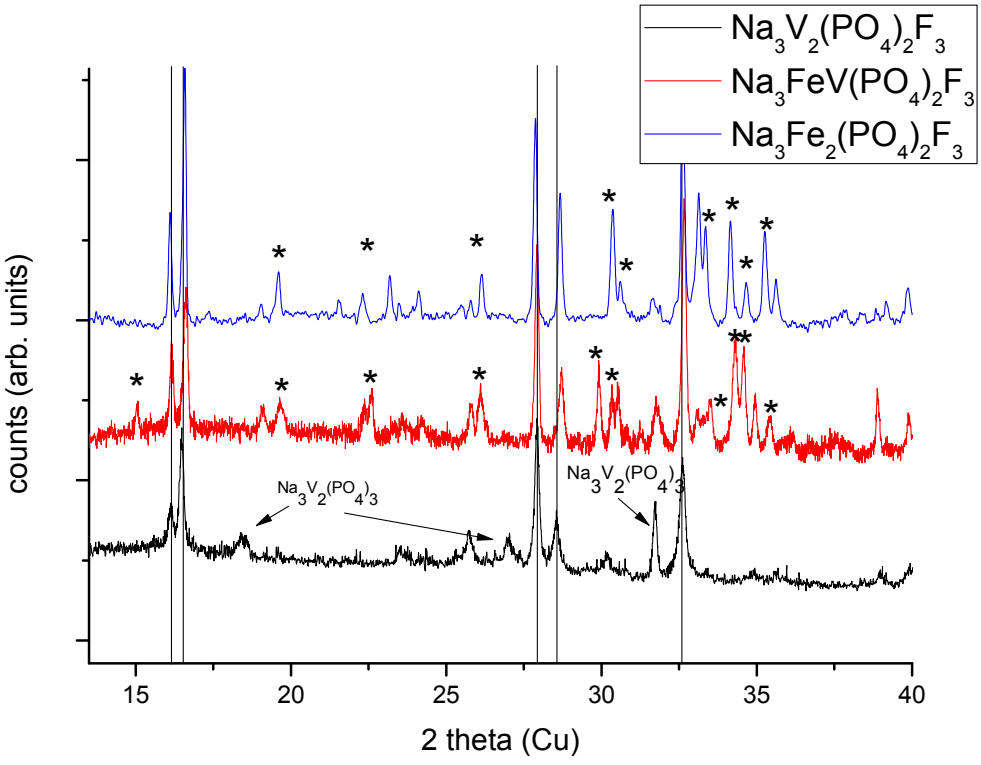

Figure 3-6: Collected x-ray diffraction spectra for as-synthesized $Na_3V_2(PO_4)_2F_3$, $Na_3Fe_2(PO_4)_2F_3$, and $Na_3FeV(PO_4)_2F_3$. Impurity peaks are labelled in the spectra and vertical lines have been inserted to demonstrate the alignment of the major peaks in $Na_3V_2(PO_4)_2F_3$ with those in the other synthesized samples.

Electrochemical results

For electrochemical testing of $Na_3[M]_2(PO_4)_2F_3$ cathodes, a smaller electrochemical testing window was used than in Sections 3.1. As the goal of these materials is to increase the energy density of the cathodes, only capacity above 1.5 V was viewed as significant. As such, all presented electrochemical data in this section is shown for galvanostatic cycling at a rate of C/20 in an electrochemical window of 1.6 V – 4.5 V. In addition, all cycles shown are for the second charge and discharge cycles for each cathode.

Within these cycling parameters, $Na_3V_2(PO_4)_2F_3$ exhibited a charge capacity of 109 mAh/g and a discharge capacity of 100 mAh/g, which can be seen in a voltage versus capacity plot in Figure 3-7. The characteristic voltage plateaus at 3.6 V and 4.2 V from both the literature and Section 3.1 of this work are observed in addition to a third, small plateau at 3.3 V [49, 50]. This corresponds to electrochemical activity of $Na_3V_2(PO_4)_3$, an impurity present in the cathode sample, as indicated in the XRD spectra shown in Figure 3-5 [47]. The observed performance is ∼80% of that observed in the literature, but for the purposes of this study it is sufficient to compare its electrochemical behavior of other the other compounds examined.

Capacity versus voltage curves for $Na_3Ti_2(PO_4)_2F_3$ and $Na_3TiV(PO_4)_2F_3$ are shown in Figure 3-7. For $Na_3Ti_2(PO_4)_2F_3$ a second-cycle charge capacity of 64 mAh/g and discharge capacity of 66 mAh/g was observed, which exceeds previously reported values of capacity in this compound [50]. In the capacity versus voltage curve, there are two distinct plateaus. The major plateau occurs near 2.4 V, accounting for 35 mAh/g, while the significantly smaller plateau at 2.8 V accounts for 10 mAh/g. These values match those reported by Chihara et al.[50]. $Na_3TiV(PO_4)_2F_3$ exhibited a second cycle charge capacity of 76 mAh/g and second cycle discharge ca-

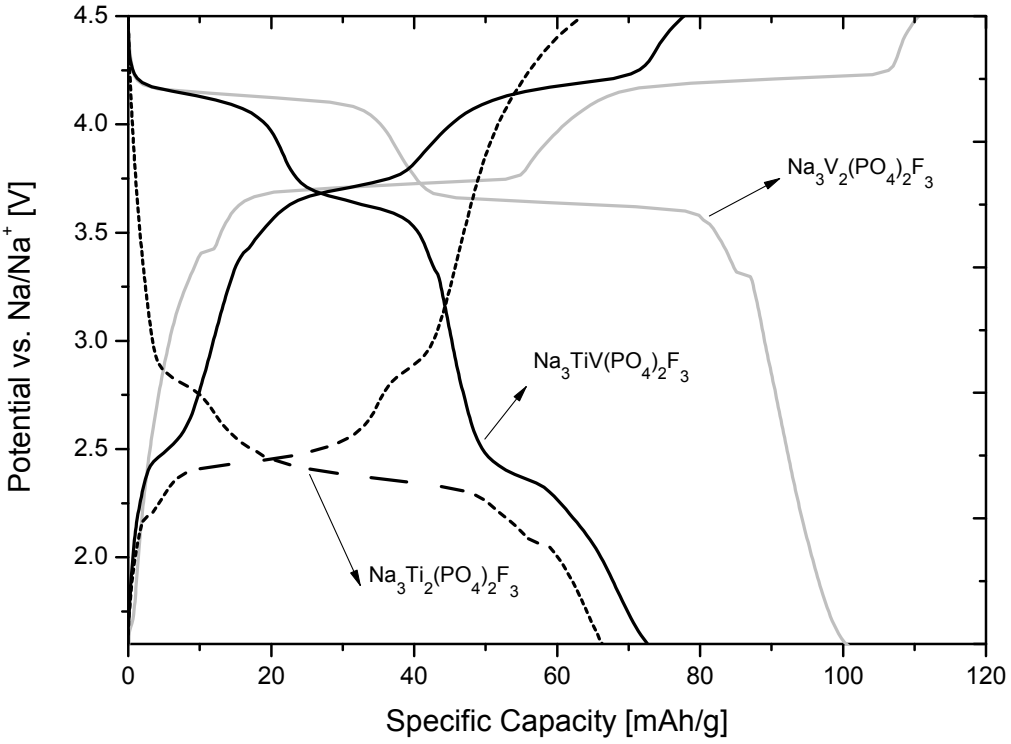

Figure 3-7: Voltage versus capacity curves for $Na_3V_2(PO_4)_2F_3$, $Na_3Ti_2(PO_4)_2F_3$, and $Na_3TiV(PO_4)_2F_3$. The curves are overlaid to elucidate the similarities between the mixed- and single-transition metal compounds. All cycles shown are the second full electrochemical cycle of each cathode.

pacity of 72 mAh/g. Three distinct voltage plateaus exist on capacity versus voltage curve shown in Figure 3-7 at 4.2 V, 3.6 V, and 2.4 V and contribute approximately 25 mAh/g, 20 mAh/g, and 15 mAh/g, respectively. The plateaus at 4.2 V and 3.6 V correspond well to the two plateaus in $Na_3V_2(PO_4)_2F_3$, while the voltage plateau at 2.4 V seems to match the major plateau seen for $Na_3Ti_2(PO_4)_2F_3$. Qualitatively examining the voltage curve for $Na_3TiV(PO_4)_2F_3$, it resembles a normalized linear combination of the voltage curves for the single-transition metal $Na_3V_2(PO_4)_2F_3$ and $Na_3Ti_2(PO_4)_2F_3$ cathodes.

Galavanostatic cycling data for a rate of C/20 is presented for $Na_3V_2(PO_4)_2F_3$, $Na_3Fe_2(PO_4)_2F_3$, and $Na_3FeV(PO_4)_2F_3$ in Figure 3-8. A second cycle charge and discharge capacity of 54 mAh/g and 56 mAh/g is observed for $Na_3Fe_2(PO_4)_2F_3$. In contrast to Ti- and V-only cathodes, the voltage curve exhibits a near-linear slope between 3 V and 1.6 V. In $Na_3FeV(PO_4)_2F_3$, galvanostatic testing resulted in a second cycle charge capacity of 102 mAh/g and a discharge capacity of 101 mAh/g. Qualitatively, the behavior of $Na_3FeV(PO_4)_2F_3$ is closely resembles that of $Na_3Fe_2(PO_4)_2F_3$, but with a significantly higher capacity and average voltage. This consistently-sloped voltage profile does not resemble that of $Na_3V_2(PO_4)_2F_3$ qualitatively, but exhibits a similar discharge capacity.

3.3.4 Discussion of results and viability of mixed-TM fluorophosphate cathodes as high-performing cathodes

Ultimately, all single- and double-transition metals of the designed fluorophosphate cathode template $Na_3[M]_2(PO_4)_2F_3$, where {M = Fe, Ti, V}, were able to be synthesized for this study. Out of this set, $Na_3V_2(PO_4)_2F_3$ performed significantly better than any of the synthesized compounds. All compounds performed significantly be-

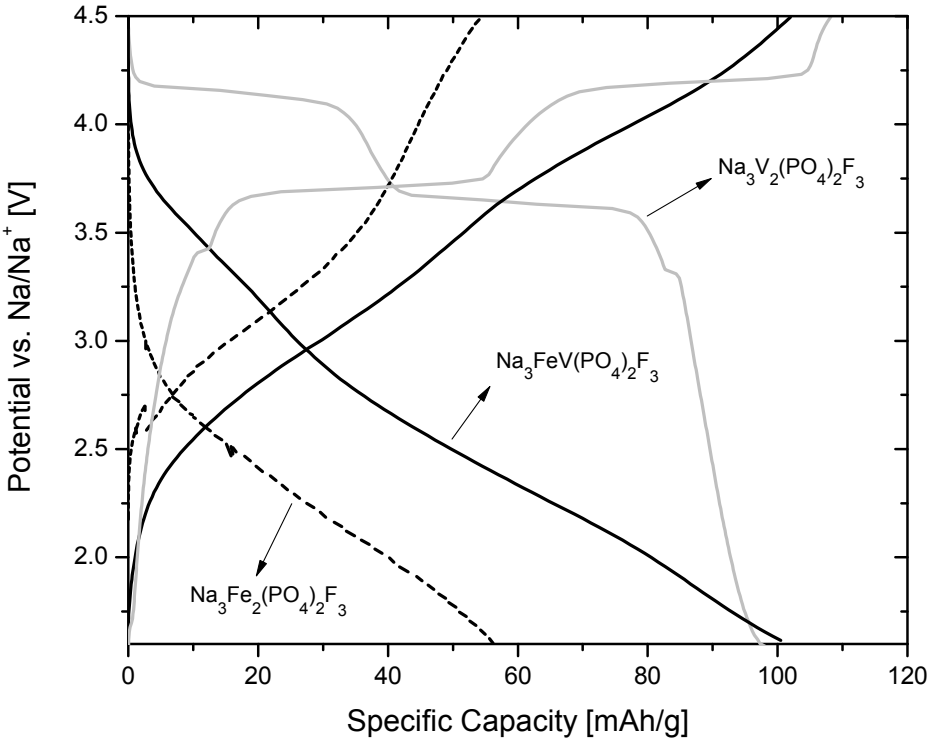

Figure 3-8: Voltage versus capacity curves for $Na_3V_2(PO_4)_2F_3$, $Na_3Fe_2(PO_4)_2F_3$, and $Na_3FeV(PO_4)_2F_3$. The curves are overlaid to show the similarities between the mixed- and single-transition metal compounds. All cycles shown are the second full electrochemical cycle of each cathode

low theoretical values outlined in the cathode template shown in Figure 3-4. Most interestingly, despite the mixed-transition metal compositions, $Na_3TiV(PO_4)_2F_3$ and $Na_3FeV(PO_4)_2F_3$, share voltage curve features and similar capacity to $Na_3V_2(PO_4)_2F_3$, respectively, their electrochemical activity is not increased. Further, even though $Na_3V_2(PO_4)_2F_3$ and $Na_3FeV(PO_4)_2F_3$ demonstrate similar capacities, the V^{3+}/V^{4+} redox couple has a higher average voltage than those in the mixed-transition metal compositions, meaning $Na_3V_2(PO_4)_2F_3$ has the highest energy density. In the case of $Na_3FeV(PO_4)_2F_3$, it is possible that the significant impurity phase contributed to its electrochemical behavior, but ultimately it seems that the capacity of the studied fluorophosphate cathodes is pinned for some reason at or near the performance of $Na_3V_2(PO_4)_2F_3$. The mechanism by which Na-ion fluorophosphate cathodes may be limited is not clear. If it is possible to elucidate any limiting mechanisms then it would also be theoretically possible to either better design this family of cathodes or determine if it is not possible to improve on $Na_3V_2(PO_4)_2F_3$. Regardless, identification of factors limiting the attainable peak performance of fluorophosphate cathodes would be of great interest to the Na-ion battery research community.

3.4 Explaining performance-limiting mechanisms in fluorophosphate Na-ion battery cathodes through inactive transition-metal mixing and first-principles mobility calculations

3.4.1 Background of limited electrochemical behavior in fluorophosphate cathodes for Na-ion batteries

The preceding work in this chapter on $Na_3V_2(PO_4)_2F_3$, $Na_3Ti_2(PO_4)_2F_3$, $Na_3TiV(PO_4)_2F_3$, $Na_3Fe_2(PO_4)_2F_3$, and $Na_3FeV(PO_4)_2F_3$, as well as published works on fluorophosphates and oxyfluorophosphates by Yamaki, Rojo, Kang, Goodenough, and others, all fail to increase the observed capacity of this family of cathodes beyond their single-electron capacity [50, 51, 49, 170, 171]. From this, there appears to be an intrinsic limiting factor preventing fluorophosphates from accessing their full multi-electron capacity. Therefore, it is necessary to determine the source of the observed limitation of capacity in $Na_3V_2(PO_4)_2F_3$-type cathodes. Specifically, the capacity limit must stem from an inability to expand the vanadium redox past one electron per transition metal ion. Further, the limit must be the result of either a limitation in the accessible redox states of vanadium during a single cycle or limitations in moving sodium in and out of the cathode crystal structure. For conciseness, these will be referred to as "redox-limited" and "site-limited" cases for the remainder of this thesis. Determining this source for $Na_3V_2(PO_4)_2F_3$ is especially complex because as-synthesized $Na_3V_2(PO_4)_2F_3$ has partially occupied Na^+ sites, vanadium can potentially exist in four redox states, and fluorine and phosphate anions tend to lead to relatively insulating phases. As such, research strategies might focus on

the working ion, transition metal ions, or anions depending on the source of capacity limitation. This will focus on explaining observed capacity limits via the experimental mixing of judiciously chosen transition metals and computational examination of ion mobility.

3.4.2 $Na_3GaV(PO_4)_2F_3$ as a test system to elucidate fluorophosphate limiting behavior

To pinpoint the source of the observed capacity limit in fluorophosphate cathodes, a combined experimental and first-principles calculations approach was used. First, to decouple the Na concentration from the vanadium redox state and clarify either redox-limiting or site-limiting behavior for material capacity, electrochemically inactive Ga^{3+} was incorporated in the crystal structure's vanadium site with the synthesis of $Na_3GaV(PO_4)_2F_3$. The dilution of the active transition metal forces the vanadium redox to extend over a wider activity range, while the overal change in sodium concentration remains constant. Figure 3-9a shows the electrochemical cycling characteristics of $Na_3V_2(PO_4)_2F_3$ schematically, with composition and capacity on the x axis and the corresponding calculated redox potentials for each regime labeled. Figure 3-9 schematically shows the rationale by which the in-depth examination of the $Na_3GaV(PO_4)_2F_3$ test system may shed light on limiting factors in the fluorophosphate cathode system. Figures 3-9b and 3-9c show how the observed capacity and redox activity in $Na_3GaV(PO_4)_2F_3$ can differentiate between "redox-limited" and "site-limited" behavior. Specifically, it shows how this cathode study may be informative from the perspective of decoupled sodium concentration and vanadium redox limits. From the results of electrochemical characterization, which will be discussed later, one can conclude that the origin of capacity limitation is not due to vanadium

redox accessibility, motivating the first-principles investigation of the energetics and mobility associated with Na sites in the fluorophosphate crystal structure. From the computational study, it is shown that the capacity limitation in the discharged limit originates from prohibitively large diffusion barriers in the cathode crystal structure. In the charged limit, however, no kinetic limitation to Na^+ intercalation is observed and it is surmised that strongly stabilized sodium orderings might be responsible for the capacity constraint. Finally, pragmatic suggestions to overcome these limitations are offered.

3.4.3 Experimental Methods for examining redox activity

Material Synthesis

$Na_3V_2(PO_4)_2F_3$ and $Na_3GaV(PO_4)_2F_3$ samples were made using a standard two-step solid-state synthesis method similar to that previously presented both in this chapter and in the literature for fluorophosphate cathodes [49]. To synthesize $Na_3V_2(PO_4)_2F_3$, stoichiometric amounts of V_2O_5 (Alfa Aesar, 99.2%) and $NH_4H_2PO_4$ (Sigma Aldrich, 99.999%) were mixed with 15% carbon black (Super P) by mass. For $Na_3GaV(PO_4)_2F_3$, the starting mixture composed of stoichiometric amounts V_2O_5 (Alfa Aesar, 99.2%), Ga_2O_3 (Sigma Aldrich, >99.99%), and $NH_4H_2PO_4$ (Sigma Aldrich, 99.999%) was mixed with 15% carbon black (Super P) by mass. For $Na_3V_2(PO_4)_2F_3$, the mixture was pelletized and heated to 750^oC under flow of argon for 4 hours. For $Na_3GaV(PO_4)_2F_3$, the mixture was pelletized and heated to 850^oC under flow of argon for 8 hours. Both resultant mixtures were then crushed, mixed a with stoichiometric mass of NaF, pelletized again, and calcined at 750^oC for 2 hours under flow of argon.

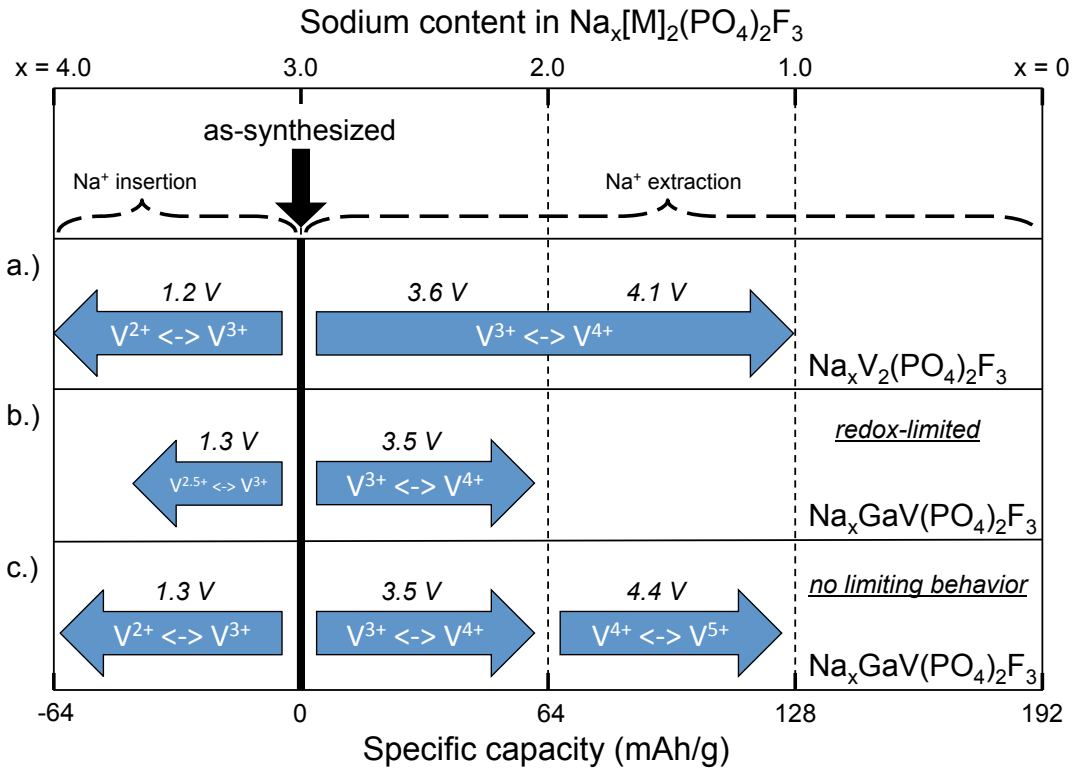

Figure 3-9: A graphical representation of theoretical redox activity between 1 V and 4.5 V for (a) $Na_xV_2(PO_4)_2F_3$ and $Na_xGaV(PO_4)_2F_3$ under the assumptions of (b) redox-limiting and (c) no limiting behavior as a function of Na content. Performance of $Na_xGaV(PO_4)_2F_3$ between (b) and (c) would indicate site-limited behavior. The calculated voltage of each redox reaction is also labeled.

Sample Characterization

Phases present in the synthesized samples were identified by powder XRD. XRD measurements were taken using a Rigaku Miniflex II diffractometer (chromium Kα, $\lambda = 2.2897$ Å, Rigaku corporation, Tokyo) in flat-plate mode, scanning from 15^o to 65^o two-theta. Lattice parameters in the single-phase polycrystalline sample were determined through diffraction data via Rietveld refinement using HighScore Plus software (PANalytical, Netherlands).

The synthesized samples were ball-milled with carbon in a Retsch PM200 planetary ball mill to improve the material's electrochemical performance through decreased particle size and carbon coating [161, 160]. The milling was completed in zirconia-lined milling jars that were loaded in a 80:20 ratio by mass with active material and Carbon (Super P), respectively, in an argon-filled glove box. The samples were milled for 4 hours at 400 rpm, and the resultant powder was unloaded in the Ar-filled glove box to limit air exposure.

For electrochemical characterization, electrode films were made using a dry-rolling method. PTFE binder was added to each ball-milled active material mixture such that the final ratio of components in the prepared electrodes was 76:19:5 by mass, respectively. Cathode films were made by rolling the mixture on a steel plate. Each cathode contained approximately 2 mg of fluorophosphate active material. Battery cells were made using Swagelok cells with stainless steel current collectors, the dry-rolled cathode films described, glass fiber separator films, a solution of 1 M $NaPF_6$ in ethylene carbonate/diethyl carbonate (1:1) as electrolyte, and a Na metal anode. Galvanostatic experiments were conducted at a rate of C/20 on an Arbin Instruments (College Station, TX) battery cycler.

Computational Methods for examining diffusion behavior

Computational work used in this study was completed by Stephen Dacek, a theory-focused graduate student in the Ceder Group [173]. All calculations were performed using the Vienna Ab-initio Software Package (VASP) within the projector augmented-wave approach using the Perdew-Burke-Ernzerhof generalized-gradient approximation (GGA) functional and the GGA + U extension [174, 175, 176]. A plane-wave energy cut off of 520 eV and a k-point grid of a least 1000 divided by the number of atoms in the unit cell were used for all total energy calculations. All structural relaxations were converged to within 1 meV $atom^{-1}$. A U value of 3.1 eV for vanadum was used in GGA + U calculations for structural relaxations, following the procedure outlined by Jain et al. [177].

Na^+ migration barriers and vacancy migration barriers were investigated using the Nudged Elastic Band (NEB) method, as implemented within the VTST tools package as an extension to VASP [178, 179]. In contrast with other total energy calculations, all NEB calculations were performed within the standard GGA (U = 0 eV) functional. The +U for NEB calculations has been forgone due to difficulties converging GGA+U calculations as the the result of metastability of electronic states along the Na^+ migration path [180]. In addition, there has been no conclusive evidence showing that GGA+U performs better at predicting cation migration barriers [4, 181, 182, 183, 184] despite improving the accuracy of redox reaction calculations [185]. The diffusion barriers were calculated using a 2 x 2 x 2 gamma centered k-point grid and with lattice parameters constrained to those of the un-defected (GGA) relaxed structures.

Phase diagram and voltage curve construction/analysis was performed using the Python Materials Genomics (pymatgen) library and VASP relaxation calculations

were performed using the custodian package [186, 177].

3.4.4 Experimental Results

Synthesis results

$Na_3GaV(PO_4)_2F_3$ was synthesized as a single-phase sample of the desired $P4_2/mnm$ space group. XRD spectra for this sample is presented in Figure 3-10. The sharp, non-doublet peaks in the figure indicate that the gallium and vanadium ions in the mixture are not phase-separated. In addition, experimental versus calculated lattice parameters for $Na_3GaV(PO_4)_2F_3$ are presented in Table 3.1 and show excellent agreement within the accuracy of what is expected from DFT/PBE + U. The experimental lattice parameters were determined using Rietveld refinement.

Table 3.1: Lattice parameters of $Na_3GaV(PO_4)_2F_3$ from XRD (Rietveld Refinement) and DFT (GGA + U). The DFT error bars for a, b, c, and volume are 1.1%, 2.0%, 1.3%, and 4.3%, respectively.

		a (Å)	b (Å)	c (Å)	Volume (Å^3)
$Na_3GaV(PO_4)_2F_3$	XRD	8.98(9)	8.98(9)	10.70(4)	864.9
	DFT	9.081	9.131	10.805	895.9

Electrochemical characterization results

An electrochemical cycling curve for $Na_3GaV(PO_4)_2F_3$ is presented in Figure 3-11, with a curve for $Na_3V_2(PO_4)_2F_3$ included for comparison. The data were obtained under galvanostatic conditions at a rate of C/20 in a voltage window of 1.2 V - 4.5 V. In addition, both cycles shown are the for the second charge/discharge cycle.

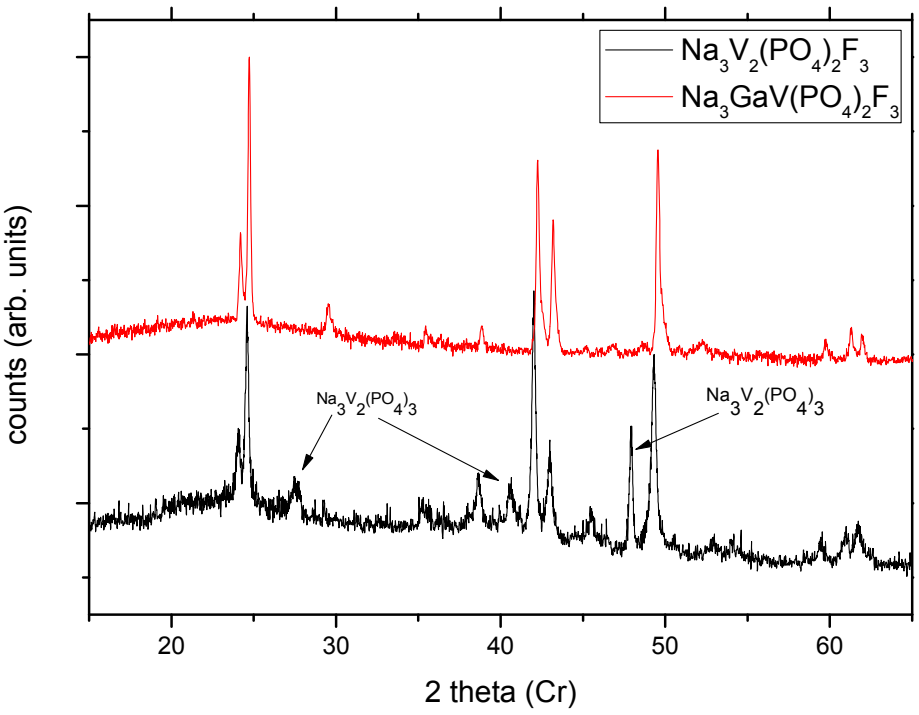

Figure 3-10: Collected XRD spectra for as-synthesized $Na_3V_2(PO_4)_2F_3$ and $Na_3GaV(PO_4)_2F_3$. Impurity peaks are labeled in the spectra.

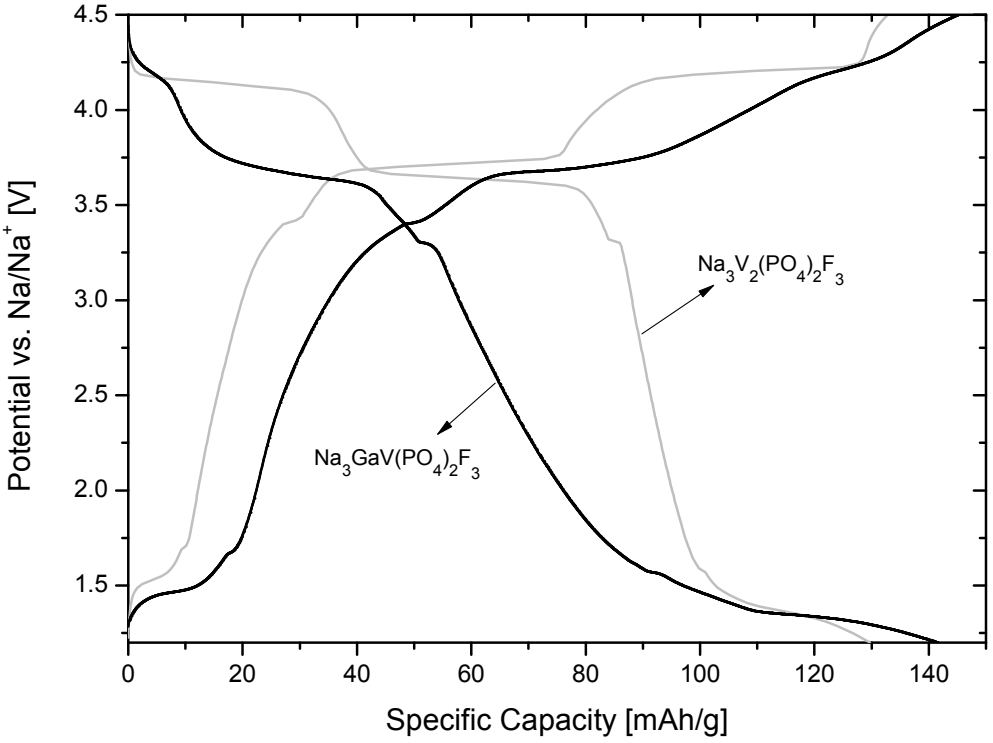

Figure 3-11: Voltage versus capacity curves for $Na_3GaV(PO_4)_2F_3$ and $Na_3V_2(PO_4)_2F_3$. The second cycle for each compound is shown.

During electrochemical cycling of $Na_3GaV(PO_4)_2F_3$ second cycle charge and discharge capacities of 144 mAh/g and 141 mAh/g, respectively, is observed. Distinct plateaus are seen in the capacity versus voltage curve at 4.2 V, 3.7 V, and 1.4 V, indicating activity of vanadium redox states V^{2+} through V^{5+}. These observed voltage plateaus correspond well to the calculated voltages for the material from DFT. A calculated voltage versus capacity curve is overlaid on the experimental cycling data of $Na_3GaV(PO_4)_2F_3$ in Figure 3-12. In the figure, the capacity of the calculated curve is aligned to line up with the portion of the curve corresponding to V^{3+}/V^{4+} activity. As with the cycling curves for $Na_3V_2(PO_4)_2F_3$, small plateaus are also present in the $Na_3GaV(PO_4)_2F_3$ data at 3.3 V and 1.7 V, indicating the likely presence of an electrochemically active $Na_3V_2(PO_4)_3$ impurity. However, no impurity is clear in the XRD spectra shown in Figure 3-10.

3.4.5 Discussion of Experimental Investigation

The observed performance of $Na_3V_2(PO_4)_2F_3$ in this study at voltages between 2.0 V and 4.5 V ($\sim$95 mAh/g) is around 80% of that observed in the literature [49, 50]. Given the unoptimized nature of the cathode, this level of performance is acceptable for this study. For clarity, Table 3.2 is included, in which the capacities of the tested materials is separated into extraction and insertion regimes. Capacity below 2 V is taken to be attributed to electrochemical insertion, which was proven to occur in Section 3.2, and capacity above 2 V to be the result of electrochemical extraction of Na^+.

For $Na_3GaV(PO_4)_2F_3$, the strategy was to use an inactive 3+ dopant to test full range of possible vanadium redox while keeping the Na^+ extraction amount within known bounds, and in doing so deconvolute Na^+ extraction limitations from redox

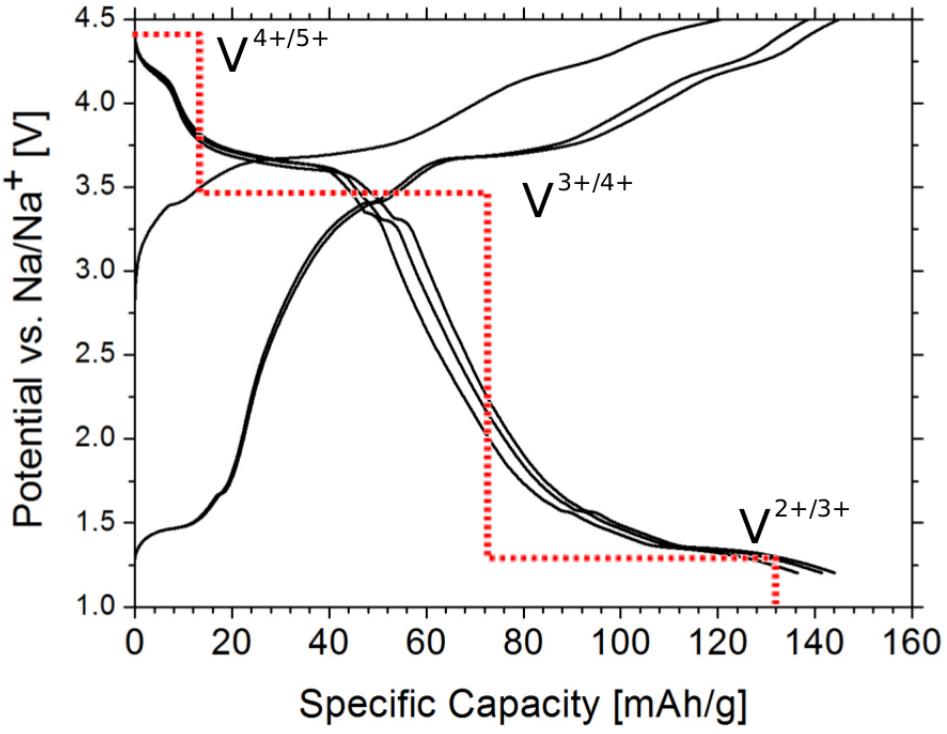

Figure 3-12: Voltage versus capacity curve for $Na_3GaV(PO_4)_2F_3$. A computed voltage versus capacity curve is overlaid with the predicted redox couples active at each plateau is labeled.

Table 3.2: The observed capacities of $Na_3V_2(PO_4)_2F_3$ and $Na_3GaV(PO_4)_2F_3$ separated into the individual contributions of electrochemical Na-ion insertion (1.2 V - 2.0 V) and extraction (2.0 V - 4.5 V) for the second cycle of each compound.

Compound	**Half-cycle**	**Capacity (1.2 V-2.0 V)**	**Capacity (2.0 V-4.5 V)**
$Na_3V_2(PO_4)F_3$	Charge	13 mAh/g	119 mAh/g
	Discharge	33 mAh/g	96 mAh/g
$Na_3GaV(PO_4)F_3$	Charge	22 mAh/g	122 mAh/g
	Discharge	64 mAhg	77 mAh/g

limitations in fluorophosphate cathodes. If it is possible to fully access vanadium redox states between V^{2+} and V^{5+}, the cathode would cycle between $Na_4GaV(PO_4)_2F_3$ and $NaGaV(PO_4)_2F_3$, yielding a capacity of 186 mAh/g. The electrochemical performance for this case is shown schematically in Figure 3-9c. Conversely, if vanadium is fully redox limited in this structure, that is, if the amount of extractable Na^+ per vanadium ion is fixed and equal to that observed in $Na_3V_2(PO_4)_2F_3$, the capacity would be halved, leading to an observed capacity of ∼90 mAh/g upon electrochemical cycling, as shown schematically in Figure 3-9b. Additionally in the case of $Na_3GaV(PO_4)_2F_3$, a greater portion of the observed capacity lies below 2 V, which is deemed to be voltages at which electrochemical insertion is occurring. Figure 3-12 shows the first three complete electrochemical cycles for $Na_3GaV(PO_4)_2F_3$, and, as such, shows good reversibility for the material, particularly for the insertion regime in which the V^{2+}/V^{3+} redox couple is active. In addition, Figure 3-12 has a calculated voltage curve overlaid including all three redox couples of vanadium in the mixed transition metal compound. The curve agrees well with the experimental data, giving further support to the idea that $Na_3GaV(PO_4)_2F_3$ is capable of reversible Na^+ insertion at voltages below 2 V.

During the electrochemical cycling of $Na_3GaV(PO_4)_2F_3$ above 4 V, a small reversible voltage plateau is observed. The capacity observed between 2 V and 4 V corresponds well to the theoretical capacity and calculated voltage of the V^{3+}/V^{4+} redox couple in $Na_3GaV(PO_4)_2F_3$, so at 4 V, the average valence of vanadium would V^{4+}. Thus, this plateau can not correspond to V^{3+}/V^{4+} activity, and by extension it can be inferred that it must come from activity of the V^{4+}/V^{5+} redox couple, even though the vanadium valence state has not been directly observed. Combined, the observed voltage curve is consistent with the occurrence of V^{2+}, V^{3+}, V^{4+}, and V^{5+} on a single charge or discharge. The reversible capacity implies electrochemical cycling between

a Na content of approximately $Na_{1.8}GaV(PO_4)_2F_3 \leftrightarrow Na_{3.5}GaV(PO_4)_2F_3$. This capacity of 141mAh/g significantly exceeds 90mAh/g, which is the "redox-limited" case described in previously in Figure 3-9. As a result $Na_3GaV(PO_4)_2F_3$, and by extension $Na_3V_2(PO_4)_2F_3$, is not fundamentally limited by the redox activity of vanadium. However, the discharge capacity of 141mAh/g falls short of the "unlimited" case, also outlined in Figure 3-9. Therefore, $Na_3GaV(PO_4)_2F_3$ must be site limited.

3.4.6 Computational Results

By synthesizing and electrochemically characterizing the $Na_3GaV(PO_4)_2F_3$ system, the source of observed capacity limitation in the $Na_3V_2(PO_4)_2F_3$ system can be attributed to a limitation in the Na^+ intercalation process rather than a limit in transition metal oxidation/reduction. Such site-limited performance is rooted in the material's thermodynamics and/or kinetics due to the energetic relationships of available Na sites and the migration barriers between them, and can be manifested in concentration-dependent diffusivity. From GITT experiments performed by Liu et al., the Na chemical diffusivity is observed at its highest ($D_{Na} \approx 10^{-6.2} cm^2/s$) at x_{Na} = 1.6 with drops in the diffusivity at both increasing and decreasing concentrations ($D_{Na} \approx 10^{-7.2} cm^2/s$ at x_{Na}=2.7, and $D_{Na} \approx 10^{-8} cm^2/s$ at x_{Na}= 1) [187]. To isolate the physical origin for the variation in Na diffusivity, first-principles mobility calculations in the dilute Na and dilute Na vacancy concentration limits (i.e. x_{Na} = 0 and x_{Na} = 4) have been performed.

Two-dimensional Na diffusion occurs within *a*-*b* planes (z = 0) of the idealized $Na_3V_2(PO_4)_2F_3$ structure as shown in Figure 3-13a, superimposed above a schematic drawing of the Na layer. In this structure, Na ions (yellow) are encapsulated within 6+1 prismatic polyhedra composed of 3 fluorine atoms (blue) and 4 oxygen atoms

(red). For clarity, phosphorus atoms (purple), which lie above and below (± 0.25) the $z = 0$ plane, are shown and the $V_2(PO_4)_2F_3$ bi-octahedra are omitted. Within Figure 3-13a, the three symmetrically distinct Na sites are shown: (1) Na1 sites are aligned such that the prismatic site's bisector in the a-b plane is parallel the a axis; (2) Na2 sites with the prismatic site's bisector is aligned along the b axis; and (3) Na3 sites (denoted by black squares in Figure 3-13a) bridge the Na1 and Na2 sites [172]. From the idealized crystal structure, there are three distinct diffusion paths, shown in Figure 3-13b and 3-13c. Path 1 captures the motion between a Na1 and a Na2 site, passing through the adjoining Na3 site. Path 2 captures the motion between a Na1 and a Na2 site passing through two adjoining Na3 sites. Path 3 captures the motion between neighboring Na1 sites and requires diffusion through two Na3 sites. Under symmetry of this material in the fully sodiated and desodiated limits, the diffusion between neighboring Na2 sites is also described by Path 3.

In Figures 3-13b and 3-13c, the migration energies corresponding to Paths 1, 2, and 3 in the $Na_3V_2(PO_4)_2F_3$ structure are shown in green, orange, and red, respectively, against their normalized path lengths in the fully sodiated (dashed) and desodiated limits (solid). In both limits, Path 1 barriers are much lower (∼20-45 meV) than the Path 2 (∼300-600 meV) and Path 3 (∼300-1100 meV) barriers. The shape of the migration energy for Path 1 in Figure 3-13b can be understood by considering the idealized trajectory highlighted in Figure 3-13a in green, as the local minimum observed halfway through the diffusion path corresponds to the Na3 site. Although the Path 1 barrier is relatively unchanged in the sodiated limit, the Path 2 and Path 3 barriers (solid red and orange lines in Figure 3-13c) change significantly. In the desodiated limit, the Path 2 and Path 3 migration energies overlap, consistent with the fact that they become identical under the symmetry of the desodiated state. Both trajectories pass through two Na3 sites, which correspond to the subtle dips

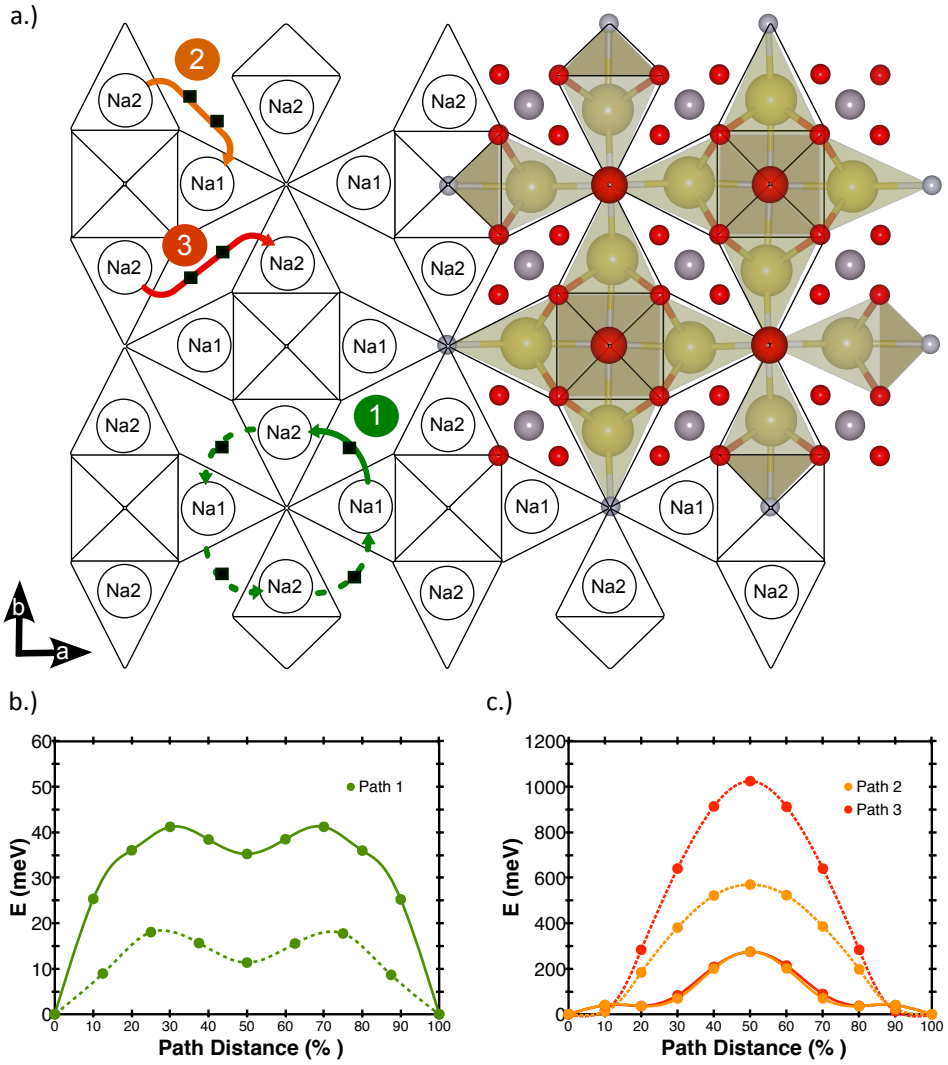

Figure 3-13: (a) A schematic image of the $Na_xV_2(PO_4)_2F_3$ crystal structure in a Na (z = 0) plane. Na1 and Na2 Na sites are marked and filled as would be expected in the fully occupied $Na_4V_2(PO_4)_2F_3$ crystal structure. A structure image with yellow 6+1 coordinated, capped prismatic Na sites is shown, overlaid for clarification. Idealized diffusion paths are drawn and labeled 1, 2, and 3. Black squares are drawn within these paths to demonstrate diffusion through six-fold coordinated prismatic Na3 sites. Path 1 is repeated to demonstrate the ring pattern associated with consecutive path 1 jumps. (b) Diffusion barriers for path 1 in the sodiated (dotted) and desodiated (solid) limits. (c) The diffusion barriers for path 2 (orange) and path 3 (red) in the sodiated (dotted) and desodiated (solid) limits.

in the migration energy observed at ∼20% and ∼80% of the path length, and the activated state in between corresponds to crossing the shared face between the two prismatic Na3 sites. In the sodiated limit, however, the Path 2 and Path 3 barriers both increase (dashed lines in Figure 3-13c), but by different amounts, which can be rationalized by considering the additional electrostatic interaction of nearby Na^+. For Path 2, the electrostatic repulsion of the nearest two Na^+ results increases the energy of the activated state and also alters the trajectory of the migrating Na^+ which performs a "tighter turn" to the adjacent Na site. For Path 3, however, the two nearest Na are on opposite sides of the diffusion trajectory, so the readjustment of the path as observed for Path 2 is no longer possible. Consequently, the migration barrier for Path 3 is significantly higher in the fully sodiated limit.

3.4.7 Discussion of Computational Study

If Na^+ intercalation were to proceed exclusively through Path 1 hops, then by these calculations, one would expect the diffusivity to be 4 to 5 orders of magnitude greater than the observed values [187]. For reference, assuming a random walk model of diffusion, a migration barrier of ∼300 meV roughly corresponds to a diffusivity of $10^{-9} cm^2/s$ at room temperature (given an atomic jump frequency $\nu = k_B T/h = 6.2 \times 10^{12} s^{-1}$ and a jump distance a of ∼3 Å), and an increase of 60 meV in the migration barrier corresponds to a decrease in the diffusivity by an order of magnitude. However, by virtue of the $Na_3V_2(PO_4)_2F_3$ crystal topology, the Na sites do not percolate without Path 2 or Path 3 hops. In other words, Na^+ would be restricted to performing circular "laps" fixed in space as depicted by the dashed green arrows forming a circle in Figure 3-13a and do not contribute to net mean-squared displacement.

The frequency of Path 2 and Path 3 hops then determines the diffusivity which is estimated using a simple random walk model. At every Na1 or Na2 site there are there are two of each possible diffusion pathways (Path 1, Path 2, or Path 3) available. Since the energy barrier for Path 1 migration is the lowest, it occurs the most often, lowering the frequency of diffusion along paths that contribute to the mean squared displacement, which are Paths 2 and 3, and leading to locally correlated diffusion. The diffusion behavior in the fully sodiated and desodiated limits can be therefore reduced to a two-dimensional random walk with the jump frequency related to the residence time of a Na ion (or vacancy) in the fast diffusing rings depicted in Figure 3-13a in green and the jump length equal to the distance between ring-centers (6.3 Å). The larger the discrepancy in the migration barrier between fast Path 1 hops and slower Path 2 and Path 3 hops, the larger the Na residence time and therefore slower diffusion. From statistical mechanics, the probability p_1 that a Na^+ moves from a Na1 site through a single Na3 site to a Na2 site, or a Path 1 hop in Figure 3-13a, is given by

$$p_1 = \frac{exp(-E_1/kT)}{exp(-E_1/kT) + exp(-E_2/kT) + exp(-E_3/kT)} \tag{3.1}$$

where E_1, E_2, and E_3 are the corresponding migration barriers shown in Figure 3-13b and Figure 3-13c. The average number of Path 1 hops before a single Path 2 or Path 3 hop occurs is then $1/(1-p_1)$ which is 2.14×10^9 in the sodiated limit (4.49×10^3 in the desodiated limit). From this probability the diffusivity in the Na layer can be approximated as

$$D_{2D} \approx \frac{a^2}{4 \cdot t_{res}} \tag{3.2}$$

where a is the distance between ring centers (6.4 Å in the sodiated limit and 6.3 Å in the desodiated limit) and t_{res} is the residency time of a Na atom (or Na vacancy) within an individual ring, in seconds, defined as

$$t_{res} = \frac{< t >}{(1 - p_1)} = \frac{1}{\Gamma} \cdot \frac{1}{(1 - p_1)} = \frac{1}{2 \cdot \nu \cdot exp(-E_1/kT) + 2 \cdot \nu \cdot exp(-E_2/kT)} \quad (3.3)$$

where $< t >= 1/\Gamma$ is the mean time for any hop, $\nu = 6.2 \times 10^{12}$ s^{-1} is the assumed atomic jump frequency, and $\Gamma = \sum_i \Gamma_i$ where

$$\Gamma_i = N_i \cdot \nu \cdot exp(E_i/kT) \quad (3.4)$$

for each barrier E_i and path multiplicity N_i. From this, the reported barriers correspond to calculated diffusivities of the order $4.7 \times 10^{-13} cm^2/s$ and $8.9 \times 10^{-8} cm^2/s$ in the fully sodiated ($x_{Na} = 4$) and desodiated ($x_{Na} = 0$) limits, respectively.

The large variation between the calculated diffusivities from the fully charged to discharged limit arises from an increase in the migration barriers for Path 2 (E_2) and Path 3 (E_3), from ∼300 meV to 600 meV and ∼300 meV to 1000 meV, respectively. The dependence of the local Na occupation on the Path 2 and Path 3 barriers strongly suggests that Na^+ diffusion proceeds preferentially through a divacancy mechanism, which would result in a decrease in the Na^+ diffusivity with increasing Na^+ intercalation due to the reduced concentration of mobile carriers (divacancies), a phenomenon well-known in the Li_xCoO_2 system as extensively characterized by

Van der Ven et al.[188]. Indeed, the existence of a preferred divacancy mechanism agrees with the general trend of increasing diffusivity upon charge has been observed by Liu et al. from $x_{Na} = 3$ to $x_{Na} = 1.6$. The abrupt drop in diffusivity that is observed at $x_{Na}<1.6$ by Liu et al., however, can not be explained by the divacancy mechanism. Moreover, the discussed mobility calculations suggest that there is no inherent kinetic limitation to accessible capacity in the low Na concentration.

Although it is determined that the apparent capacity limitation in the charged limit is not purely kinetic in origin, it is postulated that the capacity limitation is then thermodynamic in origin, specifically the result of strong Na^+ orderings at intermediate Na concentrations. If there is a Na^+ ordering strongly stabilized at a given composition, then further intercalation requires not only overcoming the Na^+ migration barrier, but also the additional energy to disrupt the ordering, either by formation of a vacancy during charge or the incorporation of Na^+ during discharge. Effectively, strong ordering interactions between intercalating species appear as regions of high slope in the open-circuit potential, decrease the concentration of mobile carriers, and accordingly reduce the diffusivity. The contribution of orderings to the diffusivity is formally captured in the so-called "thermodynamic factor" in Fick's second law, and has been investigated in detail for the lithium-ion battery cathode material $LiCoO_2$ by Van der Ven et al. [188] who demonstrate that strong orderings at $x_{Li} = 0.5$ and $x_{Li} = 0.33$ cause sudden, sharp, drops in the diffusivity. In the computed $Na_3V_2(PO_4)_2F_3$ voltage curve shown in Figure 3-14, there are noticeable steps in the voltage at $x_{Na} = 1$ and $x_{Na} = 3$, suggesting the specific concentrations where one would expect abrupt decreases in the Na^+ diffusivity. Indeed, in the diffusivity measurements performed by Liu et al., the lowest values are measured as these concentrations are approached. The concentration dependence of the diffusivity as measured by Liu et al. is also asymmetric, with a more gradual increase in

the diffusivity upon charge until $x_{Na} = 1.6$ followed by a sharp decline at lower concentrations. This can be attributed to the added contribution of divacancy limited mobility that has greater effect with increasing discharge, and smears out the more sharp effect on the diffusivity caused by the thermodynamic factor. In the charged limit, the Na^+ mobility is no longer limited by the concentration of divacancies, resulting in the more pronounced effect of strong Na^+ ordering.

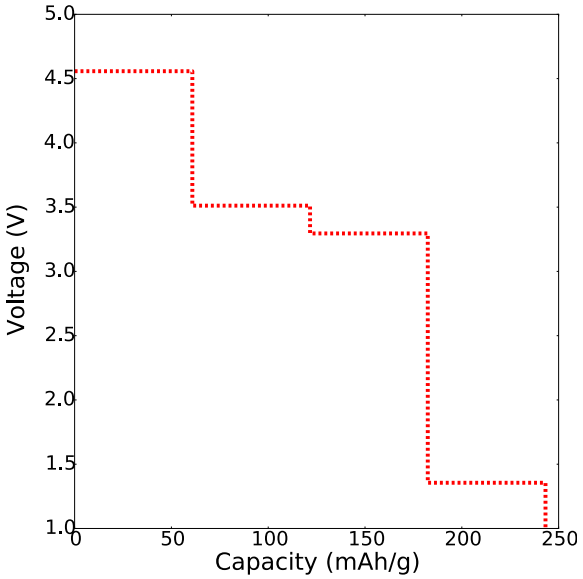

Figure 3-14: A theoretical voltage versus capacity curve for $Na_3V_2(PO_4)_2F_3$ between compositions of $V_2(PO_4)_2F_3$, at left, and $Na_4V_2(PO_4)_2F_3$, at right.

Given the results of the study, some of the specific physical mechanisms responsible for the observed capacity limitation in $Na_3V_2(PO_4)_2F_3$ electrodes have been isolated. Using this clearer understanding one can propose targeted strategies to further improve performance in fluorophosphate cathodes for Na-ion batteries. Given the limitation in Na^+ mobility in the discharged limit due to the limited concentration of mobile divacancies, significant improvement of the insertion capacity is

unlikely. However, there is an opportunity to improve the accessible capacity at the current charged limit, $NaV_2(PO_4)_2F_3$, which has the benefit of being at high voltages (>4 V) and could therefore significantly add to the energy density of these materials. In order to achieve this, it is proposed that the most promising strategy is to disrupt existing ordering interactions in the Na sub-lattice by incorporating atomic substitutions in either the Na or vanadium sublattices. This strategy has been successfully employed by Li et al. [46] in Na-ion battery layered oxide cathodes to suppress phase transitions in $NaMn_{1/4}Fe_{1/4}Ni_{1/4}Co_{1/4}O_2$.

3.4.8 Conclusions from mixed-transition metal fluorophosphate study

In order to investigate the specific physical origin of the capacity limitation of $Na_3V_2(PO_4)_2F_3$ Na-ion battery cathodes, a systematic experimental and theoretical study has been performed to isolate the factors that limit capacity to around its one-electron capacity of 128 mAh/g. To decouple potential limitations from Na concentration from those of the vanadium redox state, V^{3+} was mixed with electrochemically inactive Ga^{3+}, yielding $Na_3GaV(PO_4)_2F_3$. Electrochemical cycling of $Na_3GaV(PO_4)_2F_3$ between 1.2 V and 4.5 V yielded a discharge capacity of 141 mAh/g, with distinct voltage plateaus at 1.5 V, 3.6 V, and 4.2 V. Based on this, it could be inferred that V^{2+}, V^{3+}, V^{4+}, and V^{5+} redox states were all accessible during cycling and concluded that the capacity of $Na_3GaV(PO_4)_2F_3$ is not redox-limited and therefore must be site-limited. Ab-initio computation was employed to gain further insight, and NEB calculations of diffusion barriers showed that high diffusion barriers during Na^+ insertion prohibit significant capacity in the low-voltage regime at reasonable rates. However, high barriers to Na^+ cannot explain the limit

at the top of charge, which leads us to believe Na^+ ordering interactions must be the reason for observed capacity limits. From these results, it is suspected that improvements in fluorophosphate cathodes may be possible if these orderings can be disrupted through atomic substitutions.

3.5 Post-study update

Another paper by Jian et al., also published in 2015, demonstrated the Na^+ insertion behavior of $Na_3V_2(PO_4)_2F_3$ at low voltages seen in this work [81]. This paper, while replicating the insertion behavior observed in this thesis, fails to comment on what the material structure of $Na_4V_2(PO_4)_2F_3$ might be, confirm topotactic electrochemical insertion, or determine why the observed capacity in the $Na_3V_2(PO_4)_2F_3$ crystal structure falls short of the theoretical capacity if all vacant Na sites in as-synthesized $Na_3V_2(PO_4)_2F_3$ can be accessed during cycling.

Another paper by the Tarascon Group following the publication of the results in this thesis [173] does characterize the structure of $Na_4V_2(PO_4)_2F_3$ using synchrotron XRD, and the structure found corresponds to that predicted in this work [189]. Zhang et al., were able to synthesize the fully-sodiated $Na_4V_2(PO_4)_2F_3$ structure by ball-milling $Na_3V_2(PO_4)_2F_3$ with metallic sodium [189]. The results in the work by Zhang et al., while not explicitly saying so, indicate that this group could not reliably cycle a $Na_4V_2(PO_4)_2F_3$ battery, stating that the ideal cycling performance that could be achieved was from a cathode structure of $Na_{3.5}V_2(PO_4)_2F_3$. However, reversible insertion of Na^+ in any of these chemistries is not demonstrated in that publication.

Chapter 4

Conclusion

The societal need for greater energy storage in order to lessen the economy's dependance on fossil fuels is well-established. However, before energy storage technology can be widely implemented in transportation and grid applications, improvements on existing technology are necessary. The current leading technology for these applications, as well as for portable electronics, is the Li-ion battery. It is likely that in order for energy storage to improve dramatically, either new Li-ion battery cathode materials will need to be discovered, or a new technology, such as Na-ion batteries, will need to surpass Li-ion batteries on the basis of performance. The Ceder Group is well-suited to seek such breakthroughs by accelerating the materials discovery process by employing a joint computational-experimental approach. Combined, this motivates the Ceder Group to accelerate materials development and discover new materials for alkali-ion battery cathodes.

In this thesis, two classes of polyanionic materials computationally predicted to have multi-redox activity were studied: Li-containing carbonophosphate cathodes for Li-ion batteries (Chapter 2) and Na-containing fluorophosphates for sodium ion

batteries (Chapter 3), both with novel chemistries. These materials were synthesized and characterized electrochemically. When limits to performance, particularly capacity, were observed, the materials were carefully studied to determine the mechanism responsible, with a focus on how observed limits may influence the class of materials as a whole.

Li-containing carbonophosphate cathodes were previously identified as possible multi-redox Li-ion battery cathodes by high-throughput computational screening methods. This mixed-polyanion chemistry had never before been reported, but was able to be synthesized by the Ceder Group with a variety of different transition metal compositions. Both $Li_3FeCO_3PO_4$ and $Li_3MnCO_3PO_4$ were shown to cycle as battery cathodes, but $Li_3FeCO_3PO_4$ showed low capacity and $Li_3MnCO_3PO_4$ suffered from poor cyclability. In an attempt to improve on these materials, $Li_3Fe_{0.2}Mn_{0.8}CO_3PO_4$ was synthesized to combine the capacity of $Li_3MnCO_3PO_4$ with the cyclability of $Li_3FeCO_3PO_4$. This strategy proved moderately successful, and marginal charging plots showed that all three predicted active redox couples in the tested voltage window were reversibly activated. However, only one electron per transition metal ion was reversibly cycled in total. Ultimately, it was discovered that the low thermodynamic stability of these cathodes leads to decomposition at temperatures as low as 55^oC, making them an unrealistic alternative for current Li-ion batteries even if their theoretical performance could be achieved.

The study of carbonophosphate cathodes for Li-ion batteries is significant for two reasons, despite the potentially disappointing result. First, it provides further evidence for the viability of high-throughput computation as a method to predict novel chemistries and structures that will function as battery materials. Second, it conclusively shows the thermodynamic instability Li-containing carbonophosphates limits their observed performance and prohibits their consideration as a viable Li-ion

battery cathode.

Fluorophosphate cathodes are currently one of the most promising polyanionic sodium-ion battery cathodes. Despite exhibiting high capacity (∼125 mAh/g) and energy density (∼480 Wh/kg) for a polyanionic Na-ion battery cathode, further improvements are needed in order for fluorophosphates to surpass the performance of layered oxide Na-ion cathodes, and ultimately compete with Li-ion battery cathodes. Reversible electrochemical insertion of Na^+ in $Na_3V_2(PO_4)_2F_3$ was demonstrated as a possible means to increase the capacity of fluorophosphate cathodes. Next, a general limitation on fluorophosphate cathode capacity was uncovered when cathodes with chemistries of the form $Na_3[M]_2(PO_4)_2F_3$ with {M = Fe, Ti, V} were synthesized and electrochemically tested. Through careful design and electrochemical testing of $Na_3GaV(PO_4)_2F_3$, along with a computational examination of diffusion barriers in $Na_3V_2(PO_4)_2F_3$, it was then shown that the source of this general limitation comes from Na^+ mobility issues at high Na (low Na-vacancy) concentrations.

This thesis work provides the first conclusive demonstration of reversible insertion of Na^+ into $Na_3V_2(PO_4)F_3$ and predicts the structure of $Na_4V_2(PO_4)F_3$, which was later confirmed by the Tarascon Group. In addition, a generic limit shared in all fluorophphosphates was uncovered through testing of novel compounds of the $Na_3[M]_2(PO_4)_2F_3$ template with {M = Fe, Ti, V}. Further, the ion mobility issue in fluorophosphates, discovered in this thesis work, applies to all fluorophosphate cathodes, and will influence their future development.

Combined, these studies show two examples of how exceeding the current levels of performance of Li-ion cathodes, particularly the newly discovered Li-excess disordered rocksalt cathodes and traditional layered-oxide cathodes, will be difficult for any polyanionic cathode. The advantage given to oxides by the high negative charge density of oxygen and use of low-molecular weight Li as a major component

of the crystal's structural framework may be insurmountable for other systems. The stability of a transition metal-polyanion framework needed to allow the amount of alkali-ion extraction required to compete with these cathodes may not be thermodynamically possible. However, until such a fact is proven, the search for novel cathode compositions is important, if only for use in niche applications such as high power motor batteries. In the opinion of the author, dramatic expansion of the adoption of alkali-ion battery technology is likely, but will come from decreases in cost and improvements in cycle life rather than dramatic improvements in energy density.

Bibliography

[1] J-M Tarascon and Michel Armand. Issues and challenges facing rechargeable lithium batteries. *Nature*, 414(6861):359–367, 2001.

[2] M Saiful Islam and Craig AJ Fisher. Lithium and sodium battery cathode materials: computational insights into voltage, diffusion and nanostructural properties. *Chem. Soc. Rev.*, 43(1):185–204, 2014.

[3] Naoaki Yabuuchi, Kei Kubota, Mouad Dahbi, and Shinichi Komaba. Research development on sodium-ion batteries. *Chem. Rev.*, 114(23):11636–11682, 2014.

[4] Shyue Ping Ong, Vincent L Chevrier, Geoffroy Hautier, Anubhav Jain, Charles Moore, Sangtae Kim, Xiaohua Ma, and Gerbrand Ceder. Voltage, stability and diffusion barrier differences between sodium-ion and lithium-ion intercalation materials. *Energy Environ. Sci.*, 4(9):3680–3688, 2011.

[5] Raphaële J Clément, Peter G Bruce, and Clare P Grey. Review–manganese-based P2-type transition metal oxides as sodium-ion battery cathode materials. *J. Electrochem. Soc.*, 162(14):A2589–A2604, 2015.

[6] Geoffroy Hautier, Anubhav Jain, Hailong Chen, Charles Moore, Shyue Ping Ong, and Gerbrand Ceder. Novel mixed polyanions lithium-ion battery cathode materials predicted by high-throughput ab initio computations. *J. Mater. Chem.*, 21(43):17147–17153, 2011.

[7] Hailong Chen, Geoffroy Hautier, Anubhav Jain, Charles Moore, Byoungwoo Kang, Robert Doe, Lijun Wu, Yimei Zhu, Yuanzhi Tang, and Gerbrand Ceder. Carbonophosphates: a new family of cathode materials for Li-ion batteries identified computationally. *Chem. Mater.*, 24(11):2009–2016, 2012.

[8] PA Okken and Tom Kram. *CH_4/CO - Emission from fossil fuels global warming potential*. Energy Study Centre, Netherlands Energy Research Foundation, 1989.

[9] Malte Meinshausen, Nicolai Meinshausen, William Hare, Sarah CB Raper, Katja Frieler, Reto Knutti, David J Frame, and Myles R Allen. Greenhouse-gas emission targets for limiting global warming to 2^{o}C. *Nature*, 458(7242):1158–1162, 2009.

[10] Martin I Hoffert, Ken Caldeira, Gregory Benford, David R Criswell, Christopher Green, Howard Herzog, Atul K Jain, Haroon S Kheshgi, Klaus S Lackner, John S Lewis, et al. Advanced technology paths to global climate stability: energy for a greenhouse planet. *Science*, 298(5595):981–987, 2002.

[11] Willett Kempton and Jasna Tomić. Vehicle-to-grid power implementation: From stabilizing the grid to supporting large-scale renewable energy. *J. Power Sources*, 144(1):280–294, 2005.

[12] Cristina L Archer and Mark Z Jacobson. Supplying baseload power and reducing transmission requirements by interconnecting wind farms. *J. Appl. Meteorol. Clim.*, 46(11):1701–1717, 2007.

[13] Paul Denholm, Erik Ela, Brendan Kirby, and Michael Milligan. The role of energy storage with renewable electricity generation. Technical report, National Renewable Energy Laboratory, 2010.

[14] Ibrahim Dincer. Renewable energy and sustainable development: A crucial review. *Renew. Sust. Energ. Rev.*, 4(2):157–175, 2000.

[15] Aaron Carroll and Gernot Heiser. An analysis of power consumption in a smartphone. In *USENIX annual technical conference*, volume 14. Boston, MA, 2010.

[16] M Stanley Whittingham. Lithium batteries and cathode materials. *Chem. Rev.*, 104(10):4271–4302, 2004.

[17] John B Goodenough. Cathode materials: A personal perspective. *J. Power Sources*, 174(2):996–1000, 2007.

[18] Michel Armand and J-M Tarascon. Building better batteries. *Nature*, 451(7179):652–657, 2008.

[19] John B Goodenough and Youngsik Kim. Challenges for rechargeable Li batteries. *Chem. Mater.*, 22(3):587–603, 2009.

[20] M Stanley Whittingham. Electrical energy storage and intercalation chemistry. *Science*, 192(4244):1126–1127, 1976.

[21] K Mizushima, PC Jones, PJ Wiseman, and JB Goodenough. Li_xCoO_2 (0< x<-1): A new cathode material for batteries of high energy density. *Mater. Res. Bull.*, 15(6):783–789, 1980.

[22] Kisuk Kang, Ying Shirley Meng, Julien Bréger, Clare P Grey, and Gerbrand Ceder. Electrodes with high power and high capacity for rechargeable lithium batteries. *Science*, 311(5763):977–980, 2006.

[23] Michael M Thackeray, Sun-Ho Kang, Christopher S Johnson, John T Vaughey, Roy Benedek, and SA Hackney. Li_2MnO_3-stabilized $LiMO_2$ (M= Mn, Ni, Co) electrodes for lithium-ion batteries. *J. Mater. Chem.*, 17(30):3112–3125, 2007.

[24] Byoungwoo Kang and Gerbrand Ceder. Battery materials for ultrafast charging and discharging. *Nature*, 458(7235):190–193, 2009.

[25] David J Bradwell, Hojong Kim, Aislinn HC Sirk, and Donald R Sadoway. Magnesium–antimony liquid metal battery for stationary energy storage. *J. Am. Chem. Soc.*, 134(4):1895–1897, 2012.

[26] Kangli Wang, Kai Jiang, Brice Chung, Takanari Ouchi, Paul J Burke, Dane A Boysen, David J Bradwell, Hojong Kim, Ulrich Muecke, and Donald R Sadoway. Lithium-antimony-lead liquid metal battery for grid-level energy storage. *Nature*, 514(7522):348–350, 2014.

[27] G Girishkumar, B McCloskey, AC Luntz, S Swanson, and W Wilcke. Lithium-air battery: promise and challenges. *J. Phys. Chem. Lett.*, 1(14):2193–2203, 2010.

[28] Hun-Gi Jung, Jusef Hassoun, Jin-Bum Park, Yang-Kook Sun, and Bruno Scrosati. An improved high-performance lithium–air battery. *Nat. Chem.*, 4(7):579–585, 2012.

[29] Wei Wang, Qingtao Luo, Bin Li, Xiaoliang Wei, Liyu Li, and Zhenguo Yang. Recent progress in redox flow battery research and development. *Adv. Funct. Mater.*, 23(8):970–986, 2013.

[30] Yanguang Li and Hongjie Dai. Recent advances in zinc–air batteries. *Chem. Soc. Rev.*, 43(15):5257–5275, 2014.

[31] Brian L. Ellis and Linda F. Nazar. Sodium and sodium-ion energy storage batteries. *Curr. Opin. Solid State Mater. Sci.*, 16(4):168 – 177, 2012.

[32] Sung-Wook Kim, Dong-Hwa Seo, Xiaohua Ma, Gerbrand Ceder, and Kisuk Kang. Electrode materials for rechargeable sodium-ion batteries: Potential alternatives to current lithium-ion batteries. *Adv. Energy Mater.*, 2(7):710–721, 2012.

[33] JF Whitacre, A Tevar, and S Sharma. $Na_4Mn_9O_{18}$ as a positive electrode material for an aqueous electrolyte sodium-ion energy storage device. *Electrochem. Commun.*, 12(3):463–466, 2010.

[34] JF Whitacre, T Wiley, S Shanbhag, Y Wenzhuo, A Mohamed, SE Chun, E Weber, D Blackwood, E Lynch-Bell, J Gulakowski, et al. An aqueous electrolyte, sodium ion functional, large format energy storage device for stationary applications. *J. Power Sources*, 213:255–264, 2012.

[35] Mauro Pasta, Colin D Wessells, Robert A Huggins, and Yi Cui. A high-rate and long cycle life aqueous electrolyte battery for grid-scale energy storage. *Nature Communications*, 3:1149, 2012.

[36] Huilin Pan, Yong-Sheng Hu, and Liquan Chen. Room-temperature stationary sodium-ion batteries for large-scale electric energy storage. *Energy Environ. Sci.*, 6(8):2338–2360, 2013.

[37] Weixin Song, Xiaobo Ji, Yirong Zhu, Hanjun Zhu, Fangqian Li, Jun Chen, Fang Lu, Yinpeng Yao, Craig Banks, et al. Aqueous sodium-ion battery using a $Na_3V_2(PO_4)_3$ electrode. *Chem. Electro. Chem.*, 1(5):871–876, 2014.

[38] Haifeng Wang, Young-Il Jang, Biying Huang, Donald R Sadoway, and Yet-Ming Chiang. TEM study of electrochemical cycling-induced damage and disorder in $LiCoO_2$ cathodes for rechargeable lithium batteries. *J. Electrochem. Soc.*, 146(2):473–480, 1999.

[39] Tsutomu Ohzuku and Yoshinari Makimura. Layered lithium insertion material of $LiNi_{1/2}Mn_{1/2}O_2$: A possible alternative to $LiCoO_2$ for advanced lithium-ion batteries. *Chem. Lett.*, (8):744–745, 2001.

[40] Young-Il Jang, Biying Huang, Haifeng Wang, Donald R Sadoway, Gerbrand Ceder, Yet-Ming Chiang, Hui Liu, and Hirokazu Tamura. $LiAl_yCo_{1-y}O_2$ ($R\bar{3}m$) intercalation cathode for rechargeable lithium batteries. *J. Electrochem. Soc.*, 146(3):862–868, 1999.

[41] Seung-Taek Myung, Naoaki Kumagai, Shinichi Komaba, and Hoon-Taek Chung. Effects of al doping on the microstructure of $LiCoO_2$ cathode materials. *Solid State Ionics*, 139(1):47–56, 2001.

[42] A. K. Padhi, K. S. Nanjundaswamy, and J. B. D. Goodenough. Phospho-olivines as positive-electrode materials for rechargeable lithium batteries. *J. Electrochem. Soc.*, 144(4):1188–1194, 1997.

[43] Shinichi Komaba, Naoaki Yabuuchi, Tetsuri Nakayama, Atsushi Ogata, Toru Ishikawa, and Izumi Nakai. Study on the reversible electrode reaction of $Na_{1-x}Ni_{0.5}Mn_{0.5}O_2$ for a rechargeable sodium-ion battery. *Inorg. Chem.*, 51(11):6211–6220, 2012.

[44] Donghan Kim, Eungje Lee, Michael Slater, Wenquan Lu, Shawn Rood, and Christopher S Johnson. Layered $Na[Ni_{1/3}Fe_{1/3}Mn_{1/3}]O_2$ cathodes for Na-ion battery application. *Electrochem. Commun.*, 18:66–69, 2012.

[45] Naoaki Yabuuchi, Masataka Kajiyama, Junichi Iwatate, Heisuke Nishikawa, Shuji Hitomi, Ryoichi Okuyama, Ryo Usui, Yasuhiro Yamada, and Shinichi Komaba. P2-type $Na_x[Fe_{1/2}Mn_{1/2}]O_2$ made from earth-abundant elements for rechargeable Na batteries. *Nat. Mater.*, 11(6):512–517, 2012.

[46] Xin Li, Di Wu, Yong-Ning Zhou, Lei Liu, Xiao-Qing Yang, and Gerbrand Ceder. O3-type $Na(Mn_{0.25}Fe_{0.25}Co_{0.25}Ni_{0.25})O_2$: A quaternary layered cathode compound for rechargeable Na-ion batteries. *Electrochem. Commun.*, 49:51 – 54, 2014.

[47] Zelang Jian, Liang Zhao, Huilin Pan, Yong-Sheng Hu, Hong Li, Wen Chen, and Liquan Chen. Carbon coated $Na_3V_2(PO_4)_3$ as novel electrode material for sodium ion batteries. *Electrochem. Commun.*, 14(1):86–89, 2012.

[48] Zelang Jian, Wenze Han, Xia Lu, Huaixin Yang, Yong-Sheng Hu, Jing Zhou, Zhibin Zhou, Jianqi Li, Wen Chen, Dongfeng Chen, et al. Superior electrochemical performance and storage mechanism of $Na_3V_2(PO_4)_3$ cathode for room-temperature sodium-ion batteries. *Adv. Energy Mater.*, 3(2):156–160, 2013.

[49] R. A. Shakoor, Dong-Hwa Seo, Hyungsub Kim, Young-Uk Park, Jongsoon Kim, Sung-Wook Kim, Hyeokjo Gwon, Seongsu Lee, and Kisuk Kang. A combined first principles and experimental study on $Na_3V_2(PO_4)_2F_3$ for rechargeable Na batteries. *J. Mater. Chem.*, 22:20535–20541, 2012.

[50] Kuniko Chihara, Ayuko Kitajou, Irina D. Gocheva, Shigeto Okada, and Junichi Yamaki. Cathode properties of $Na_3M_2(PO_4)_2F_3$ [M = Ti, Fe, V] for sodium-ion batteries. *J. Power Sources*, 227(0):80 – 85, 2013.

[51] Paula Serras, Veronica Palomares, Aintzane Goni, Izaskun Gil de Muro, Pierre Kubiak, Luis Lezama, and Teofilo Rojo. High voltage cathode materials for Na-ion batteries of general formula $Na_3V_2O_{2x}(PO_4)_2F_{3-2x}$. *J. Mater. Chem.*, 22:22301–22308, 2012.

[52] Vinodkumar Etacheri, Rotem Marom, Ran Elazari, Gregory Salitra, and Doron Aurbach. Challenges in the development of advanced Li-ion batteries: a review. *Energy Environ. Sci.*, 4(9):3243–3262, 2011.

[53] Candace K Chan, Hailin Peng, Gao Liu, Kevin McIlwrath, Xiao Feng Zhang, Robert A Huggins, and Yi Cui. High-performance lithium battery anodes using silicon nanowires. *Nat. Nanotechnol.*, 3(1):31–35, 2008.

[54] See-How Ng, Jiazhao Wang, David Wexler, Konstantin Konstantinov, Zai-Ping Guo, and Hua-Kun Liu. Highly reversible lithium storage in spheroidal carbon-coated silicon nanocomposites as anodes for lithium-ion batteries. *Angew. Chem. Int. Edit.*, 45(41):6896–6899, 2006.

[55] Li-Feng Cui, Liangbing Hu, Jang Wook Choi, and Yi Cui. Light-weight free-standing carbon nanotube-silicon films for anodes of lithium ion batteries. *ACS Nano*, 4(7):3671–3678, 2010.

[56] Shinichi Komaba, Wataru Murata, Toru Ishikawa, Naoaki Yabuuchi, Tomoaki Ozeki, Tetsuri Nakayama, Atsushi Ogata, Kazuma Gotoh, and Kazuya Fujiwara. Electrochemical Na insertion and solid electrolyte interphase for hard-carbon electrodes and application to Na-ion batteries. *Adv. Funct. Mater.*, 21(20):3859–3867, 2011.

[57] DA Stevens and JR Dahn. High capacity anode materials for rechargeable sodium-ion batteries. *J. Electrochem. Soc.*, 147(4):1271–1273, 2000.

[58] Ashish Rudola, Kuppan Saravanan, Chad W Mason, and Palani Balaya. $Na_2Ti_3O_7$: an intercalation based anode for sodium-ion battery applications. *J. Mater. Chem. A*, 1(7):2653–2662, 2013.

[59] Yunhua Xu, Yujie Zhu, Yihang Liu, and Chunsheng Wang. Electrochemical performance of porous carbon/tin composite anodes for sodium-ion and lithium-ion batteries. *Adv. Energy Mater.*, 3(1):128–133, 2013.

[60] Gholam-Abbas Nazri and Gianfranco Pistoia. *Lithium batteries: science and technology*. Springer Science & Business Media, 2008.

[61] Vanchiappan Aravindan, Joe Gnanaraj, Srinivasan Madhavi, and Hua-Kun Liu. Lithium-ion conducting electrolyte salts for lithium batteries. *Chem. Eur. J.*, 17(51):14326–14346, 2011.

[62] Michael D. Slater, Donghan Kim, Eungje Lee, and Christopher S. Johnson. Sodium-ion batteries. *Adv. Funct. Mater.*, 23(8):947–958, 2013.

[63] Doron Aurbach. *Nonaqueous electrochemistry*. CRC Press, 1999.

[64] D Guyomard and JM Tarascon. Li metal-free rechargeable $LiMn_2O_4$/Carbon cells: Their understanding and optimization. *J. Electrochem. Soc.*, 139(4):937–948, 1992.

[65] Akitoshi Hayashi, Kousuke Noi, Atsushi Sakuda, and Masahiro Tatsumisago. Superionic glass-ceramic electrolytes for room-temperature rechargeable sodium batteries. *Nature Communications*, 3:856, 2012.

[66] Yifei Mo, Shyue Ping Ong, and Gerbrand Ceder. First principles study of the $Li_{10}GeP_2S_{12}$ lithium super ionic conductor material. *Chem. Mater.*, 24(1):15–17, 2011.

[67] Michel Armand, Frank Endres, Douglas R MacFarlane, Hiroyuki Ohno, and Bruno Scrosati. Ionic-liquid materials for the electrochemical challenges of the future. *Nat. Mater.*, 8(8):621–629, 2009.

[68] Béatrice Garcia, Serge Lavallée, Gérald Perron, Christophe Michot, and Michel Armand. Room temperature molten salts as lithium battery electrolyte. *Electrochem. Acta*, 49(26):4583–4588, 2004.

[69] A. J. Smith, J. C. Burns, S. Trussler, and J. R. Dahn. Precision measurements of the coulombic efficiency of lithium-ion batteries and of electrode materials for lithium-ion batteries. *J. Electrochem. Soc.*, 157(2):A196–A202, 2010.

[70] Jianlin Li, Claus Daniel, and David Wood. Materials processing for lithium-ion batteries. *J. Power Sources*, 196(5):2452–2460, 2011.

[71] Huiqiao Li and Haoshen Zhou. Enhancing the performances of Li-ion batteries by carbon-coating: present and future. *Chem. Commun.*, 48(9):1201–1217, 2012.

[72] Sung-Yoon Chung and Yet-Ming Chiang. Microscale measurements of the electrical conductivity of doped $LiFePO_4$. *Electrochem. Solid State Lett.*, 6(12):A278–A281, 2003.

[73] Feng Wang, Rosa Robert, Natasha A Chernova, Nathalie Pereira, Fredrick Omenya, Fadwa Badway, Xiao Hua, Michael Ruotolo, Ruigang Zhang, Lijun Wu, et al. Conversion reaction mechanisms in lithium ion batteries: study of the binary metal fluoride electrodes. *J. Am. Chem. Soc.*, 133(46):18828–18836, 2011.

[74] Hyungsub Kim, Inchul Park, Dong-Hwa Seo, Seongsu Lee, Sung-Wook Kim, Woo Jun Kwon, Young-Uk Park, Chul Sung Kim, Seokwoo Jeon, and Kisuk Kang. New iron-based mixed-polyanion cathodes for lithium and sodium rechargeable batteries: combined first principles calculations and experimental study. *J. Am. Chem. Soc.*, 134(25):10369–10372, 2012.

[75] Guangyuan Zheng, Seok Woo Lee, Zheng Liang, Hyun-Wook Lee, Kai Yan, Hongbin Yao, Haotian Wang, Weiyang Li, Steven Chu, and Yi Cui. Interconnected hollow carbon nanospheres for stable lithium metal anodes. *Nat. Nanotechnol.*, 9(8):618–623, 2014.

[76] Yi Cui, Guangyuan Zheng, Steven Chu, and Kai Yan. Interfacial engineering for stable lithium metal anodes, January 2016. US Patent 20,160,013,462.

[77] L Wang, T Maxisch, and G Ceder. A first-principles approach to studying the thermal stability of oxide cathode materials. *Chem. Mater.*, 19(3):543–552, 2007.

[78] Shyue Ping Ong, Anubhav Jain, Geoffroy Hautier, Byoungwoo Kang, and Gerbrand Ceder. Thermal stabilities of delithiated olivine MPO_4 (M = Fe, Mn) cathodes investigated using first principles calculations. *Electrochem. Commun.*, 12(3):427–430, 2010.

[79] Xin Xia and JR Dahn. $NaCrO_2$ is a fundamentally safe positive electrode material for sodium-ion batteries with liquid electrolytes. *Electrochem. Solid State Lett.*, 15(1):A1–A4, 2011.

[80] Brian L Ellis, TN Ramesh, Linda JM Davis, Gillian R Goward, and Linda F Nazar. Structure and electrochemistry of two-electron redox couples in lithium metal fluorophosphates based on the tavorite structure. *Chem. Mater.*, 23(23):5138–5148, 2011.

[81] Zelang Jian, Yang Sun, and Xiulei Ji. A new low-voltage plateau of $Na_3V_2(PO_4)_3$ as an anode for Na-ion batteries. *Chem. Commun.*, 51(29):6381–6383, 2015.

[82] Jeffrey W Fergus. Recent developments in cathode materials for lithium ion batteries. *J. Power Sources*, 195(4):939–954, 2010.

[83] Hajime Arai, Shigeto Okada, Yoji Sakurai, and Jun-ichi Yamaki. Cathode performance and voltage estimation of metal trihalides. *J. Power Sources*, 68(2):716–719, 1997.

[84] F Badway, F Cosandey, N Pereira, and GG Amatucci. Carbon metal fluoride nanocomposites high-capacity reversible metal fluoride conversion materials as rechargeable positive electrodes for li batteries. *J. Electrochem. Soc.*, 150(10):A1318–A1327, 2003.

[85] F Badway, N Pereira, F Cosandey, and GG Amatucci. Carbon-metal fluoride nanocomposites structure and electrochemistry of FeF_3:C. *J. Electrochem. Soc.*, 150(9):A1209–A1218, 2003.

[86] Glenn G Amatucci and Nathalie Pereira. Fluoride based electrode materials for advanced energy storage devices. *J. Fluorine Chem.*, 128(4):243–262, 2007.

[87] Candace K Chan, Xiao Feng Zhang, and Yi Cui. High capacity Li ion battery anodes using Ge nanowires. *Nano Lett.*, 8(1):307–309, 2008.

[88] Guanglei Cui, Lin Gu, Linjie Zhi, N Kaskhedikar, Peter A van Aken, Klaus Müllen, and Joachim Maier. A germanium–carbon nanocomposite material for lithium batteries. *Adv. Mater.*, 20(16):3079–3083, 2008.

[89] Mi-Hee Park, Min Gyu Kim, Jaebum Joo, Kitae Kim, Jeyoung Kim, Soonho Ahn, Yi Cui, and Jaephil Cho. Silicon nanotube battery anodes. *Nano Lett.*, 9(11):3844–3847, 2009.

[90] Jordi Cabana, Laure Monconduit, Dominique Larcher, and M Rosa Palacin. Beyond intercalation-based Li-ion batteries: The state of the art and challenges of electrode materials reacting through conversion reactions. *Adv. Mater.*, 22(35):E170–E192, 2010.

[91] S Kikkawa, S Miyazaki, and M Koizumi. Electrochemical aspects of the deintercalation of layered AMO_2 compounds. *J. Power Sources*, 14(1-3):231–234, 1985.

[92] C Delmas, A Nadiri, and JL Soubeyroux. The NASICON-type titanium phosphates $ATi_2(PO_4)_3$ (A= Li, Na) as electrode materials. *Solid State Ionics*, 28:419–423, 1988.

[93] K West, B Zachau-Christiansen, T Jacobsen, and S Skaarup. Sodium insertion in vanadium oxides. *Solid State Ionics*, 28:1128–1131, 1988.

[94] C Delmas. Alkali metal intercalation in layered oxides. *Mater. Sci. Eng. B*, 3(1-2):97–101, 1989.

[95] Romain Berthelot, D Carlier, and Claude Delmas. Electrochemical investigation of the P2–Na_xCoO_2 phase diagram. *Nat. Mater.*, 10(1):74–80, 2011.

[96] Marie Guignard, Christophe Didier, Jacques Darriet, Pierre Bordet, Erik Elkaïm, and Claude Delmas. P2-Na_xVO_2 system as electrodes for batteries and electron-correlated materials. *Nat. Mater.*, 12(1):74–80, 2013.

[97] Di Wu, Xin Li, Bo Xu, Nancy Twu, Lei Liu, and Gerbrand Ceder. $NaTiO_2$: a layered anode material for sodium-ion batteries. *Energy Environ. Sci.*, 8(1):195–202, 2015.

[98] Christophe Didier, Marie Guignard, Cathy Denage, Olivier Szajwaj, Seishiro Ito, Ismaël Saadoune, Jacques Darriet, and Claude Delmas. Electrochemical Na-deintercalation from $NaVO_2$. *Electrochem. Solid State Lett.*, 14(5):A75–A78, 2011.

[99] Shinichi Komaba, Tetsuri Nakayama, Atsushi Ogata, Takaya Shimizu, Chikara Takei, S Takada, A Hokura, and I Nakai. Electrochemically reversible sodium intercalation of layered $NaNi_{0.5}Mn_{0.5}O_2$ and $NaCrO_2$. *ECS Trans.*, 16(42):43–55, 2009.

[100] Xiaohua Ma, Hailong Chen, and Gerbrand Ceder. Electrochemical properties of monoclinic $NaMnO_2$. *J. Electrochem. Soc.*, 158(12):A1307–A1312, 2011.

[101] Naoaki Yabuuchi, Hiroaki Yoshida, and Shinichi Komaba. Crystal structures and electrode performance of α-$NaFeO_2$ for rechargeable sodium batteries. *Electrochemistry*, 80(10):716–719, 2012.

[102] Plousia Vassilaras, Xiaohua Ma, Xin Li, and Gerbrand Ceder. Electrochemical properties of monoclinic $NaNiO_2$. *J. Electrochem. Soc.*, 160(2):A207–A211, 2013.

[103] Alexandra J Toumar, Shyue Ping Ong, William Davidson Richards, Stephen Dacek, and Gerbrand Ceder. Vacancy ordering in O3-type layered metal oxide sodium-ion battery cathodes. *Phys. Rev. App.*, 4(6):064002, 2015.

[104] JJ Ding, YN Zhou, Q Sun, XQ Yu, XQ Yang, and ZW Fu. Electrochemical properties of P2–phase $Na_{0.74}CoO_2$ compounds as cathode material for rechargeable sodium-ion batteries. *Electrochem. Acta*, 87:388–393, 2013.

[105] David Hamani, Mohamed Ati, Jean-Marie Tarascon, and Patrick Rozier. Na_xVO_2 as possible electrode for Na-ion batteries. *Electrochem. Commun.*, 13(9):938–941, 2011.

[106] Gosuke Oyama, Shin-ichi Nishimura, Yuya Suzuki, Masashi Okubo, and Atsuo Yamada. Off-stoichiometry in alluaudite-type sodium iron sulfate $Na_{2+2x}Fe_{2-x}(SO_4)_3$ as an advanced sodium battery cathode material. *Chem. Electro. Chem.*, 2(7):1019–1023, 2015.

[107] Yu Meng, Tiantian Yu, Sen Zhang, and Chao Deng. Top-down synthesis of muscle-inspired alluaudite $Na_{2+2x}Fe_{2-x}(SO_4)_3$/SWNT spindle as a high-rate and high-potential cathode for sodium-ion batteries. *J. Mater. Chem. A*, 4:1624–1631, 2016.

[108] Prabeer Barpanda, Gosuke Oyama, Chris D Ling, and Atsuo Yamada. Kröhnkite-type $Na_2Fe(SO_4)_2 \cdot 2H_2O$ as a novel 3.25 V insertion compound for Na-ion batteries. *Chem. Mater.*, 26(3):1297–1299, 2014.

[109] MY Saıdi, J Barker, H Huang, JL Swoyer, and G Adamson. Performance characteristics of lithium vanadium phosphate as a cathode material for lithium-ion batteries. *J. Power Sources*, 119:266–272, 2003.

[110] BL Ellis, WRM Makahnouk, Y Makimura, K Toghill, and LF Nazar. A multifunctional 3.5 V iron-based phosphate cathode for rechargeable batteries. *Nat. Mater.*, 6(10):749–753, 2007.

[111] Shin-ichi Nishimura, Megumi Nakamura, Ryuichi Natsui, and Atsuo Yamada. New lithium iron pyrophosphate as 3.5 V class cathode material for lithium ion battery. *J. Am. Chem. Soc.*, 132(39):13596–13597, 2010.

[112] Prabeer Barpanda, Tian Ye, Maxim Avdeev, Sai-Cheong Chung, and Atsuo Yamada. A new polymorph of $Na_2MnP_2O_7$ as a 3.6 V cathode material for sodium-ion batteries. *J. Mater. Chem. A*, 1(13):4194–4197, 2013.

[113] Prabeer Barpanda, Gosuke Oyama, Shin-ichi Nishimura, Sai-Cheong Chung, and Atsuo Yamada. A 3.8 V earth-abundant sodium battery electrode. *Nature Communications*, 5, 2014.

[114] Ian Matts, Hailong Chen, and Gerbrand Ceder. Electrochemical properties of $Li_3Fe_{0.2}Mn_{0.8}CO_3PO_4$ as a Li-ion battery cathode. *ECS Electrochem. Lett.*, 2(8):A81–A83, 2013.

[115] Chuanlong Wang, Monica Sawicki, Satya Emani, Caihong Liu, and Leon L Shaw. $Na_3MnCO_3PO_4$-a high capacity, multi-electron transfer redox cathode material for sodium ion batteries. *Electrochem. Acta*, 161:322–328, 2015.

[116] Atsuo Yamada, Nobuyuki Iwane, Yu Harada, Shin-ichi Nishimura, Yukinori Koyama, and Isao Tanaka. Lithium iron borates as high-capacity battery electrodes. *Adv. Mater.*, 22(32):3583–3587, 2010.

[117] Shigeto Okada, Shoichiro Sawa, Minato Egashira, Jun-ichi Yamaki, Mitsuharu Tabuchi, Hiroyuki Kageyama, Tokuzo Konishi, and Akira Yoshino. Cathode properties of phospho-olivine $LiMPO_4$ for lithium secondary batteries. *J. Power Sources*, 97:430–432, 2001.

[118] Hui Zhou, Shailesh Upreti, Natasha A Chernova, Geoffroy Hautier, Gerbrand Ceder, and M Stanley Whittingham. Iron and manganese pyrophosphates as cathodes for lithium-ion batteries. *Chem. Mater.*, 23(2):293–300, 2010.

[119] R Dugas, B Zhang, P Rozier, and JM Tarascon. Optimization of Na-ion battery systems based on polyanionic or layered positive electrodes and carbon anodes. *J. Electrochem. Soc.*, 163(6):A867–A874, 2016.

[120] Tim Mueller, Geoffroy Hautier, Anubhav Jain, and Gerbrand Ceder. Evaluation of tavorite-structured cathode materials for lithium-ion batteries using high-throughput computing. *Chem. Mater.*, 23(17):3854–3862, 2011.

[121] Geoffroy Hautier, Chris Fischer, Virginie Ehrlacher, Anubhav Jain, and Gerbrand Ceder. Data mined ionic substitutions for the discovery of new compounds. *Inorg. Chem.*, 50(2):656–663, 2010.

[122] Jae Chul Kim, Charles J. Moore, Byoungwoo Kang, Geoffroy Hautier, Anubhav Jain, and Gerbrand Ceder. Synthesis and electrochemical properties of monoclinic $LiMnBO_3$ as a Li intercalation material. *J. Electrochem. Soc.*, 158(3):A309–A315, 2011.

[123] Geoffroy Hautier, Anubhav Jain, Shyue Ping Ong, Byoungwoo Kang, Charles Moore, Robert Doe, and Gerbrand Ceder. Phosphates as lithium-ion battery cathodes: an evaluation based on high-throughput ab initio calculations. *Chem. Mater.*, 23(15):3495–3508, 2011.

[124] G Ceder, Y-M Chiang, DR Sadoway, MK Aydinol, Y-I Jang, and B Huang. Identification of cathode materials for lithium batteries guided by first-principles calculations. *Nature*, 392(6677):694–696, 1998.

[125] Jinhyuk Lee, Alexander Urban, Xin Li, Dong Su, Geoffroy Hautier, and Gerbrand Ceder. Unlocking the potential of cation-disordered oxides for rechargeable lithium batteries. *Science*, 343(6170):519–522, 2014.

[126] Alexander Urban, Jinhyuk Lee, and Gerbrand Ceder. The configurational space of rocksalt-type oxides for high-capacity lithium battery electrodes. *Adv. Energy Mater.*, 4(13), 2014.

[127] Nancy Twu, Xin Li, Alexander Urban, Mahalingam Balasubramanian, Jinhyuk Lee, Lei Liu, and Gerbrand Ceder. Designing new lithium-excess cathode materials from percolation theory: Nanohighways in $Li_xNi_{2-4x/3}Sb_{x/3}O_2$. *Nano Lett.*, 15(1):596–602, 2014.

[128] Rui Wang, Xin Li, Lei Liu, Jinhyuk Lee, Dong-Hwa Seo, Shou-Hang Bo, Alexander Urban, and Gerbrand Ceder. A disordered rock-salt Li-excess cathode material with high capacity and substantial oxygen redox activity: $Li_{1.25}Nb_{0.25}Mn_{0.5}O_2$. *Electrochem. Commun.*, 60:70–73, 2015.

[129] Jan N Reimers and JR Dahn. Electrochemical and in situ x-ray diffraction studies of lithium intercalation in Li_xCoO_2. *J. Electrochem. Soc.*, 139(8):2091–2097, 1992.

[130] Nicolas Tran, Laurence Croguennec, Michel Ménétrier, François Weill, Ph Biensan, C Jordy, and Claude Delmas. Mechanisms associated with the "plateau" observed at high voltage for the overlithiated $Li_{1.12}(Ni_{0.425}Mn_{0.425}Co_{0.15})_{0.88}O_2$ system. *Chem. Mater.*, 20(15):4815–4825, 2008.

[131] Bo Xu, Christopher R Fell, Miaofang Chi, and Ying Shirley Meng. Identifying surface structural changes in layered Li-excess nickel manganese oxides in high voltage lithium ion batteries: A joint experimental and theoretical study. *Energy Environ. Sci.*, 4(6):2223–2233, 2011.

[132] M Sathiya, Artem M Abakumov, D Foix, G Rousse, K Ramesha, M Saubanère, ML Doublet, H Vezin, CP Laisa, AS Prakash, et al. Origin of voltage decay in high-capacity layered oxide electrodes. *Nat. Mater.*, 14(2):230–238, 2015.

[133] Jianming Zheng, Pinghong Xu, Meng Gu, Jie Xiao, Nigel D Browning, Pengfei Yan, Chongmin Wang, and Ji-Guang Zhang. Structural and chemical evolution of Li-and Mn-rich layered cathode material. *Chem. Mater.*, 27(4):1381–1390, 2015.

[134] Kisuk Kang and Gerbrand Ceder. Factors that affect Li mobility in layered lithium transition metal oxides. *Phys. Rev. B*, 74(9):094105, 2006.

[135] Allen J Bard and Larry R Faulkner. *Electrochemical methods: fundamentals and applications*, volume 2. Wiley New York, 1980.

[136] Maria Strømme Mattsson. Li insertion into WO_3: introduction of a new electrochemical analysis method and comparison with impedance spectroscopy and the galvanostatic intermittent titration technique. *Solid State Ionics*, 131(3):261–273, 2000.

[137] John Reed and Gerbrand Ceder. Role of electronic structure in the susceptibility of metastable transition-metal oxide structures to transformation. *Chem. Rev.*, 104(10):4513–4534, 2004.

[138] J Reed and G Ceder. Charge, potential, and phase stability of layered $Li(Ni_{0.5}Mn_{0.5})O_2$. *Electrochem. Solid State Lett.*, 5(7):A145–A148, 2002.

[139] Nadir Recham, Loic Dupont, Matthieu Courty, Karim Djellab, Dominique Larcher, Michel Armand, and J-M Tarascon. Ionothermal synthesis of tailor-made $LiFePO_4$ powders for Li-ion battery applications. *Chem. Mater.*, 21(6):1096–1107, 2009.

[140] Peter R Tremaine and Caibin Xiao. Enthalpies of formation and heat capacity functions for maricite, $NaFePO_4$, and sodium iron (III) hydroxy phosphate, $Na_3Fe(PO_4)_2{\cdot}(Na_{4/3}H_{2/3}O)$. *J. Chem. Thermodyn.*, 31(10):1307–1320, 1999.

[141] Wei Tong, Guan-Guang Xia, Zheng-Rong Tian, Jia Liu, Jun Cai, Steven L Suib, and Jonathan C Hanson. Hydrothermal synthesis and characterization of sodium manganese oxo-phosphate $Na_2Mn_2O\ (PO_4)_2{\cdot}H_2O$. *Chem. Mater.*, 14(2):615–620, 2002.

[142] Prabeer Barpanda, Jean-Noël Chotard, Nadir Recham, Charles Delacourt, Mohamed Ati, Loic Dupont, Michel Armand, and Jean-Marie Tarascon. Structural, transport, and electrochemical investigation of novel $AMSO_4F$ (A= Na, Li; M= Fe, Co, Ni, Mn) metal fluorosulphates prepared using low temperature synthesis routes. *Inorg. Chem.*, 49(16):7401–7413, 2010.

[143] F Sanz, C Parada, JM Rojo, and C Ruiz-Valero. Synthesis, structural characterization, magnetic properties, and ionic conductivity of $Na_4M_3^{II}(PO_4)_2(P_2O_7)$($M^{II}$= Mn, Co, Ni). *Chem. Mater.*, 13(4):1334–1340, 2001.

[144] J Gopalakrishnan and K Kasthuri Rangan. Vanadium phosphate ($V_2(PO_4)_3$): a novel NASICON-type vanadium phosphate synthesized by oxidative deintercalation of sodium from sodium vanadium phosphate. *Chem. Mater.*, 4(4):745–747, 1992.

[145] K Zaghib, J Trottier, P Hovington, F Brochu, A Guerfi, A Mauger, and CM Julien. Characterization of Na-based phosphate as electrode materials for electrochemical cells. *J. Power Sources*, 196(22):9612–9617, 2011.

[146] Orville Frank Tuttle. A new hydrothermal quenching apparatus. *Am. J. Sci*, 246(10):628–635, 1948.

[147] IM Kötschau and JR Dahn. In situ x-ray study of $LiMnO_2$. *J. Electrochem. Soc.*, 145(8):2672–2677, 1998.

[148] Rahul Malik, Fei Zhou, and Gerbrand Ceder. Kinetics of non-equilibrium lithium incorporation in $LiFePO_4$. *Nat. Mater.*, 10(8):587–590, 2011.

[149] Pierre Gibot, Montse Casas-Cabanas, Lydia Laffont, Stephane Levasseur, Philippe Carlach, Stéphane Hamelet, Jean-Marie Tarascon, and Christian Masquelier. Room-temperature single-phase Li insertion/extraction in nanoscale Li_xFePO_4. *Nat. Mater.*, 7(9):741–747, 2008.

[150] Fangyi Cheng and Jun Chen. Transition metal vanadium oxides and vanadate materials for lithium batteries. *J. Mater. Chem.*, 21(27):9841–9848, 2011.

[151] Katherine C Hess, Jay F Whitacre, and Shawn Litster. In situ measurements of potential, current and charging current across an EDL capacitance anode for an aqueous sodium hybrid battery. *J. Electrochem. Soc.*, 159(8):A1351–A1359, 2012.

[152] M Morcrette, Y Chabre, G Vaughan, G Amatucci, J-B Leriche, S Patoux, C Masquelier, and JM Tarascon. In situ x-ray diffraction techniques as a powerful tool to study battery electrode materials. *Electrochem. Acta*, 47(19):3137–3149, 2002.

[153] Nadir Recham, Jean-Noel Chotard, Loic Dupont, Charles Delacourt, Wesley Walker, Michel Armand, and Jean-Marie Tarascon. A 3.6 V lithium-based fluorosulphate insertion positive electrode for lithium-ion batteries. *Nat. Mater.*, 9(1):68–74, 2010.

[154] John B. Goodenough. Evolution of strategies for modern rechargeable batteries. *Acc. Chem. Res.*, 46(5):1053–1061, 2013. PMID: 22746097.

[155] Anubhav Jain, Geoffroy Hautier, Charles Moore, Byoungwoo Kang, Jinhyuk Lee, Hailong Chen, Nancy Twu, and Gerbrand Ceder. A computational investigation of $Li_9M_3(P_2O_7)_3(PO_4)_2$ (M = V, Mo) as cathodes for Li-ion batteries. *J. Electrochem. Soc.*, 159(5):A622–A633, 2012.

[156] Atsuo Yamada, Yoshihiro Kudo, and Kuang-Yu Liu. Phase diagram of $Li_x(Mn_yFe_{1>y})PO_4$ ($0<x,y<1$). *J. Electrochem. Soc.*, 148(10):A1153–A1158, 2001.

[157] J Yao, S Bewlay, K Konstantionv, VA Drozd, RS Liu, XL Wang, HK Liu, and GX Wang. Characterisation of olivine-type $LiMn_xFe_{1-x}PO_4$ cathode materials. *J. Alloy. Compd.*, 425(1):362–366, 2006.

[158] Haisheng Fang, Enrui Dai, Bin Yang, Yaochun Yao, and Wenhui Ma. $LiMn_{0.8}Fe_{0.19}Mg_{0.01}PO_4$/C as a high performance cathode material for lithium ion batteries. *J. Power Sources*, 204:193–196, 2012.

[159] A Robert Armstrong and Peter G Bruce. Synthesis of layered $LiMnO_2$ as an electrode for rechargeable lithium batteries. *Nature*, 381(6582):499–500, 1996.

[160] C. H. Mi, X. B. Zhao, G. S. Cao, and J. P. Tu. In situ synthesis and properties of carbon-coated $LiFePO_4$ as Li-ion battery cathodes. *J. Electrochem. Soc.*, 152(3):A483–A487, 2005.

[161] H. Huang, S.-C. Yin, and L. F. Nazar. Approaching theoretical capacity of $LiFePO_4$ at room temperature at high rates. *Electrochem. Solid State Lett.*, 4(10):A170–A172, 2001.

[162] K Amine, H Yasuda, and M Yamachi. β-FeOOH, a new positive electrode material for lithium secondary batteries. *J. Power Sources*, 81:221–223, 1999.

[163] Rahul Malik, Fei Zhou, Gerbrand Ceder, et al. Phase diagram and electrochemical properties of mixed olivines from first-principles calculations. *Phys. Rev. B*, 79(21):214201, 2009.

[164] Hailiang Wang, Li-Feng Cui, Yuan Yang, Hernan Sanchez Casalongue, Joshua Tucker Robinson, Yongye Liang, Yi Cui, and Hongjie Dai. Mn_3O_4-graphene hybrid as a high-capacity anode material for lithium ion batteries. *J. Am. Chem. Soc.*, 132(40):13978–13980, 2010.

[165] Hailong Chen, Geoffroy Hautier, and Gerbrand Ceder. Synthesis, computed stability, and crystal structure of a new family of inorganic compounds: carbonophosphates. *J. Am. Chem. Soc.*, 134(48):19619–19627, 2012.

[166] Mahesh Datt Bhatt and Colm O'Dwyer. Recent progress in theoretical and computational investigations of Li-ion battery materials and electrolytes. *Phys. Chem. Chem. Phys.*, 17(7):4799–4844, 2015.

[167] Monica Sawicki and Leon L Shaw. Advances and challenges of sodium ion batteries as post lithium ion batteries. *RSC Advances*, 5(65):53129–53154, 2015.

[168] Diem My Duong, Van An Dinh, and Takahisa Ohno. Quasi-three-dimensional diffusion of Li ions in $Li_3FePO_4CO_3$: First-principles calculations for cathode materials of Li-ion batteries. *Appl. Phys. Express*, 6(11):115801, 2013.

[169] Verónica Palomares, Paula Serras, Irune Villaluenga, Karina B Hueso, Javier Carretero-González, and Teófilo Rojo. Na-ion batteries, recent advances and present challenges to become low cost energy storage systems. *Energy Environ. Sci.*, 5(3):5884–5901, 2012.

[170] Young-Uk Park, Dong-Hwa Seo, Hyung-Soon Kwon, Byoungkook Kim, Jongsoon Kim, Haegyeom Kim, Inkyung Kim, Han-Ill Yoo, and Kisuk Kang. A new high-energy cathode for a Na-ion battery with ultrahigh stability. *J. Am. Chem. Soc.*, 135(37):13870–13878, 2013.

[171] Maowen Xu, Long Wang, Xin Zhao, Jie Song, Hui Xie, Yuhao Lu, and John B Goodenough. $Na_3V_2O_2(PO_4)_2F$/graphene sandwich structure for high-performance cathode of a sodium-ion battery. *Phys. Chem. Chem. Phys.*, 15(31):13032–13037, 2013.

[172] Mateos Bianchini, Nicolas Brisset, François Fauth, François Weill, Erik Elkaim, Emmanuelle Suard, Christian Masquelier, and Laurence Croguennec. $Na_3V_2(PO_4)_2F_3$ revisited: A high-resolution diffraction study. *Chem. Mater.*, 26(14):4238–4247, 2014.

[173] Ian L Matts, Stephen Dacek, Tomasz K Pietrzak, Rahul Malik, and Gerbrand Ceder. Explaining performance-limiting mechanisms in fluorophosphate Na-ion battery cathodes through inactive transition-metal mixing and first-principles mobility calculations. *Chem. Mater.*, 27(17):6008–6015, 2015.

[174] P. E. Blöchl. Projector augmented-wave method. *Phys. Rev. B*, 50:17953–17979, 1994.

[175] G. Kresse and J. Furthmüller. Efficient iterative schemes for ab initio total-energy calculations using a plane-wave basis set. *Phys. Rev. B*, 54:11169–11186, 1996.

[176] John P. Perdew, Kieron Burke, and Matthias Ernzerhof. Generalized gradient approximation made simple. *Phys. Rev. Lett.*, 77:3865–3868, 1996.

[177] Anubhav Jain, Geoffroy Hautier, Charles J. Moore, Shyue Ping Ong, Christopher C. Fischer, Tim Mueller, Kristin A. Persson, and Gerbrand Ceder. A high-throughput infrastructure for density functional theory calculations. *Comp. Mater. Sci.*, 50(8):2295 – 2310, 2011.

[178] Graeme Henkelman, Blas P. Uberuaga, and Hannes Jónsson. A climbing image nudged elastic band method for finding saddle points and minimum energy paths. *J. Chem. Phys.*, 113(22):9901–9904, 2000.

[179] Graeme Henkelman and Hannes Jónsson. Improved tangent estimate in the nudged elastic band method for finding minimum energy paths and saddle points. *J. Chem. Phys.*, 113(22):9978–9985, 2000.

[180] Miao Liu, Ziqin Rong, Rahul Malik, Pieremanuele Canepa, Anubhav Jain, Gerbrand Ceder, and Kristin A. Persson. Spinel compounds as multivalent battery cathodes: A systematic evaluation based on ab initio calculations. *Energy Environ. Sci.*, 8(3):964–974, 2015.

[181] Gopi Krishna Phani Dathar, Daniel Sheppard, Keith J Stevenson, and Graeme Henkelman. Calculations of Li-ion diffusion in olivine phosphates. *Chem. Mater.*, 23(17):4032–4037, 2011.

[182] Hao Lin, Yanwei Wen, Chenxi Zhang, Lulu Zhang, Yunhui Huang, Bin Shan, and Rong Chen. A GGA+U study of lithium diffusion in vanadium doped $LiFePO_4$. *Solid State Commun.*, 152(12):999–1003, 2012.

[183] Bo Xu and Shirley Meng. Factors affecting Li mobility in spinel $LiMn_2O_4$: A first-principles study by GGA and GGA+U methods. *J. Power Sources*, 195(15):4971–4976, 2010.

[184] Dane Morgan, Anton Van der Ven, and Gerbrand Ceder. Li conductivity in Li_xMPO_4 (M = Mn, Fe, Co, Ni) olivine materials. *Electrochem. Solid State Lett.*, 7(2):A30–A32, 2004.

[185] Fei Zhou, Matteo Cococcioni, Chris A Marianetti, Dane Morgan, and G Ceder. First-principles prediction of redox potentials in transition-metal compounds with LDA+ U. *Phys. Rev. B*, 70(23):235121, 2004.

[186] Shyue Ping Ong, William Davidson Richards, Anubhav Jain, Geoffroy Hautier, Michael Kocher, Shreyas Cholia, Dan Gunter, Vincent L. Chevrier, Kristin A. Persson, and Gerbrand Ceder. Python materials genomics (pymatgen): A robust, open-source python library for materials analysis. *Comp. Mater. Sci.*, 68(0):314 – 319, 2013.

[187] Zigeng Liu, Yan-Yan Hu, Matthew T. Dunstan, Hua Huo, Xiaogang Hao, Huan Zou, Guiming Zhong, Yong Yang, and Clare P. Grey. Local structure and dynamics in the Na-ion battery positive electrode material $Na_3V_2(PO_4)_2F_3$. *Chem. Mater.*, 26(8):2513–2521, 2014.

[188] A Van der Ven and G Ceder. Lithium diffusion in layered Li_xCoO_2. *Electrochem. Solid State Lett.*, 3(7):301–304, 2000.

[189] Biao Zhang, Romain Dugas, Gwenaelle Rousse, Patrick Rozier, Artem M Abakumov, and Jean-Marie Tarascon. Insertion compounds and composites made by ball milling for advanced sodium-ion batteries. *Nature Communications*, 7, 2016.